DISSERTATION

INVESTIGATION OF RELATIONSHIPS BETWEEN TROPICAL CYCLONE STRUCTURE AND INTENSITY CHANGE

Submitted by

Eleanor G. Casas

Department of Atmospheric Science

In partial fulfillment of the requirements

For the Degree of Doctor of Philosophy

Colorado State University

Fort Collins, Colorado

Summer 2022

Doctoral Committee:

Advisor: Michael M. Bell

David A. Randall
Eric D. Maloney
Subhas Karan Venayagamoorthy

ABSTRACT

INVESTIGATION OF RELATIONSHIPS BETWEEN TROPICAL CYCLONE STRUCTURE AND INTENSITY CHANGE

Rapid intensification (RI) of a tropical cyclone (TC) remains one of the largest sources of intensity forecast error, due in part to internal dynamics that are complex and less well understood. Part of the difficulty in improving understanding of RI is due to complex interactions across a wide range of TC intensities, shapes, and sizes. In this doctoral study, I investigate these interactions by first simplifying the complexity and reducing the dimensionality of the intensity and structure parameter space to distill the key aspects of variability from observations, and then re-introducing physical complexity back into the experimental design through idealized modeling.

In Chapter 2, an Empirical Orthogonal Function (EOF) analysis is used to develop the intensity-size framework that lays the foundation for the rest of this doctoral study. In addition to commonly-used TC metrics, a new structural parameter is introduced that describes the decay of tangential wind outside the radius of maximum wind (RMW). The utility of this framework is demonstrated for describing key TC evolutionary features with observations of Hurricanes Rita (2005) and Charley (2004) and numerical simulations of Rita.

In Chapter 3, simplified TC analytic profiles are used to construct physically realistic wind fields that can explore the intensity-size phase space. Results suggest that while there are systematic differences between the details of the reconstructed wind fields using different methods, they all are representative of observed variability in TC structure despite being derived from a relatively small set of parameters derived from the EOFs.

In Chapter 4, these simplified TC wind profiles are used to investigate the tropical cyclone boundary layer (TCBL) response across our intensity-size phase space using both height-averaged (slab) and height-resolved TCBL numerical models. The results suggest that while there are

some different dynamical ramifications of the specific analytic profiles used, the response depends more on the location in the intensity and size phase space than on the differences between analytic wind formulations. The results indicate that (1) strong, big TC profiles produce the strongest supergradient wind within the TCBL; (2) weak, big TCs have the largest RMW contraction as the TCBL adjusts; and (3) weak TCs regardless of size have TCBL responses that are less conducive for intensification.

Finally, in Chapter 5, full-physics, axisymmetric models are used to test whether the one-way TCBL responses found in Chapter 4.3 are consistent with two-way TCBL interactions with influences from convection, and explore the dependencies of intensification rates on TC internal structure. The results suggest that small, strong TCs can achieve the highest rapid intensification rates. The findings suggest that while intensification rates do not systematically vary with contraction rates of the RMW, both intensification and contraction rates do have some dependence on different aspects of TC intensity and size across the phase space. When visualized in the phase space, there is a relatively smooth transition between a "initially large mode" and "initially small mode" of RI. The findings of this doctoral study provide new insights into the role of TC intensity and size in the RI process.

ACKNOWLEDGEMENTS

I would first like to thank my advisor, Dr. Michael Bell, who graciously helped me transfer from the University of Hawaii at Manoa to Colorado State University, where I have matured as an atmospheric scientist and had multiple rewarding teaching experiences that have helped me discover my passion for education.

I would also like to thank the Office of Naval Research, and their awards N000141613033, N000141712230, and N000142012069 for supporting me throughout my graduate school career.

I would also like to thank my committee, Dave Randall, Eric Maloney, and Karan Venayagamoorthy for their helpful feedback and support throughout both my master's and doctoral programs.

I would also like to thank the Engineering Success Center, and Bert Vermuelen, April Undy, and Anthony Marchase, for their enthusiasm for teaching and helping me develop my teaching philosophy and confidence in my teaching abilities as both a Graduate Teaching Fellow and the inaugural Engineering Summer Camp Faculty for the ENcourage Engineering Math Program.

I would also like to thank Dave Thompson for mentoring me during my teaching as a Graduate Teaching Assistant, and Luke Davis for help with lab preparations in ATS-351.

Finally, I would most of all like to thank my husband, Mike Casas, for supporting me through all of the immense stress of being a graduate student during a global pandemic, and for all of the sacrifices he has made throughout the years. I look forward to our future chapters of life together.

TABLE OF CONTENTS

Chapter 1

Introduction

Tropical Cyclones (TCs) are extreme weather phenomena that can cause prolific damage in their path, and accurately forecasting their intensity and size at long lead times is important for protecting both lives and infrastructure. However, while great strides have been made towards improving TC track forecasts, intensity forecasts have only begun to improve in the last decade (Cangialosi et al. 2020). The largest source of intensity forecast error is due to rapid intensity changes, either rapid weakening or intensification, and the sources of rapid intensity change are due to a combination of environmental and internal sources of error (Cangialosi et al. 2020; Trabing and Bell 2020). Therefore, to improve intensity forecasts, the representation and understanding of environmental and internal influences needs to be improved.

Researchers have long known that TCs are strongly influenced by aspects of their environment, such as effects from the sea surface temperature (SST), where warmer water is more conducive for intensification; vertical wind shear, where low shear is most conducive for intensification; and mid-level humidity, where more humidity is more conducive for intensification (Gray 1968). While there is still much to learn about the complex interactions between TCs and their environment, a general rule of thumb is that as the environment becomes more "favorable," TCs generally intensify faster and to higher peak intensities, and vice versa.

However, this general rule of thumb is not perfect, because favorable environments are also associated with the largest forecast errors, and due in part to less well-understood internal effects on rapid intensification (Trabing and Bell 2020). For example, rapid intensification has been linked to convective bursts within the inner core (Rogers et al. 2013), the overall degree of axisymmetry (Miyamoto and Takemi 2015), and tropical cyclone boundary layer effects (Smith and Montgomery 2015; Torgerson et al. 2022). Convective bursts are strong thunderstorms in the inner core that quickly grow upscale, and while they will not be directly investigated in this doctoral study, their uncertain role in TC intensification will be used to introduce much of the complicated interplay between various internal processes that will be investigated.

Statistical analysis of radar observations has indicated that TCs that undergo RI have more convective bursts located radially inward of the radius of maximum tangential wind (RMW), but uncertainty remains as to whether they are a cause or symptom of rapid intensification (Rogers et al. 2013). A reason to suggest that they may be a cause of rapid intensification stems from the balanced vortex model (Eliassen 1951). In this model, a heat source located within the RMW acts to spin up the vortex, and a heat source located further within the RMW is more efficient at spinning up the vortex (Schubert and Hack 1982; Shapiro and Willoughby 1982; Pendergrass and Willoughby 2009; Hendricks et al. 2014). Therefore, in this conceptual model, convective bursts and their associated latent heat release and vertical motion within the RMW should become increasingly favorable the further radially inward they are located.

However, reasons why convective bursts might be considered a symptom of rapid intensification instead of a direct cause relates to the uncertainty as to why convective bursts are located further radially inward compared to slower intensifying TCs. For example, they might be forming in association with enhanced frictional convergence in the TCBL inward of the RMW (Kepert 2001, 2010), or they might be a symptom of reduced inertial stability in the outer core that allows for a greater radial displacement (Rogers et al. 2013). Regarding the latter, a balance between radial inflow and inertial stability has been proposed by Kepert (2017), who suggests that this balance is responsible for the distance between the radius of the maximum updraft and the RMW.

However, convective bursts may also play a critical role in stretching large amounts of vorticity in the rotating convection paradigm (Montgomery and Smith 2014; Smith and Montgomery 2015).In the azimuthally-averaged component of this paradigm, angular momentum is converged both above and within the TCBL to further spin up the general vortex.

Thus so far, internal processes related to rapid intensification already entail a range of complex interactions between the location of convection and its associated dynamics and thermodynamics within a broader vortex on time scales shorter than the lifetime of a TC.

Further complicating matters, recent research suggests that in addition to interactions on shorter time scales, internal processes are also influenced by memory of initial conditions of TC intensity and size, as well. For example, recent research suggests that the incipient vortex size strongly influences future TC size and steady-state intensity (Martinez et al. 2020; Tao et al. 2020).

However, there are also many ways that intensity and size are defined, which can complicate physical understanding. For example, size can also be defined as the radius of outermost closed isobar (e.g. Merrill 1984), the radius of gale force wind (e.g. Knaff et al. 2016), or the radius of vanishing wind (e.g. Chavas and Emanuel 2010). While TC size and intensity are weakly correlated overall (Merrill 1984; Chavas and Emanuel 2010; Chan and Chan 2012), there is both theoretical (e.g. Hendricks et al. 2014) and anecdotal (e.g. Rogers et al. 2017) evidence to suggest that size may play a role in intensification rates, such that small TCs are potentially capable of undergoing faster RI and reaching higher intensities given a conducive environment.

However, since the parameter space to fully investigate the effects of TC intensity and size on internal processes of rapid intensification is very large, studies typically perturb only a portion of the possible parameter space to investigate these interactions, such as the RMW, or the decay rate of tangential wind radially outward from the RMW (Stern et al. 2015; Williams Jr. 2015, e.g.). Thus, while many pieces about internal processes and interactions have been studied over time, a contextualized understanding of how these pieces fit together is missing.

Therefore, this doctoral study seeks to investigate internal processes of rapid intensification in a more holistic approach, where the different dependencies on intensity and size become readily apparent and are based on observed variability.

1.1 Dissertation Objectives and Outline

This dissertation presents four chapters that systematically investigate the interconnected relationships between how the observed variability in TC intensity and structure can be most simplified, the TCBL response to this variability, and how rapid intensification varies as a function of intensity and size.

In Chapter 2, we first investigate the observed variability of TC intensity and structure at flight-level, near the top of the TCBL. An Empirical Orthogonal Function (EOF) analysis analysis is used to identify the primary modes of variability, and results show that TC intensity explains the most variance, while TC size explains the second most variance. The third mode of variability describes TC "maturity," and is dominated by a new parameter that describes the rate of decay of tangential wind speed outside the RMW. The first two principle components are then used to define an orthogonal intensity-size phase space, and its utility is demonstrated through both observations of Hurricanes Rita (2005) and Charley (2004) and numerical simulations of Hurricane Rita.

In Chapter 3, we then investigate how to best reconstruct realistic idealized tangential wind profiles from our intensity-size phase space, and we test three different methods. Results show that while each method has its own strengths and weaknesses regarding fit to a defined set of "anchor points," all simplified profiles lie within observed variability. The vorticity shapes of the three methods are all found to be quite different, which motivates further investigation in the next chapter.

In Chapter 4, we then investigate the TCBL response to the simplified wind profiles using a new TCBL model in both height-averaged and height-resolved configurations. Results show that the TCBL response varies smoothly across the intensity-size phase space, such that the strong, big TCBLs have the strongest supergradient winds and secondary circulations. The weak, big TCBLs undergo the most contraction in response to a constant gradient wind forcing. The small TCBLs are found to have relatively weak secondary circulations relative to larger TCBLs at the same intensity, which may be related to why they experience less contraction.

In Chapter 5, we investigate how the rapid intensification varies as a function of TC intensity and size in a set of axisymmetric, full-physics simulations. Results show that while strong, small TCs have the fastest intensification rates, the strong, big TCs have the highest quasi-steady intensities. Additionally, we find that rapid intensification and RMW contraction rates only strongly vary together during the initial portion of RI for weak, big TCs. Weak, small TCs have limited RMW contraction during the initial portion of RI, and strong TCs have little to no RMW contraction throughout rapid intensification regardless of size.

In Chapter 6, we synthesize the findings of this dissertation, and discuss implications and future work.

Chapter 2

An Intensity and Size Phase Space for Tropical Cyclone Structure and Evolution[1]

2.1 Introduction

While all tropical cyclones (TCs) have differences in structure that ultimately make each one unique, there are common characteristics that allow us to characterize TCs by various intensity and size metrics. TC structure and intensity are also related to each other, which is demonstrated by the ability to estimate TC intensity from observations of TC structure via satellite imagery using techniques such as the Dvorak method (e.g. Velden et al. 2006, and references therin). However, while structure and intensity are intimately related, the relationships can be complex, and it has been known for several decades that there is a weak statistical relationship between TC size and intensity Merrill (1984). This weak statistical relationship between TC intensity and size is due in part to the fact that there is still considerable structural variability across TCs with the same intensity Xu and Wang (2015). Additionally, the use of different metrics to describe intensity, structure, or size can yield different relationships and complicate our physical understanding.

Variability in structure and intensity is also important since those metrics influence future TC intensities and intensification rates. For example, recent research has suggested that the initial TC structure strongly impacts evolution throughout the rest of the TC life cycle, such that initially larger idealized TCs can achieve higher steady-state intensities when the environment is constrained to yield TCs with the same maximum potential intensities Tao et al. (2020); Xu and Wang (2018). Initial structural variability of the vortex skirt outside the radius of maximum

[1]The results outlined in this chapter have been submitted for publication and are pending revision. Used and adapted with permission.

wind was found to be more important for setting TC expansion rates than environmental moisture in both 2D and 3D idealized CM1 simulations Martinez et al. (2020). Studies have shown that assimilating TC observations such as dropsonde, flight-level and radar data can improve TC structure and hence improve forecasts of rapid intensification Tao et al. (2022). Tao et al. (2022) demonstrates the evolution pathway is also determined by TC structure in addition to TC intensity. In this study, we seek to simplify the characterization of intensity and size through an examination of observed variability in wind structure obtained from aircraft reconnaissance.

While the term "TC structure" can refer to a broad array of TC attributes, one of the most commonly observed is TC size. However, there are many different ways to measure TC size depending on the phenomenon of interest. For example, studies that focus on inner-core processes may use the radius of maximum wind (RMW) or the absolute angular momentum at the RMW (M_{max}). In contrast, studies that focus on outer-core processes or TC hazards may use the radius of gale-force winds (R_{34}) instead.

RMW is an important metric to measure because changes in RMW typically correspond with changes in TC intensification. For example, many tropical storms start with a large RMW that contracts as the TC intensifies, and this evolution is often likened to the "ice skater" angular momentum analogy. However, recent research suggests that RMW contraction often ends before TC intensification is finished Stern et al. (2015). In addition, jumps in the magnitude of RMW are associated with eyewall replacement cycles, which also modulate TC intensification as the inner eyewall decays.

M_{max} contains both intensity and size information, and it is known to be related to a TC's maximum potential intensity (MPI) Tao et al. (2020). Since lines of constant angular momentum are often assumed to not penetrate the tropopause, they exhibit a strong constraint on MPI. In addition, since absolute angular momentum increases with increasing radius in an inertially stable vortex, it can be used as a radial coordinate known as 'potential radius'. In this case, M_{max} is related to a TC's "dynamic size," and tight radial gradients near M_{max} are stretched to show detail (e.g. Schubert and Hack 1983; Martinez et al. 2019).

R_{34} is also an important variable because it is used for forecasting potential hazards and damage extents Knaff et al. (2016). In addition, the magnitude of R_{34} is linked to changes in structure, such as the likelihood of secondary eyewall formation or other inner-core structures (e.g. Xu and Wang 2015; Musgrave et al. 2012; Rozoff et al. 2012) and the magnitude of R_{34} is also related to future intensification rates Xu and Wang (2015).

However, while related, these three different size parameters do not necessarily co-vary together. Therefore, the concept of TC fullness has been proposed, which is defined as TCF $\equiv$ $1 - \text{RMW}/R_{34}$ Guo and Tan (2017). Fullness is highly correlated with intensity, and a rapidly increasing fullness is also associated with rapid intensification.

While fullness can be considered a measure of "TC shape," it does not directly consider intensity in its definition. The rate of decay of wind from the RMW to R_{34} also varies, and is often approximated by a modified Rankine decay parameter Mallen et al. (2005). In this study, we quantify this wind decay with respect to the slope of normalized angular momentum (M^*) Martinez et al. (2017). In this study, we introduce a new parameter denoted as ϕ that represents this slope, and show that this parameter is related to TC maturity.

In addition to having multiple different TC size parameters, there are also multiple ways to define TC intensity, such as the maximum wind speed or minimum central pressure. The maximum wind speed (V_{max}) is a primary way of characterizing intensity, but there are several variations in how it is defined depending on the wind-averaging period and altitude. In this study, we define V_{max} as the azimuthally averaged flight-level tangential velocity, and use "surface intensity" to refer to the Best Track (BT) 1-minute sustained surface wind speed anywhere in the storm as defined by the U.S. National Hurricane Center.

Intensity is also commonly quantified as the minimum central surface pressure (P_{min}) of the TC. Recent research suggests that P_{min} correlates better with TC size and total damage than V_{max} Klotzbach et al. (2020), and acts as a relatively good evaluation metric for TC structure Tao et al. (2022). While most global estimates of P_{min} rely on the Dvorak technique, it can be measured more accurately and easily than V_{max} or surface intensity, because it is a single point that can be measured with a barometer, and it is not dependent on azimuthal averages or extrapolations to the surface wind speed.

Since there are so many intensity and size metrics in use and they all co-vary to varying degrees, a central purpose of the article is to reduce the dimensionality of TC structure and intensity characterization. We seek to find metrics such that size and intensity are more orthogonal in order to better characterize the TC with as few parameters as possible. Finally, we also seek to have the metrics represent the full range of variability of observed structure and apply the new metrics to explain the existing findings.

To satisfy these objectives, we utilize aircraft TC observations and empirical orthogonal functions (EOFs). EOFs have been successfully used for revealing useful information on many atmospheric systems, such as determining the location and strength of the MJO (e.g. Wheeler and Hendon 2004). By using the EOF on observational data, we are able to reduce the dimensionality of TC intensity and structure into their primary modes of variability, as well as compare past and future data to climatological averages and standard deviations in an orthogonal space. We show further that the size and intensity phase space developed here can be used to validate numerical weather prediction models.

In Section 2.2, we will define the new wind decay parameter in more detail, describe the datasets used in this study, detail how we perform our EOF, and describe numerical model setups used to show an example of applications of this study. In Section 2.3, we will describe the results of the EOF as well as demonstrate a useful application. We discuss and summarize the key findings in Section 2.4.

2.2 Methods

2.2.1 A new wind decay parameter

In this study we define a new wind decay parameter, denoted simply as ϕ, as the angle with respect to the y-axis in normalized r^* and M^* space that is defined as

$$\tan\phi \equiv 1/(M^*_{2RMW} - 1) \tag{2.1}$$

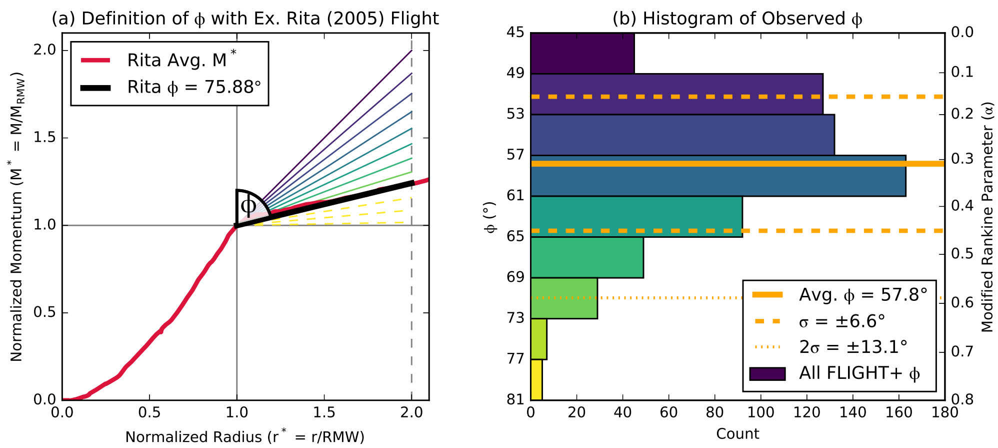

Figure 2.1: (a) Definition of ϕ as in Eq. 2.1, with an example M^* profile from Rita at peak intensity (red). The purple to yellow lines in (a) correspond with the bin boundaries of the histogram in (b). (b) Histogram of all ϕ observations that were included in the final dataset. The solid orange line shows the average ϕ in the final dataset, and the dashed and dotted lines represent 1- and 2- standard deviations of ϕ, respectively.

where r^* is radius normalized by the radius of maximum azimuthally averaged flight-level tangential wind (RMW), M^* is the absolute angular momentum normalized by its value at the RMW, and M^*_{2RMW} is the absolute angular momentum at twice the RMW (2RMW) normalized by the magnitude of the absolute angular momentum at the RMW. Note that the numerator in Eq. 2.1 is 1 because we have defined ϕ as between 1–2 RMW to both sufficiently describe the TC structure and also allow for quantification of this metric with observed flight-level winds.

Since the exact value of M^*_{2RMW} can be noisy due to convection and turbulence at flight-level, we use a best-fit line that is fixed at the point (1,1) to estimate M^*_{2RMW} and therefore ϕ. This decision to use a linear fit is justified by the quasi-linear shape of M^* profiles beyond (1,1) in observed wind profiles. An example of a M^* profile in Hurricane Rita (2005) near peak intensity is shown in Fig. 2.1a. To calculate the linear best-fit line, an endpoint outside the RMW needs to be specified. In this study, we chose an outer radii of 2RMW because flight-level azimuthal averages often have limited coverage beyond 2RMW due to flight limitations such as distance to land, finite fuel and flight hours, and mission objectives. The black line shows the best fit to the observed M^* profile, yielding the angle ϕ respect to the y-axis in normalized r* and M* space.

The ϕ parameter can be related to the modified Rankine alpha parameter through the relationship

$$\tan\phi = \frac{r^* - 1}{(r^*)^{1-\alpha} - 1} \tag{2.2}$$

where r^* is the normalized outer RMW of interest (which we define as 2RMW), and α is the modified Rankine parameter (Fig. 2.1b). Through this relationship, we can see that the minimum angle of ϕ is 45 degrees because that would correspond with an α of 0, and that a pure Rankine vortex with an α of 1.0 would correspond with a ϕ of 90 degrees. Values greater than 90 degrees would imply an inertially unstable vortex.

A physical interpretation of ϕ is that a ϕ of 45 degrees would be a wind profile that has constant V_{max} from 1- 2RMW, implying no wind decay. This is typically only possible in weak or immature storms. As a TC matures, the wind decay and alpha typically increase Mallen et al. (2005) and the angle of ϕ increases. If a TC were to intensify to a pure Rankine vortex with zero vorticity outside the RMW, ϕ would increase to 90 degrees. However, observed TCs rarely, if ever, reach this condition, and we are interested in discovering what a realistic upper-bound of ϕ is for observed TCs. We chose to estimate ϕ instead of trying to estimate α because ϕ is easier to calculate and simple to interpret. Instead of trying to work with exponential fits, we are able to simply use a linear best fit.

A histogram of ϕ angles calculated in the flights remaining after the quality control (QC) conditions outlined in Section 2.2.3 are shown in Fig. 2.1b. The bin width is set to correspond with increments of 4 degrees of ϕ to aid with physical interpretation, and corresponding values of α that are shown on the right were calculated from Eq. 2.2. The mean angle of ϕ in our dataset is 57.8 degrees, with a standard deviation of 6.6 degrees. There is also a right skew in the histogram, indicating that most values of ϕ are associated with less mature TC structures.

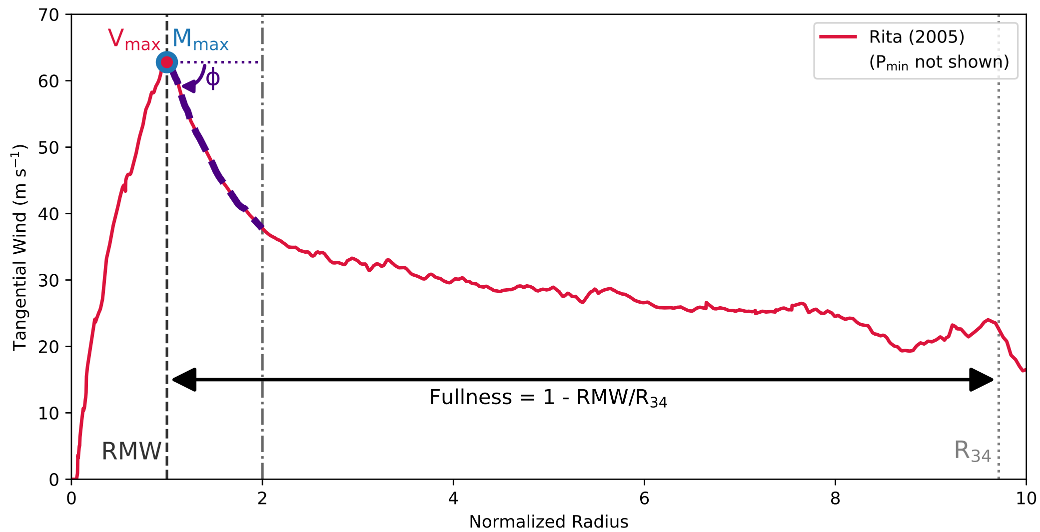

Figure 2.2: Visual depiction of variables used in this study, using the same example Rita (2005) flight data at peak intensity (in red) as shown in Fig. 2.1. Dataset variables include V_{max} (red point), M_{max} (blue point), RMW (dark gray dash), R_{34} (light gray dotted), fullness (black arrow), ϕ (purple angle), and P_{min} (not shown). Purple dashing shows the extent of the ϕ definition, which extends out to 2RMW (medium gray dash-dot).

2.2.2 Observational Datasets

We used two observational datasets in this study to derive seven parameters that describe intensity, size, or structure. The first dataset is the Flight Level Dataset (FLIGHT+), version 1.3 Vigh et al. (2020). We primarily used the binned flight-level tangential wind to compute azimuthal averages and obtain V_{max}, from which we derived RMW, M_{max}, and ϕ. We also used the RMW from FLIGHT+ to compute fullness (as defined in Section 2.1), since RMW is not quality controlled in Best Track estimates prior to 2020 and is not reliably present in IBTrACs.

We also used two parameters from the International Best Track Archive for Climate Stewardship (IBTrACS; Knapp et al. 2010) dataset to supplement additional parameters of interest, P_{min} and R_{34}. In addition to being used as its own parameter, R_{34} was also used to calculate fullness, which means that fullness is the only parameter that was derived from multiple datasets.

The seven parameters used in our EOF analysis (P_{min}, V_{max}, RMW, M_{max}, R_{34}, fullness, and ϕ) and the distributions and data sources of each parameter are shown in Figs. 2.2–2.3. Fig. 2.2 shows the variables relative to the original FLIGHT+ azimuthally-averaged, flight-level tan-

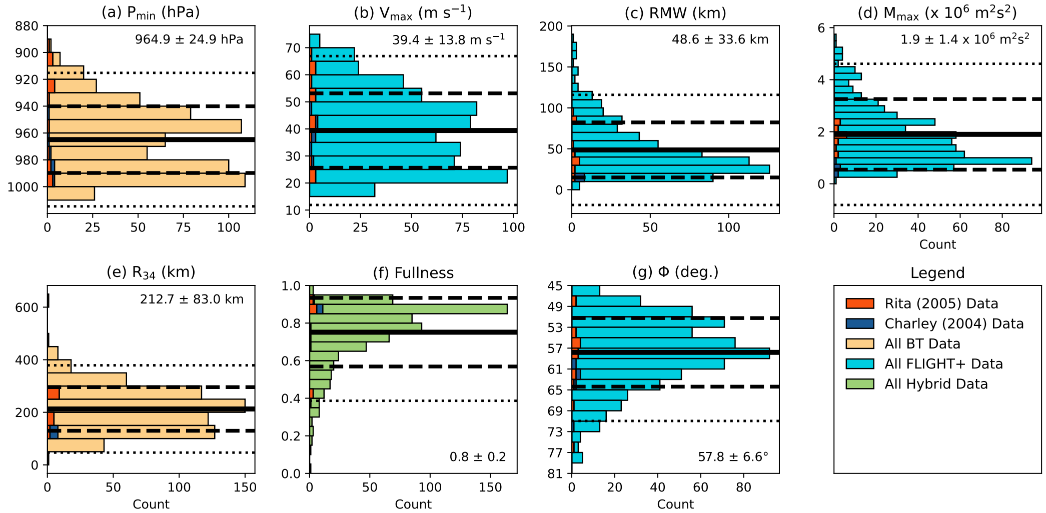

Figure 2.3: Histograms of the parameters used in this study. Orange and blue represent Hurricanes Rita (2005) and Charley (2004), respectively, and the remaining data is color-coded to denote whether the data source is interpolated from the Best Track (yellow), azimuthally-averaged flight-level data from FLIGHT+ (blue), or derived from both datasets (green). Black lines denote each parameter's average (solid), the first standard deviation (dashed), or second standard deviation (dashed) as in Fig. 2.1. The quantitative value of each average and first standard deviation are written on the right-hand side.

gential wind profile, with the exception of P_{min}, and demonstrates that the seven parameters chosen in this study represent a broad range of attributes that describe both the inner- and outer- core structure of the TC. Fig. 2.3a-b show the azimuthally-averaged flight-level V_{max} and interpolated Best Track minimum surface pressure P_{min}, with an average P_{min} of 964 hPa and an average V_{max} of 39.4 m s^{-1}. The dataset encompasses a wide range of intensity values about the mean values. Similarly, our three size parameters —RMW, M_{max}, and R_{34} —show that the average of TC observations have values of 48.6 km, 1.9 × 10^6 m^2 s^2, and 212.7 km, respectively (Fig. 2.3c-e). Finally, we can see that the mean fullness values are more skewed and have an average of 0.8, and ϕ has a wider range and an average angle of 57.8 deg. as in 2.1b but is shown with a finer bin interval here (Fig. 2.3f-g).

In Section 2.3.1, we will demonstrate the utility of our EOF analysis by highlighting two example TCs within our dataset: Hurricane Rita (2005) and Hurricane Charley (2004). Figure 2.3 shows how our two example TCs compare to the distributions within the full dataset across their lifetimes. Fig. 2.3a-b shows that Rita and Charley have observations at nearly the full range of

V_{max} and P_{min}. Fig. 2.3c-e show that Rita and Charley were average sized and small, respectively, compared to other storms. Fullness in Fig. 2.3f shows that Rita and Charley were close to 0.9 through much of their lifecycle, but did have some smaller values at times. Finally, Fig. 2.3g shows that Rita and Charley encompassed a large range of ϕ within the dataset.

2.2.3 EOF Procedure

The seven variables from the observational datasets were quality-controlled before computing the EOF so that we were only using physically-relevant data. The quality control thresholds are:

1. The TCs must have been officially been designated as at least a Tropical Storm (TS) for more than three hours
2. The azimuthal average must contain at least 3 radial legs
3. Each flight time must have all 7 parameters
4. ϕ must be less than or equal to 90 deg.
5. V_{max} must be at least 18 m/s (TS strength)
6. The M^* profile must extend out to at least 2RMW

After quality-controlling the data, we had 649 observations from the Atlantic basin available for analysis. We then standardized each parameter with their mean and standard deviation before computing the EOF.

Since some of the parameters contain redundant information, we tested many permutations of reduced parameter sets to try to create the best EOF that explained sufficient variance and had good separation of the different principal components. We also tested including Integrated Kinetic Energy as an additional parameter, but found it did not add enough value to warrant inclusion, especailly since it was the most difficult to calculate (requiring the entire wind field). We found that using all of seven of the retained parameters produced the best results, since there were sufficient degrees of freedom to determine the primary modes of variance in the observations.

2.2.4 Model Setups

In the results section we also demonstrate a useful application of the EOF by regressing the structure of simulated TCs onto the first two principle components. Here we highlight two variations of Rita (2005) simulations that are adapted from Foerster and Bell (2017). We chose to highlight Rita as an example because it was well-sampled throughout its lifetime across a wide range of the phase space, which facilitates comparisons between observations and simulations.

The model setup was adapted from Foerster and Bell (2017). We use WRF version V3.9.1.1 with three nested domains of 18-, 6-, and 2-km horizontal grid spacing and 43 vertical levels. The three domains had 300, 250, and 250 square grid points respectively, and the two inner domains were vortex-following. The simulations use the following physics parameterizations: Rapid Radiative Transfer Model (RRTM) longwave radiation Mlawer et al. (1997), Dudhia shortwave radiation Dudhia (1989), the Noah land surface model Ek et al. (2003), the Yonsei University boundary layer scheme Hong et al. (2006), Thompson aerosol-aware microphysics Thompson and Eidhammer (2014), and modified surface fluxes for tropical cyclones (Garratt formulation; Davis and Coauthors 2008). The outer two domains use the Kain–Fritsch cumulus parameterization Kain and Fritsch (1990), and the inner domain is convective permitting. The WRF simulations were run from 18 to 23 September 2005, and captured both the period of rapid intensification and the secondary eyewall formation of Hurricane Rita.

We conducted two numerical simulations that were set up identical to each other besides their initial bogus vortex conditions. In particular, we demonstrate the effects of an initially smaller bogus vortex with an initial V_{max} of 17 m s^{-1} and an initial RMW of 150 km, and an initially larger bogus vortex that had an initial V_{max} of 15 m s^{-1} and RMW of 250 km. The model output was smoothed with a Lanczos filter before regressing onto the EOF to make comparisons easier to interpret.

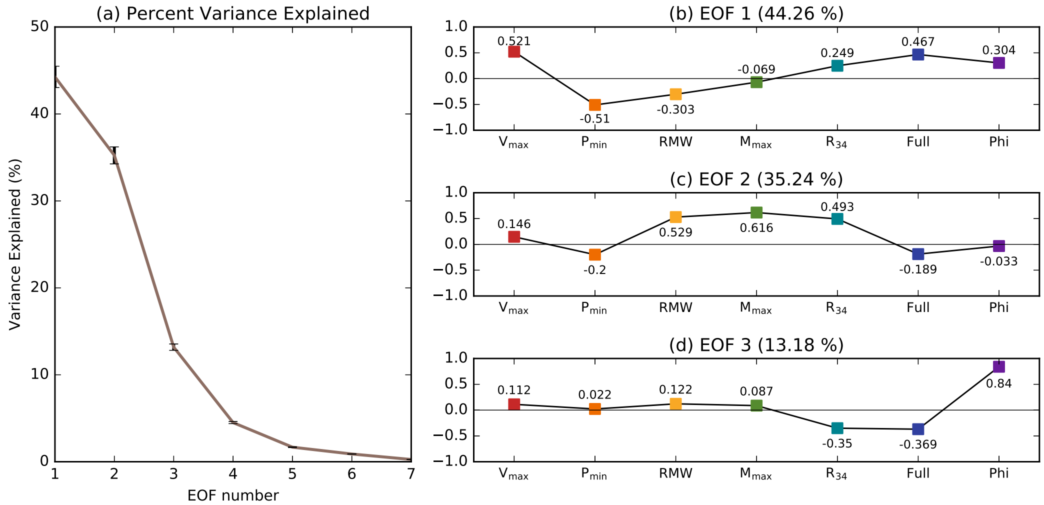

Figure 2.4: (a) Percent variance explained by each EOF mode, with error bars in black. (b-d) The structures of the first three EOF modes. Values indicate the length of the eigenvectors, and rainbow colors are consistent with the arrows in Fig. 2.6

2.3 Results

2.3.1 EOF Results

Figure 2.4a shows the percent variance explained from the EOF analysis. Most of the variance is explained by the first two EOFs at nearly 80%. EOF1 primarily represents variability in intensity since the eigenvectors most strongly on V_{max} and P_{min} (Fig. 2.4b). The variability in wind and pressure is anti-correlated, with positive amplitudes of EOF1 are primarily associated with higher V_{max} and lower P_{min}. In contrast, EOF2 primarily represents variability in size since it most strongly depends on RMW, M_{max}, and R_{34} (Fig. 2.4c). EOF1 also has some sensitivity to fullness, RMW, and R_{34}, but there is almost no relationship to M_{max}, while M_{max} is the most dominant parameter in EOF2. Higher fullness, smaller RMW, and larger R_{34} are therefore all correlated with higher intensity. A larger RMW, larger M_{max}, and larger R_{34} are all correlated with larger size. The first two EOFs being associated with intensity and then size resulted for every tested permutation of EOF analyses, as well as for stricter quality-control requirements (not shown).

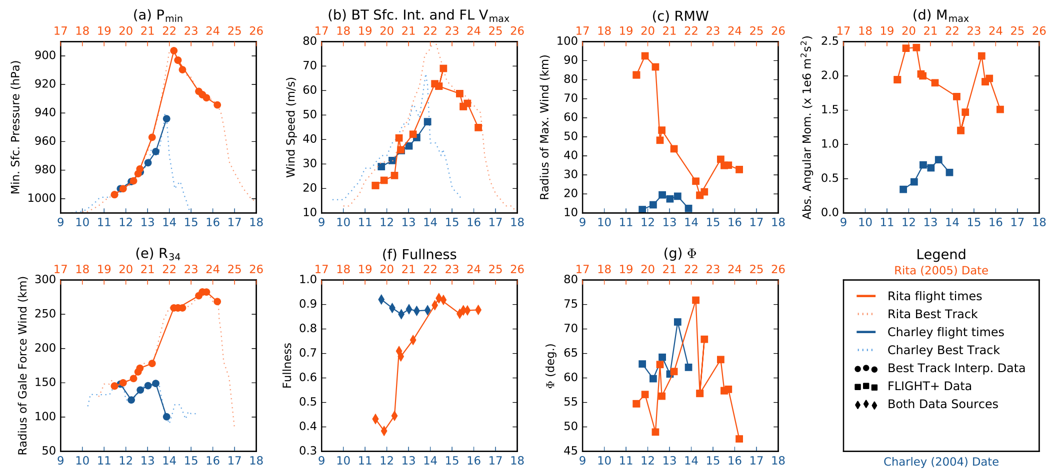

Figure 2.5: Interpolated Best Track and azimuthally-averaged values for Rita (orange) and Charley (blue) that are included within the EOF dataset. The parameters shown are: (a) All P_{min} (hPa) values (pale solid lines) and interpolated to flight times (circles), (b) All Best Track Surface Wind Speed estimates (pale solid lines) and FLIGHT+ flight-level azimuthal averages (V_{max}; m s^{-1}; squares), (c) RMW (km), (d) M_{max} ($\times 10^6$ m^2 s^2), (e) All R_{34} (km) values (pale solid lines) and interpolated to flight times (circles), (f) Fullness, (g) ϕ (deg.). Circles indicate second-order accurate interpolations to the flight time from Best Track data. Squares indicate azimuthally-averaged values at flight-level from FLIGHT+ data. Diamonds indicate that parameters from both datasets were used.

EOF 3 represents approximately 13% of our dataset's variability, and it primarily represents variability in ϕ after accounting for the differences in size and intensity that accounted in EOFs 1-2 (Fig. 2.4d). The fact that ϕ dominates EOF3 indicates that ϕ is a nearly orthogonal parameter to both intensity and size. EOF3 also shows that there is a weak relationship between ϕ and R_{34} and fullness, where TCs with smaller outer wind fields are more likely to have higher ϕ angles. EOFs 4-7 represent a combined variability of approximately 7%, and are not shown because they are likely associated with noise.

However, while we interpret EOF1 as intensity, EOF2 as size, and EOF3 as "maturity," we note that each EOF contains some information on all three attributes, in accordance with the direction of the eigenvectors. In particular, intensity and maturity seem to have some aspects in common, since a component of ϕ points in the same direction as PC1. Similarly, PC1 also incorporates some size information from RMW and R_{34}, and PC2 incorporates some intensity information from P_{min}. However, a benefit of this EOF analysis is that we show how each of the seven metrics covary as TCs evolve.

To more clearly show the relationship between the EOF analysis and physical metrics, Fig. 2.5 shows examples of the lifecycle of Hurricanes Rita (2005) and Charley (2004). These two TCs were chosen to demonstrate how different intensities and sizes are represented in the EOF analysis. Rita (2005) had sixteen flights that met the QC criteria, with intensities that ranged from Categories 1-5 on the Saffir-Simpson scale and a medium size. In contrast, Charley (2004) was small, intense TC sampled by six flights.

Figure 2.5a shows the central minimum surface pressure, which is interpolated from Best Track data to the average flight time with second-order accuracy finite differencing. Note that the y-axis has been reversed such that lower pressures are at the top for easier comparison. The dates on the two x-axes have been aligned to show that Rita and Charley had a period of similar intensification rates near the beginning of their observations. However, Rita was able to reach much lower P_{min} values at peak intensity than Charley.

Figure 2.5b shows the FLIGHT+ azimuthal averages for Rita and Charley in orange and blue, and compares them to the Best Track estimates of sustained 1-min average surface wind speeds. Comparing the FLIGHT+ V_{max} to the surface intensity, there is general agreement with the rate of intensification for both Rita and Charley, but the flight-level tangential velocity averages are consistently lower than the surface wind speed estimates. Comparing the FLIGHT+ V_{max} to the interpolated P_{min} evolutions, Rita appears to have a more similar intensity to Charley at the midpoint of the observed periods, rather than the beginning. This could either be due to limitations to azimuthal averages or be related to the very different sizes of Rita and Charley.

Figure 2.5c shows the RMW of the FLIGHT+ azimuthal averages. While some Best Track estimates were available to compare, they occurred sporadically and are not quality controlled in the official Best Track process. Thus, they were omitted from the figure. Rita's RMW started out quite large and contracted significantly throughout its intensification period. An eyewall replacement is evident with larger RMW around 23 September. In contrast, Charley's RMW remained quite small throughout the observed intensification period. Figure 2.5d shows M_{max}, which is the value used to normalize M profiles to calculate phi. M_{max} is obtained from V_{max}, RMW, and Coriolis parameter, all of which are obtained from the FLIGHT+ dataset. The M_{max} magnitude was larger in Rita and decreased as the RMW contracted. Rita's eyewall replacement is also evident in the M_{max} evolution. In contrast, M_{max} is small in Charley and increased over the lifecycle as V_{max} increased while RMW stayed roughly constant.

Figure 2.5e shows R_{34}, which is also interpolated from Best Track estimates. Interestingly, Rita's R_{34} consistently increases during intensification while Charley's decreases. Figure 2.5f shows fullness, which is the only parameter that uses both FLIGHT+ and Best Track data sources. Charley's fullness remains consistently high during the observing period, while Rita's generally increases throughout its intensification period. Both Rita and Charley have similar fullness around 0.9 at peak observed intensity. Figure 2.5g shows ϕ, which is calculated from FLIGHT+ parameters. While there is some noise apparent in this parameter, there is a clear trend towards larger angles as both TCs intensify. Rita also shows a decrease in ϕ after peak intensity, unlike fullness.

The seven parameter timeseries shows many aspects of the evolution of Rita and Charley, including both intensity and size changes. Through the EOF analysis we can reduce the dimensionality to show these changes in the context of other TCs in a simple 2-D phase space corresponding to the magnitude of the first two principal components (PCs). Figure 2.6 shows the data distribution when we use PC1, which represents intensity, as the x-axis and PC2, which represents size, as the y-axis. Since the parameters were normalized prior to computing the EOF, the point (0,0) represents average intensity and size of a TC in the quality-controlled dataset. The upper-left quadrant represents weak, big TCs, and the lower-right quadrant represents strong, small TCs. The upper-right and lower-left quadrants represent strong, big and weak, small TCs, respectively.

In Fig. 2.6a, each dot represents a single observed axisymmetric TC structure. The dots are shaded by the value of ϕ, which can be thought of as a 'vertical' axis corresponding to PC3. The arrows in the lower-left corner are an alternative way of viewing the first 2 EOFs displayed in Fig. 2.4b-c, where the x-component is the magnitude of each parameter in PC1 shown in

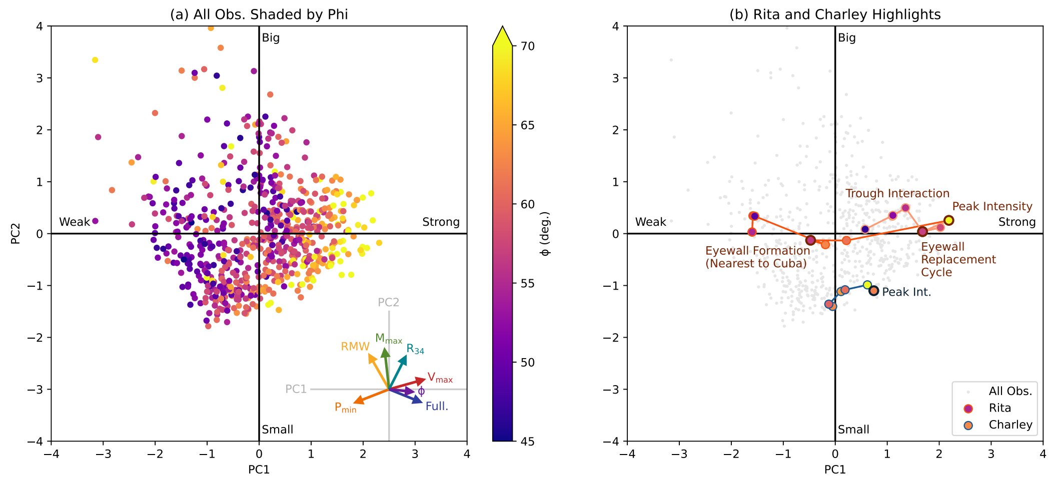

Figure 2.6: EOF dataset transformed into coordinates where PC1 is the x-axis and PC2 is the y-axis. (a) Scatter points of all observations area shaded by ϕ using the same colorbar in Fig. 2.1. Arrows show how the points in Fig. 2.4b-c are represented in this phase space, where Fig. 2.4b are the x-components and Fig. 2.4c are the y-components of each arrow. (b) Gray points represent the same points as in (a), but the Rita and Charley points shown in Fig. 2.5 are highlighted in orange and blue, respectively. The weakening phase of Rita is outlined with a paler orange to make it easier to see, and key lifecycle points are outlined in a darker color and labeled. Additional text labels on the axes are included to help with physical interpretation of both subplots.

Fig. 2.4b and the y-component is the magnitude of each parameter in PC2 shown in Fig. 2.4c. The direction of each arrow corresponds with the gradient of each parameter from low to high magnitudes. In this format, it's also easier to see that V_{max} aligns most closely with the intensity axis, and M_{max} aligns most closely with the size axis. P_{min} is nearly opposite to V_{max}, but has a marginally larger component in the size direction. RMW also has a slightly larger component in the size axis than R_{34}, but both have a small component in the intensity axis. Fullness and ϕ are primarily associated with intensity, but also increase in the negative PC2 direction (i.e. smaller size). The fact that fullness has a larger PC1-component than both RMW and R_{34} corroborates the findings of Guo and Tan (2017), in which fullness was found to be more correlated with Best Track intensity than RMW or R_{34}. While ϕ and fullness have very similar angles with respect to PC1 and PC2, ϕ is primarily oriented in the vertical PC3 direction.

In Fig. 2.6b, the orange- and blue-outlined dots correspond with the observations of Rita and Charley shown in Fig. 2.5, and their shading corresponds to ϕ. Focusing on Rita first, we can see that Rita initially started out in the weak, big quadrant for the first four flights, corresponding to low V_{max} and P_{min} magnitudes and large RMW magnitude on the 19th and early 20th (Fig. 2.5a-c). As Rita continued to intensify and contract the structure 'moves' down and towards the right in the phase space. There was some apparent weakening indicated between the fifth and sixth flights during eyewall formation around 20 September. Rapid intensification and Rita's peak intensity follow as the TC moved further right with increasing PC1 values. During this time period (21 - 22 September), Rita had large changes in all parameters (Fig. 2.5). However, RMW decreases and R_{34} increases such that their contributions yield little net change in the PC2 direction. Just after peak intensity on the 22nd, there is some evidence of Rita's eyewall replacement cycle. Finally, after the eyewall replacement cycle, Rita started interacting with a synoptic-scale, upper-level trough, which sheared Rita and further increased Rita's RMW and R_{34} while weakening the TC (Fig. 2.5c, e).

In contrast, Charley's structure has some of the smallest PC2 magnitudes in the dataset. Charley was not sampled as extensively as Rita over its lifecycle, but we can see that Charley's evolution appears to increase in size for the first half of its observations. Interestingly, while P_{min} and V_{max} appear to be reasonably similar in the first few flights of Charley and Rita (Fig. 2.5a,b), it becomes much clearer in the PC1 framework that Charley is much further along in its lifecycle and more mature than Rita. We can also see that Charley's peak intensity is also weaker than Rita's.

Overall, Fig. 2.6 shows a novel way to visualize TC structure and evolution in a phase space where intensity and size are nearly orthogonal. The general maturation of a TC will tend to move primarily from left to right in this phase space with a corresponding increase in ϕ and fullness. However, individual storms can occupy different parts of the phase space and evolve differently depending on their environmental conditions and internal processes. Structural changes such as contraction, rapid intensification, and eyewall replacement cycles can be visualized simply in this framework. The phase space also allows for easy comparison between different TCs and their variability in terms of 2 standardized variables rather than 7 physical parameters.

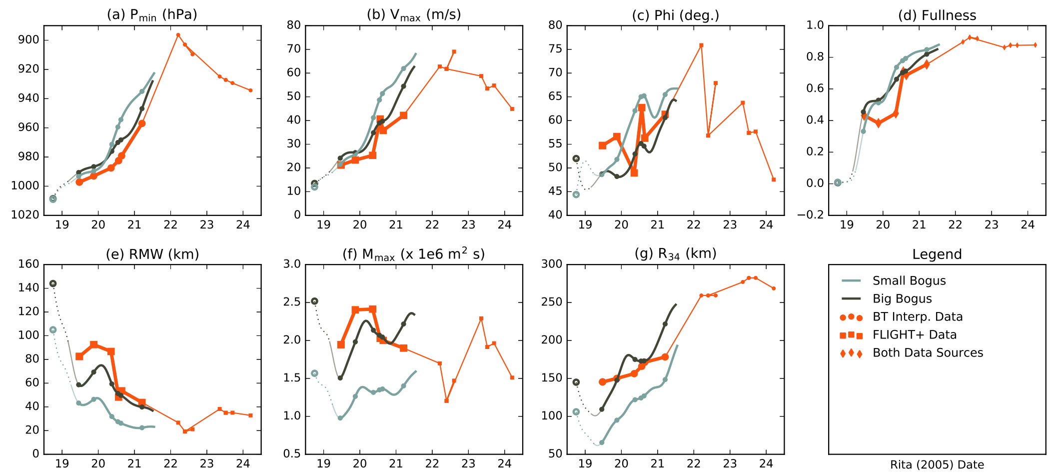

Figure 2.7: Comparison of the two simulations of Rita to the orange observations shown in Fig. 2.5. Dark blue represent the big-bogus simulation, and light blue represents the small-bogus simulation. The open circle represents the simulation initialization; dotted segment of the simulations represent when V_{max} < 18 m s^{-1}, because that portion of the simulation would not meet QC requirements; pale, thin segments of simulations represent that the simulation V_{max} is larger than 18 m s^{-1} but the timing is before Rita's observing period; and bold segments represent the primary comparison time between models and observations. Scatter point symbols for observations are consistent with Fig. 2.5, and equivalent observation times are marked in simulations as well.

2.3.2 Modeling Application

To demonstrate the utility of having orthogonal axes for intensity and size, we show two variations of a Rita simulation: one with a small bogus vortex initialization and one with a large bogus vortex initialization to compare to Rita's well-sampled observations within the dataset.

Figure 2.7 compares the smoothed output from each of the two example Rita simulations to Rita's best-track observations that were shown in Fig 2.5. Periods of simulation prior to Rita's observing period are denoted differently to represent V_{max} less than 18 m s^{-1} (dashed) or V_{max} greater than 18 m s^{-1} but prior to Rita's observations (pale, thin). The bold portions between 11Z 19 Sep 2005 and 05Z 21 Sep 2005 will be the primary focus of the comparison between simulations and observations (hereafter the comparison period).

In each simulation, the evolutions of P_{min} and V_{max} show very similar behavior to each other (Fig. 2.7a-b). Prior to the comparison period, both simulations intensify at nearly identical rates. At the beginning of the comparison period on 19 Sep 2005, there is also good agreement between both simulations and both the Best-Track P_{min} and FLIGHT+ V_{max}. However, on 20 Sep 2005, the small-bogus simulation begins to intensify more rapidly than both the big-bogus simulation and observations, and the small-bogus simulation remains most intense for the remainder of the simulation time. However, the big-bogus also intensifies but shows signs of an eyewall formation. After completing the eyewall formation, the big-bogus simulation intensifies at a rate and intensity similar to observations with respect to P_{min}, but V_{max} becomes much more intense than FLIGHT+ azimuthal average on 21 Sep 2005. Overall, the simulation intensities appear to either be reasonably close to observations or an overestimate.

In terms of ϕ and fullness, the big- and small-bogus simulations exhibit similar behavior but different magnitudes during the main comparison period (Fig. 2.7c-d). While both simulations have smaller ϕ and fullness on 19 Sep 2005 than observations suggest, the small-bogus simulation quickly develops a higher ϕ. In contrast, the big-bogus simulation has a lower ϕ but similar fullness. Both simulations show an interesting ϕ and fullness evolution that is similar to the observations but with different magntitudes. RMW and M_{max} also follow similar evolution at different magnitudes between the big- and small-bogus simulations (Fig. 2.7e-f). While both simulations initially contract to an RMW that is too small, the big-bogus simulation magnitudes of RMW and M_{max} end up much closer to FLIGHT+ observations than the small-bogus simulation. These results highlight the persistent impact of the initial TC size on TC evolution, as shown in Tao et al. (2020); Martinez et al. (2020).

Finally, R_{34} for the big- and small-bogus simulations start out too small at the beginning of the comparison period (Fig. 2.7g). However, the outer-core expansion in the big-bogus simulation becomes similar to observations around the 20th, and then expands too quickly afterward. The small-bogus simulation has too small of an outer wind field for the entire simulation, but evolves to just under the observed magnitude around 10Z 21 Sep 2005. However, the rate of expansion in the small-bogus simulation is quite fast compared to observations.

Overall, while neither of the simulations were a perfect representation of Rita's evolution, Fig. 2.7 shows that the big-bogus simulation is closer to observations. However, it is hard to sep-

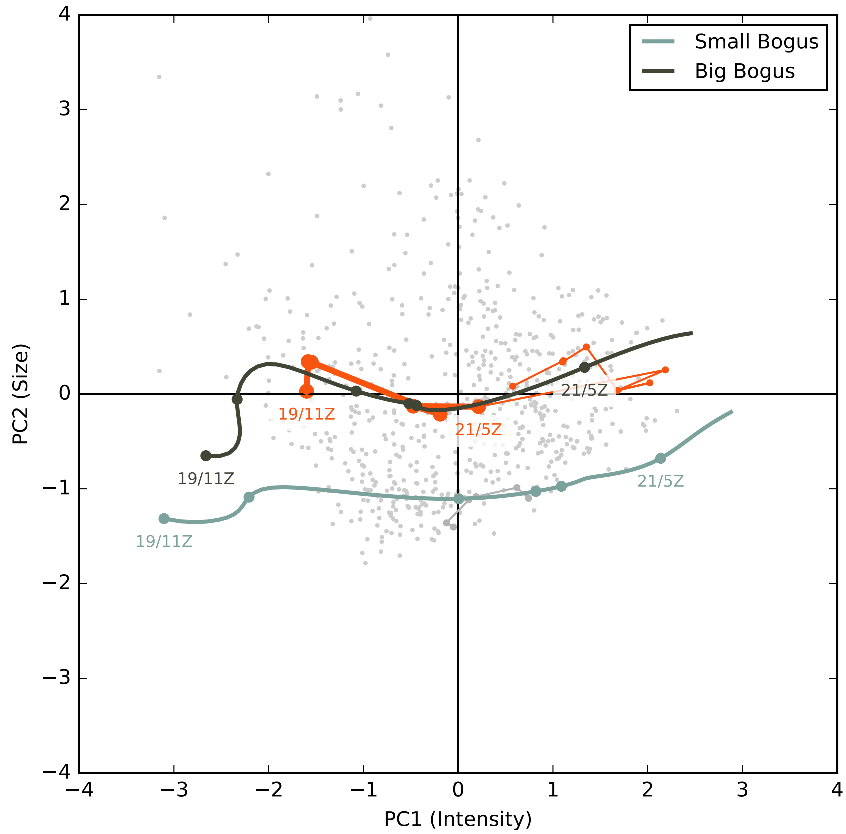

Figure 2.8: Projections of the big- and small-bogus simulations onto the coordinates shown in Fig. 2.6. The big-bogus simulation is shown in dark blue and the small-bogus simulation is shown in light-blue. Times prior to Rita's observing period have been omitted, but the initial conditions for each simulation are (-5.5, 1.0) for the small-bogus simulation and (-5.0, 2.1) for the big-bogus simulation. Day and hour of first and last observation within the comparison period have been labeled. Small gray points are identical to Fig. 2.6b.

arate redundant vs. important information in seven panels of comparisons. Figure 2.8 shows how the two simulations project onto the same coordinates as originally shown in 2.6. In this format, it becomes much easier to quickly distill the differences between the two simulations. At a glance, we can see that the big-bogus simulation is larger PC2 at all times than the small-bogus simulation during the comparison period, but the big-bogus simulation is fairly accurate in terms of PC2 size. In addition, we see that the initially big storm remains big with PC2 size. We can also see that the overall structure during the comparison period starts out too weak and ends too intense.

Both simulations show evidence of eyewall formation at the beginning of the comparison period, with a pause in intensification and increase in size that is similar to observations but in a different part of the phase space. The eyewall formation happens at a much weaker PC1 intensity and smaller PC2 size than Rita's observations would suggest. After that, both simulations slowly contract as they rapidly intensify. Coincidentally, the small-bogus simulation appears to be initialized at an appropriate size for a Charley simulation instead of a Rita simulation, and we can see that the combination of initial conditions led to a small TC compared to observations of Rita. By the end of the comparison period, we can see that the small-bogus simulation has intensified far too quickly with respect to Rita's observations, and that PC1 for 05Z 21 Sep 2005 in the small-bogus simulation is 2 standard deviations more intense than observations. While the initial evolution of the big-bogus simulation is too weak and too small at 11Z 19 Sep 2005, it is clear that the PC2 size after that adjustment then closely resembles Rita's observations. However, the simulated storm intensifies too quickly and the PC1 intensity still winds up being 1 standard deviation larger than the observation at 05Z 21 Sep 2005.

Overall, Fig. 2.8 shows the same conclusions as Fig. 2.5, but in a more concise way. We can see that the big-bogus simulation structure resembles observations the closest, but it is too intense at the end of the simulation. In addition, when combined with the scatter of observed TC variability, we can gain historical context to the curves and quickly identify when there are abnormal intensity-size relationships. While time is implicit in this phase space and must be annotated separately, one can quickly see a holistic TC structural evolution in a single curve. The EOF phase space allows TC researchers and forecasters to quickly identify specific features and examine them in the context of observed variability.

2.4 Discussion and Conclusions

In this study we have used aircraft and best track observations to calculate an empirical orthogonal function (EOF) analysis and create orthogonal axes for intensity and size. Through the EOF analysis we have reduced a 7-parameter space into a simplified, orthogonal, 2D phase space, where PC1 is primarily associated with intensity, and PC2 is primarily associated with size. We also defined a new parameter, ϕ, which is a simple way to characterize vortex radial wind decay. Since our new parameter ϕ primarily corresponds with PC3, we believe that it provides additional information on TC structure and maturity.

However, while our principle components are primarily associated with either intensity, size, or maturity, we note that each principle component incorporates some information from the other two attributes. For example, PC1 and "maturity" are related through components of ϕ and fullness, and PC1 also incorporates some size information from RMW and R_{34}. PC2 also retains some intensity information from P_{min} and "maturity" information from ϕ and fullness, as well. However, a benefit of this EOF analysis is that it shows how the seven metrics covary together in such a way that the variability cleanly separates into ways that can be interpreted as intensity and size.

To demonstrate our new intensity-size coordinates, we first compared the well-known storms of Hurricanes Charley (2004) and Rita (2005) within our dataset. When examining individual parameters, we can see noticeable differences in size, but only minimal differences in intensity for the majority of both intensification periods. However, trying to comprehend the various relationships between all seven parameters is challenging. But when plotting onto the EOF phase space, it is more easily apparent that Charley was one of the smallest and more intense TCs in the historical record, while Rita was an averaged size TC that traversed a wide range of PC1 and PC2 values as it intensified, underwent an eyewall replacement, and ultimately weakened.

In addition to comparing observed structure and evolution, we have also demonstrated that simulated structure can be regressed onto these axes for model validation. When comparing two simulations of Rita with initially small and big bogus vortices with best track observations, it is quickly apparent that Rita's initial intensity is similar in both cases but the small-bogus vortex simulation was too small. By increasing the initial RMW, the big-bogus simulation became more in-line with the observed structure and evolution. Both simulations intensified too quickly compared to observations however.

While we have only demonstrated the utility of this framework with deterministic models, this framework could also help distill key structural differences in ensemble runs. The framework could help forecasters more quickly assess deterministic or ensemble simulations, and also allow the ability to quickly put new forecasts and observations into historical context. Researchers can use this framework to diagnose key structural and intensity changes and run more accurate case study simulations. Idealized structures can also be compared to real TCs in this framework to determine their realism. For future work, this framework can also be used to assess how internal structure variability affects contraction, intensification, and other structural evolution in TCs.

Chapter 3

Variability in Analytic Tropical Cyclone Wind Profiles

3.1 Introduction

Analytic TC wind profiles are used in a wide variety of important applications, including as an initialization for real-time storm surge forecasts from landfalling TCs (e.g. Peng et al. 2006), engineering impact studies (e.g. Powell et al. 2005), historical TC reconstructions (e.g. Boose 2004), and as idealized model initializations that yield insight towards TC dynamics and physical processes (e.g. Kepert 2001; Williams Jr. 2015). In this study, analytic wind profiles are constructed using a reduced set of parameters derived from the EOF phase space in Chapter 2. The essential variability derived from the principal components of observed wind fields is therefore expanded back into physical space in order to further investigate the relationships between structure and intensity change. While many different analytic profiles have been proposed over the years and are optimized for different usages, two of the most commonly used "families" of TC wind profile-fitting methods have been developed by Greg Holland (Holland 1980, 2008; Holland et al. 2010) and Hugh Willoughby (Willoughby and Rahn 2004; Willoughby et al. 2006). These methods can create realistic axisymmetric radial profiles of winds from a small set of parameters. A brief overview of key features, weaknesses, and differences of these methods will be summarized below.

The original Holland method detailed in Holland (1980) was developed as a way to construct simplified, physically-based vortices that better resembled aircraft observations when compared to prior analytic formulations. The method has been steadily updated since original publication to provide better fits to observed data (Holland 2008; Holland et al. 2010). A hallmark of this "family" of methods is that it contains a rectangular hyperbolic form of the radial pressure variation, first given by the form

$$r^B \ln\left(\frac{p_n - p_c}{p - p_c}\right) = A, \tag{3.1}$$

where A and B are scaling parameters, p_n is the environmental pressure, p_c is the minimum central TC pressure, and p is the pressure at radius r. From this pressure variation, the wind profile is derived from a combination of cyclostrophic balance from the eye to the tangential wind maximum (V_{max}), and gradient wind balance radially outward. The cyclostrophic and gradient wind regimes are connected such that $\partial V/\partial r = 0$ at the RMW.

However, one drawback of this original 1980 formulation is that the radial vorticity gradient radially inward from V_{max} changes sign from positive to negative, which satisfies the condition for barotropic instability in the eye. As a result, simulations based on this vortex may experience enhanced eye-eyewall mixing and vortex breakdown (Williams Jr. 2015). Another drawback is that the Holland method tends to systematically (1) overestimate the width of the eyewall wind maximum, and (2) force the wind to decrease too sharply both radially inward and outward from V_{max} (Willoughby and Rahn 2004; Willoughby et al. 2006). As a result of these drawbacks, the Holland profile method has been steadily improved over time to better represent observed TC structure (Holland 2008; Holland et al. 2010). In this study, we will use the most recent 2010 formulation, which will be further described in Section 3.2.

Alternatively, the Willoughby "family" of profile-fitting methods propose a different solution to the aforementioned drawbacks which removes the physical balance constraints in favor of a set of piecewise functions that can more accurately fit aircraft observations (Willoughby and Rahn 2004; Willoughby et al. 2006). With this approach, the increase in wind speed within the eye is described by a power law function, the decay of wind with radius outside the RMW is described by exponential decay, and a polynomial ramp function smoothly connects the two regimes near V_{max} (Willoughby et al. 2006). Additionally, the exponential decay outside the RMW may be described by either a single exponential decay length scale or a weighted combination of a short decay length scale near V_{max} and a long decay length scale at further radii.

The flexibility of this method allows for very accurate fits to full aircraft radial profiles of wind. In this study, we will use a simplified version of the dual exponential decay Willoughby method, which will be further introduced in Section 3.2.

While the Holland method produces a ring-like vorticity structure that satisfies the Rayleigh condition for barotropic instability (Shapiro and Montgomery 1993), the Willoughby profile produces a monotonic Gaussian shaped profile of vorticity in the eye that is stable to finite-amplitude perturbations. However, the Willoughby profile can have different dynamical problems depending on the parameters used to construct the wind field. For example, the power law portion within the eye produces a singularity at the TC center when the fitted exponent $n < 1$, such that there is infinite vorticity and angular velocity at $r = 0$ km. Such a profile can potentially cause numerical instabilities if used to initialize a numerical weather prediction model.

In contrast to the Holland and Willoughby methods that aim to accurately fit aircraft observations, alternative idealized vortices that are often used to initialize full-physics numerical weather simulations sacrifice some realism in favor of stability. One of the most commonly used initial "bogus" vortex in full-physics simulations is based on a modified Rankine vortex. In a pure Rankine vortex, vorticity is constant from the center out to the RMW, and then irrotational at larger radii. However, TC structure is generally not a purely Rankine vortex, so Rankine profiles are typically modified with a decay parameter, such that

$$V(r) = \begin{cases} r & r \leq r_{v_m} \\ r^{-\alpha} & r > r_{v_m} \end{cases}, \tag{3.2}$$

where α denotes the wind decay outside the RMW. An α of 1.0 results in a pure Rankine vortex, and smaller values result in a slower wind decay. The α parameter is directly related to the ϕ parameter introduced in Chapter 2, which defines the wind decay as an angle relative to the change in normalized angular momentum. While α has been shown to vary with intensity (Mallen et al. 2005), the value is often fixed in operational models in favor of varying V_{max} and

RMW to describe the vortex. Due to the simplicity and numerical stability the modified Rankine vortex is commonly used, but it is unclear whether these parameters can fully represent the structural heterogeneity found in nature. The suitability of this vortex structure for simulating observed wind profiles will be examined along with the methods developed by Holland and Willoughby in this study.

In this study, we seek to answer the following science questions:

1. What are the strengths, weaknesses, and dynamical implications for the TCBL for different analytic wind profiles?

2. Is the choice of a particular analytic TC profile more or less important than the location in EOF phase space?

3.2 Wind Profile Construction

In this study, we first use the EOF framework developed in Chapter 2 to construct idealized profiles that represent the majority of the intensity-size EOF phase space. We then assess the boundary layer response to different wind profiles with a slab TCBL model.

3.2.1 Constructing Idealized Wind Profiles

To construct the idealized wind profiles, we first follow the same method of constructing the first two principle components (PCs) from Ch. 2, which describe TC intensity and size. These two PCs are then stratified into 0.5×0.5 bins from $-1.5 \leq PC1 \leq 1.5$ and $-1.5 \leq PC2 \leq 1.5$, as shown in Fig. 3.1. In our dataset, this range covers close to 80% of the aircraft observations. If we assume a normal distribution and that the observed space is undersampled, this domain of interest represents nearly 87% of the variability of the potential intensity-size phase space. We note that Fig. 3.1a shows that no observations exist within the lowest-right bin. Therefore, that lowest-right bin was excluded from further analysis due to a lack of data.

For clarity, we sequentially label the bins from left-to-right and top-to-bottom, as shown in Fig. 3.1b. Note that bins containing 10 observations or less are color-coded with white text, and bins with over 10 observations have black text. The shading denotes the number of observations within each bin that ranges from 2–34 flight passes. Finally, red-orange squares highlight the bins numbered 7, 10, 25, and 28 because these bins will be highlighted as examples within each quadrant throughout this chapter.

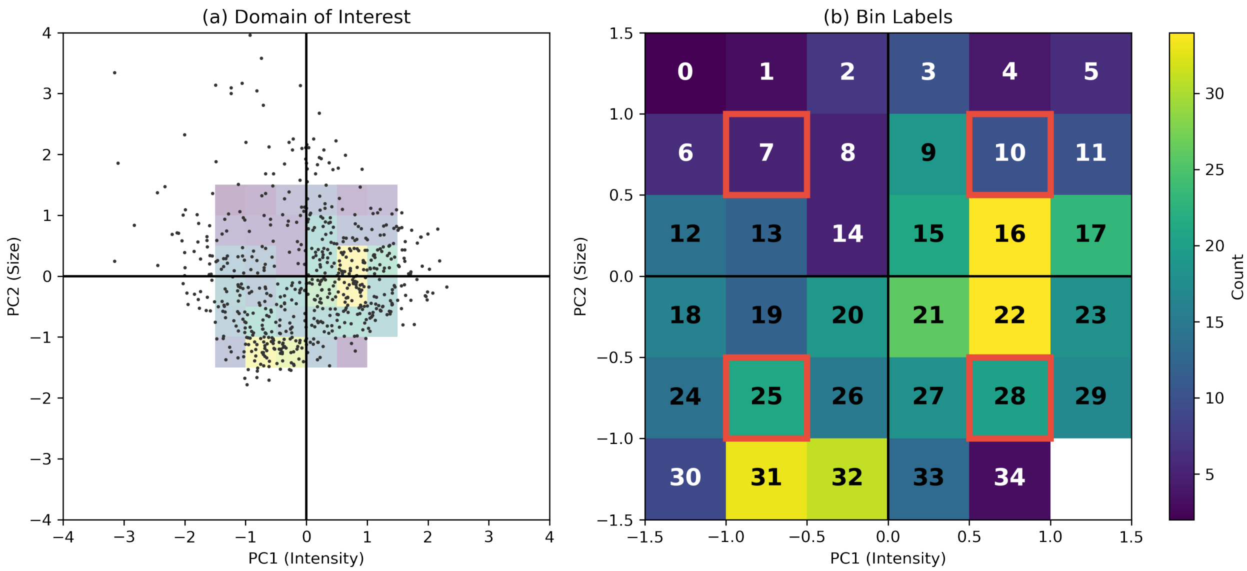

Figure 3.1: (a) As in 2.4, but showing the bins used in this analysis relative to the original observations. (b) Bins with their numerical labels in text, and count of observations in shading. Note that the text color is white for bins with less than or equal to 10 observations, and the text color is black for bins with over 10 observations. Red squares denote the bins that are shown as detailed examples in subsequent figures.

To construct the profiles, we first compute the average of each of the seven EOF parameters within each bin (Fig. 3.2). The computed averages within each bin show a smooth gradient from low to high values, with a slight exception of ϕ, since that parameter projects most strongly onto PC3 and is therefore more orthogonal to intensity and size than the rest of the parameters. We note that the gradients align with the eigenvectors shown in 2.6 by construction of the EOF analysis.

To get a sense of how much each bin mean is representative of the distribution present within its respective bin, the standard deviations within each bin have also been computed (Fig. 3.3). In general, standard deviations are low, but Bin 7 has more variability than the others in terms of size and maturity metrics (Fig. 3.3c-d). We can also see that TCs with positive PC2 values have slightly greater variability in terms of M_{max} and R_{34}, and TCs with negative PC1

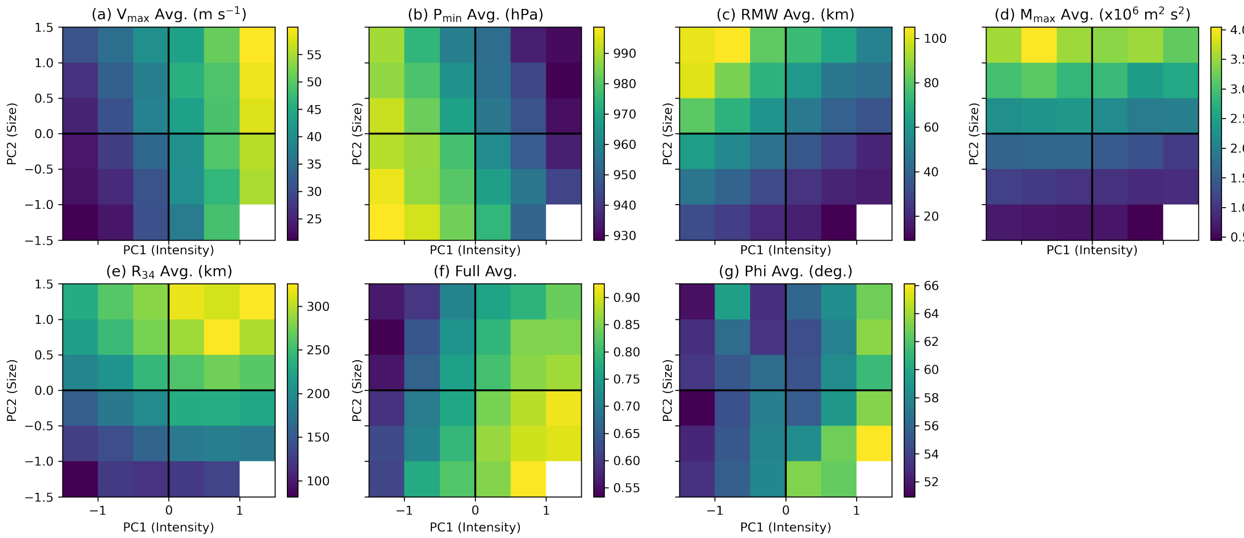

Figure 3.2: Means of observations within the bins described in 3.1, for (a) V_{max} (m s^{-1}), (b) P_{min} (hPa), (c) RMW (km), (d) M_{max} (x 10^6 m^2 s^{-2}), (e) R_{34} (km), (f) Fullness, and (g) ϕ (deg.).

values have greater variability in terms of fullness. However, the standard deviations are low enough that we believe the mean values are generally representative of each bin.

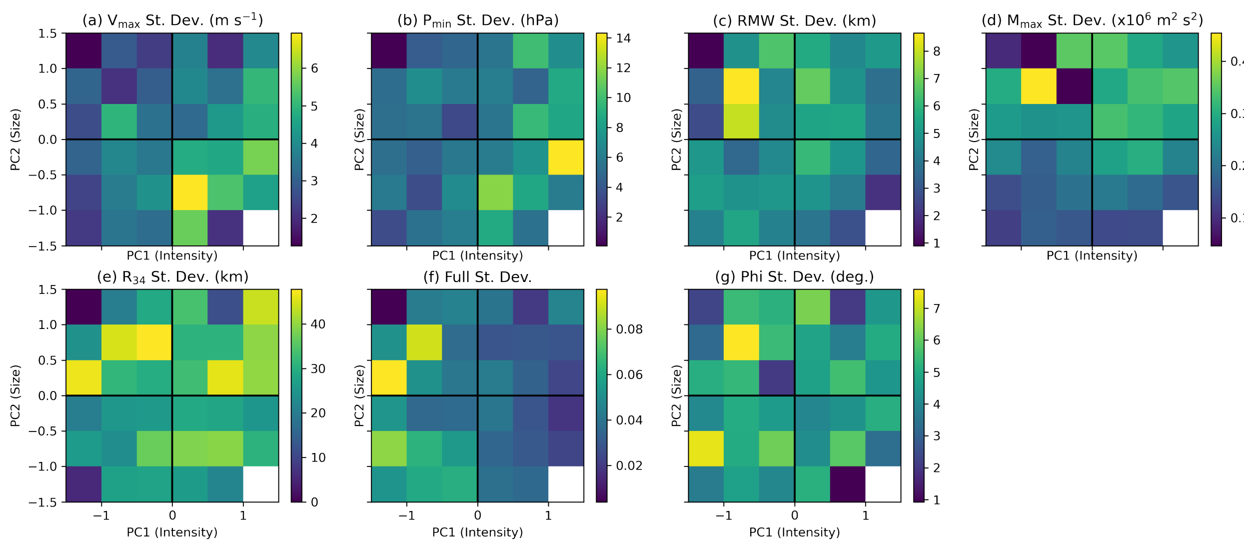

Figure 3.3: As in 3.2, but for the standard deviations within each bin.

The next step in constructing the idealized wind profiles is to use the bin averages to determine the most salient features of profiles within each bin. The four key parameters that are considered to define the mean profile that is being fitted are:

1. The tangential wind speed at the TC center, which is assumed to always be zero ($V(r = 0) = 0$ m s^{-1}),

2. The bin-average V_{max},

3. The tangential wind at 2RMW, which is derived from the definition of ϕ and the bin-average RMW, M_{max}, and ϕ values (Eq. 2.1),

4. The Best Track R_{34}, which is assumed to be apply to flight-level such that the axisymmetric flight-level tangential wind speed of 34 kts occurs at the same radius as the radius where the Best Track sustained surface wind speed is 34 kts,

From these four "anchor" points, we then use three different methods of curve-fitting: the Holland method (Holland et al. 2010), the Willoughby method (Willoughby et al. 2006), and a new method that is based on our definition of ϕ from Ch. 2. Both the Holland and Willoughby methods are commonly used in hazard impact forecasts and modeling studies, and our new method is closer to a modified Rankine vortex. It will be shown that all three methods can produce wind profiles that are within the envelope of observed profiles in each bin (c.f. Fig. 3.5). The equations that define each wind profile fitting method follow.

Holland Method

The 2010 Holland method is defined as the set of equations:

$$v_s = \left[\frac{100 b_s \Delta p_s \left(\frac{r_{vms}}{r}\right)^{b_s}}{\rho_s e^{\left(\frac{r_{vm}}{r}\right)^{b_s}}} \right]^x \text{, where} \tag{3.3}$$

$$p_s = p_{cs} + \Delta p_s e^{-\left(\frac{r_{vm}}{r}\right)^{b}}, \tag{3.4}$$

$$b_s = \frac{v_{ms}^2 \rho_{ms} e}{100(p_{ns} - p_{cs})}, \text{ and} \tag{3.5}$$

$$x = \begin{cases} 0.5 & r \le r_{v_m} \\ 0.5 + (r - r_m)\frac{x_n - 0.5}{r_n - r_{vm}} & r > r_{v_m} \end{cases}, \tag{3.6}$$

where v_s is the tangential wind, p_s is the pressure, and b_s and x are scaling parameters. (finish describing)

In this study, we assume that p_{ns} = 1010 hPa, and we minimize the absolute error at the four anchor points to determine the optimal value of x_n.

Willoughby Method

In the study, we use the dual-exponential form of the Willoughby method, which is defined as

$$V(r) = \begin{cases} V_i = V_{max}\left(\frac{r}{R_{max}}\right)^n, & 0 \le r \le R_1 \\ V_i(1-w) + V_o w, & R_1 \le r \le R_2 \\ V_o = V_{max}\left[(1-A)\exp\left(-\frac{r-R_{max}}{X_1}\right) + A\exp\left(-\frac{r-R_{max}}{X_2}\right)\right], & R_2 \le r \end{cases} \tag{3.7}$$

where V_i represents the inner tangential velocity profile, V_o represents the outer tangential velocity profile, and w is a weighting factor that blends the two curves together in an intermediate zone around the RMW. In V_o, A is another weight that blends the two exponential decay lengths (X_1 and X_2) together.

In this study, we have assumed that the shorter exponential decay length is the RMW, and the longer decay length is R_{34}. The exponent n determines the profile shape in the eye, and n, w, and A are optimized by minimizing the error to the four "anchor" points.

Angular Momentum Method

Our new method of fitting winds (hereafter the Angular Momentum method) is defined in the same axes as our definition of ϕ, in terms of normalized radius and normalized absolute angular momentum, such that

$$V(r)=\begin{cases} M^*\,(r^*)^2 & r \le r_{v_m} \\ \left(\frac{M_m}{r}\frac{M_{34}^*-1}{r^*-1}\right)-0.5\bar{f}r & r > r_{v_m} \end{cases}, \tag{3.8}$$

where M denotes absolute angular momentum, r denotes radius, asterisks denote normalization by a variable's respective values at V_{max}, and the $\bar{f}$ denotes the bin-average Coriolis parameter. In this phase space, angular momentum profiles are assumed to vary linearly from the RMW at point (1,1) to the normalized angular momentum at R_{34}.

The profiles are then converted to tangential wind using the definition of absolute angular momentum and the Coriolis parameter derived from each profile's V_{max}, RMW, and M_{max} and averaged within each bin.

An example of the angular momentum profiles fit through the four anchor points is shown in Fig. 3.4. In the example bins of 7, 10, 25, and 28, the fit is nearly exact for weaker TCs. The 2RMW anchor point is slightly above the line in the stronger vortices, but the overall correspondence to the anchor points is good despite the simplification to a linear profile.

One benefit of this simple method is that it can potentially be derived solely from data that are preserved in the extended Best Track dataset: the Best Track intensity, the RMW, the R_{34}, and the latitude. A user only needs to assume a scaling parameter between the Best Track surface intensity and the flight-level tangential wind speed. In the current case, we use the flight level V_{max} and RMW along with the Best Track R_{34}. Future work will investigate the uncertainty of solely deriving idealized profiles from Best Track data.

3.3 Wind Profile Comparisons

The resulting reconstructed profiles for all three methods in each example bin are compared to their respective anchor points and original azimuthally-averaged profiles in Fig. 3.5. Results show that both the anchor points and idealized profiles lie within the envelope of variability, which indicates that they are all potentially representative of the observed profiles within each

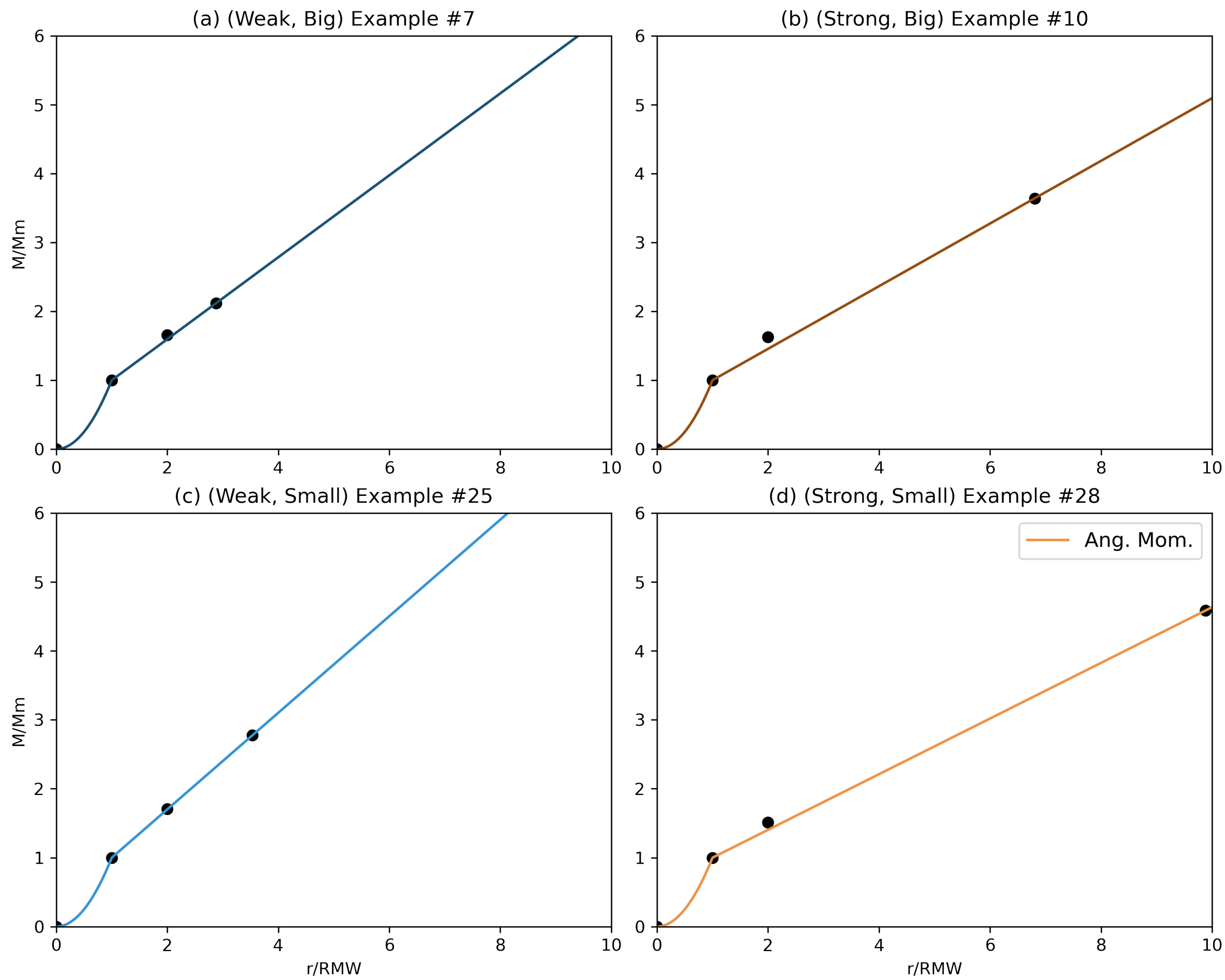

Figure 3.4: Examples of how the Angular Momentum method is constructed for the bins highlighted in red in Fig 3.1. The x-axis is the radius normalized by the RMW, and the y-axis is the absolute angular momentum normalized by its value at the RMW. Color shading refers to the PC2-size, and color hue refers to the PC1-intensity, and is consistent with subsequent figures.

bin. The differences between the three methods retain some of the observed variability within the bin, especially for the smaller storms with negative values of PC2 (Fig. 3.5c-d). Figure 3.5 also indicates that each method appears to be better suited for different quadrants of the EOF phase space. When comparing the simplified profiles to observations, the Angular Momentum method appears to be the best fit for weak, small storms; the Holland method appears to be the best fit for weak, big storms; and the Willoughby method appears to be the best fit for strong, big storms. However, we note that the simplifications made to the Holland and Willoughby methods may not represent the most ideal fits these methods can produce. In particular, using R_{34} as the longer exponential decay length in the Willoughby method does not appear to be ideal for very weak and small TCs.

Calculating the root mean square error (RMSE) of each simplified profile to the four anchor points confirms the indication from Fig. 3.5 that each method has different strengths and weaknesses for a given TC structure (Fig 3.6). Results show that the Angular Momentum method has the lowest RMSE for weak, small TCs, and highest RMSE for strong, big TCs (Fig 3.6a). In contrast, the Holland method has the lowest RMSE for weak, average size TCs, and highest RMSE for strong, small TCs (Fig 3.6b). Finally, the Willoughby method has the lowest RMSE for strong, average size TCs and highest RMSE for weak, small TCs (Fig 3.6c). Again, we note that both the Holland and Willoughby methods are designed to be used with the full azimuthal averages, so the deficiencies of each method can potentially be mitigated with additional parameter tuning. However, while each method has slightly better fits for different regions in the EOF phase space, the RMSE is low enough that all profiles are generally representative of the TC structure that is being reconstructed.

While all three methods fit reasonably well to the anchor points and full azimuthally-averaged profiles, there are considerable dynamical ramifications of each method. In particular, the vorticity for each method within the example bins is shown in Fig. 3.7. The Angular Momentum method most closely represents a “Rankine-like” structure. The Holland method represents a “ring-like” structure, and the Willoughby method represents a “Gaussian-like” structure. As de-

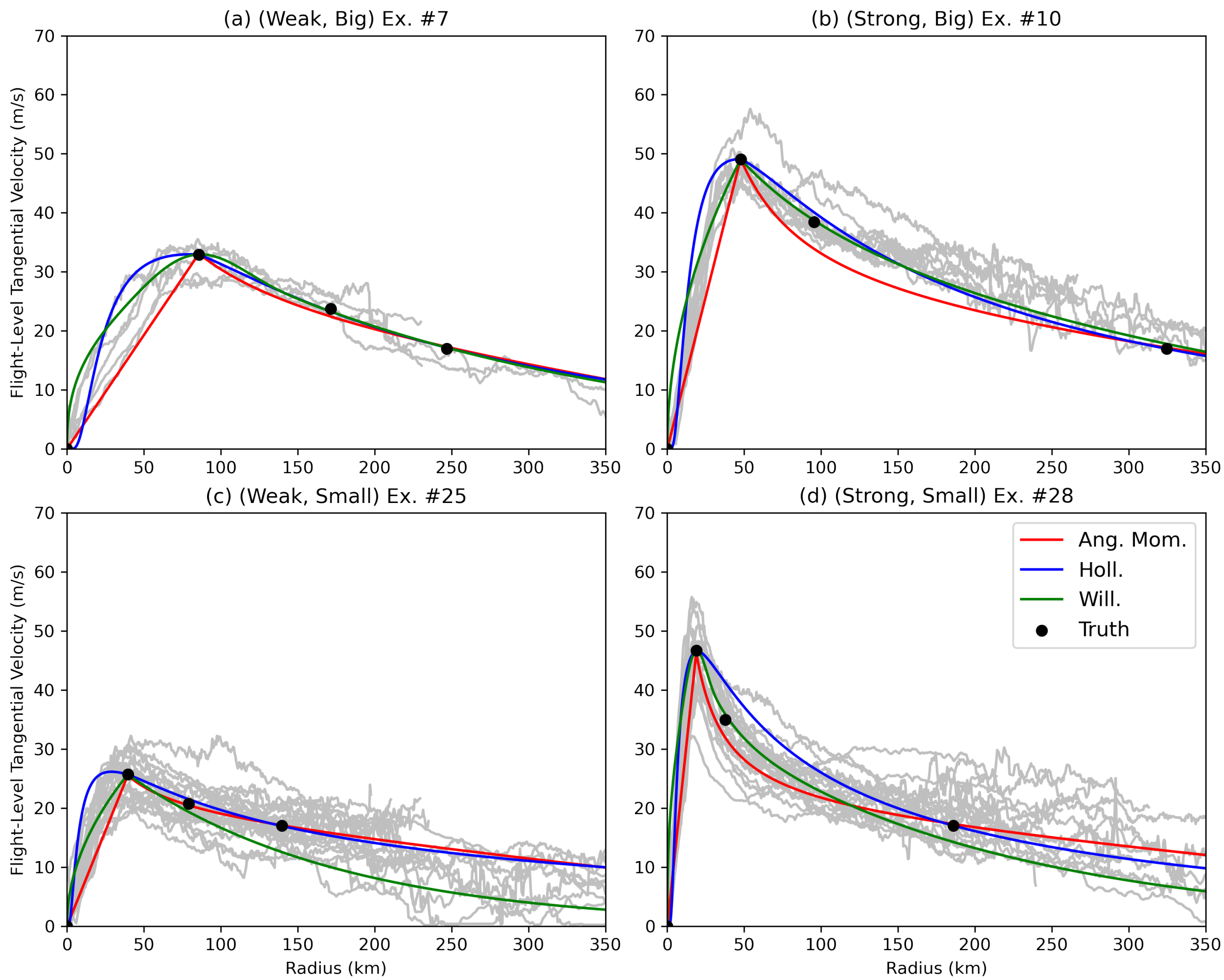

Figure 3.5: Comparison of the three methods of idealized profiles of flight-level tangential wind to their anchor points and all of the complete azimuthally-averaged tangential wind profiles (gray) within each example bin. The Angular Momentum method is shown in red, the Holland method is shown in blue, and the Willoughby method is shown in green.

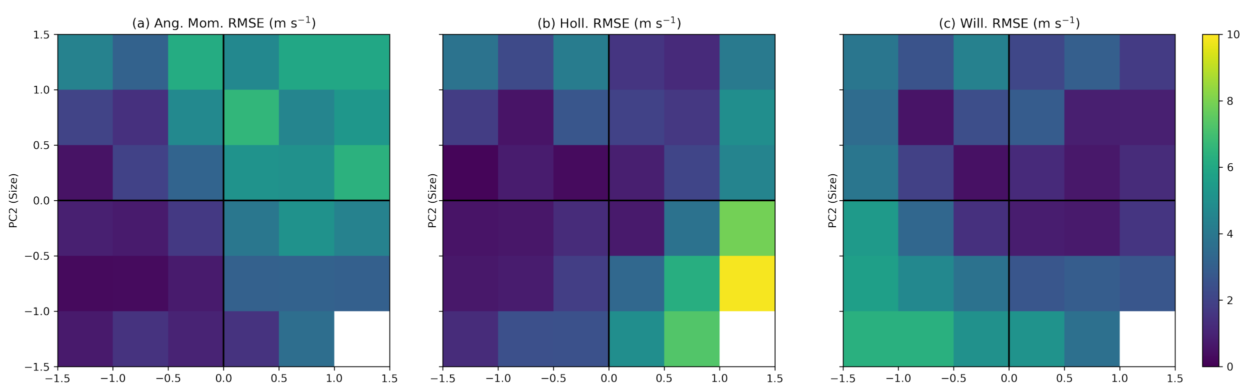

Figure 3.6: Root mean square error (RMSE) of each method to the "anchor" scatter points shown in Fig. 3.5 for (a) the Angular Momentum method tangential wind (m s^{-1}), (b) the Holland method tangential wind (m s^{-1}), and (c) the Willoughby method tangential wind (m s^{-1}).

scribed in Section 3.1, the vorticity profiles indicate that the Holland method is susceptible to barotropic instability, the Willoughby method is susceptible to numerical instability in simulations, and the Angular Momentum method is not susceptible to instabilities.

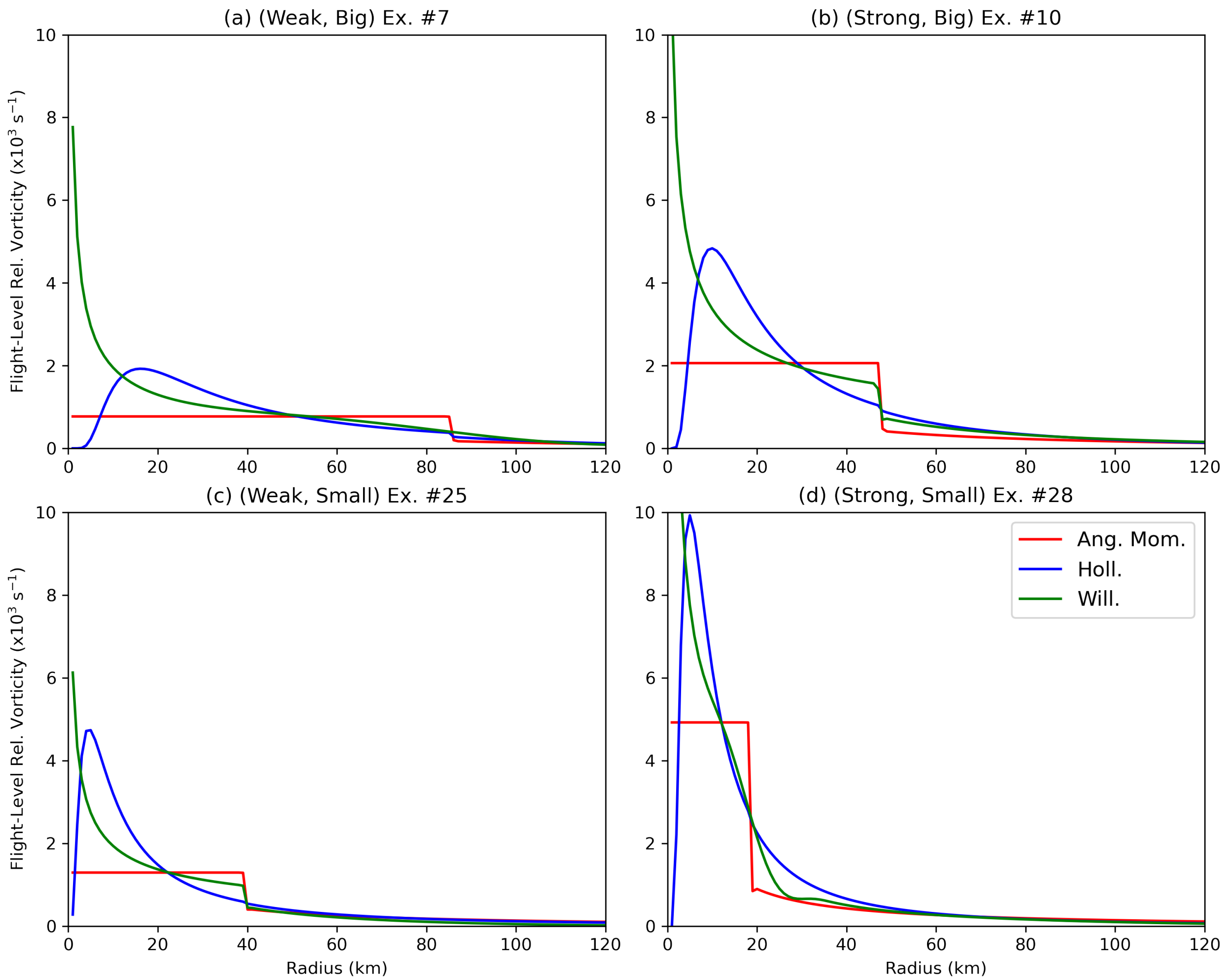

Figure 3.7: Profiles of relative vorticity ($\times 10^3$ s^{-1}) for each method within each example bin.

3.4 Discussion and Conclusions

In this study, we sought to first assess the strengths and weaknesses of the Angular Momentum, Holland, and Willoughby methods for a wide variety of TC structures. The Angular Momentum method proposed in this study has the benefit that it is very simple and can be solely derived from commonly observed variables in the Best Track dataset. In addition, the vorticity profile is most “well-behaved” in numerical simulations when compared to the Holland and Willoughby methods. This study finds that the Angular Momentum method is particularly well-suited for weak, small TCs, and least suited for strong, big TCs.

The Holland method has the benefit that it relates pressure and wind together in a physically-based framework, and it is the most commonly used method. In this study, we find that it is best suited for average, small TCs, and least suited for strong, small TCs.

The Willoughby method has the benefit that it is the most tunable, and can most accurately reproduce aircraft observations. However, with the simplifications used in this study, the Willoughby method is best suited for strong, big TCs and least suited for weak, small TCs.

However, while all three tested methods have different strengths and weaknesses, they all generally lie within observed variability. Therefore, all three are valid representations of an idealized wind field that will continue to be be explored in Ch. 4-5.

Chapter 4

Boundary Layer Response to Analytic Tropical Cyclone Wind Profiles

4.1 Introduction

TCBL structure is important for TC intensification, due in part to its ability to enhance radial inflow and angular momentum convergence, constrain the location of the maximum updraft within the radius of maximum tangential wind (RMW), and more generally spin up the secondary circulation through frictional effects (Kepert 2001). Additionally, the TCBL is also able to directly interact with its environment through fluxes of surface drag and enthalpy, which may either act to spin up or spin down a TC (Bell et al. 2012; Montgomery et al. 2010; Smith et al. 2014).

While many TCBL processes are important, the location of the updraft is particularly important for future intensification, because latent heat release within the convective updraft can be more efficiently converted to kinetic energy when released within the RMW in the balanced vortex model (Eliassen 1951; Schubert and Hack 1982; Shapiro and Willoughby 1982; Pendergrass and Willoughby 2009).

However, there are different mechanisms within the TCBL that may play a role in constraining the location of the maximum updraft. First, Kepert (2017) proposes that the magnitude of the displacement of the updraft radially inward from the RMW is determined by the term u/I, which describes a trade-off between the strength of the radial inflow and the inertial stability. In this term, if either the radial inflow is stronger or the inertial stability is weaker, then parcels that are being advected radially inward within the TCBL inflow are able to penetrate further inward before ascending into the updraft.

An additional TCBL process that may constrain the location of maximum updraft is the possible existence of shock-like structures within the TCBL that constrain the location of the maximum updraft (Williams et al. 2013), but vertical advection may play an important role in diffusing the shock-like structures (Williams Jr. 2015). Therefore, the importance of vertical advection to TCBL dynamics suggests that height-resolved models are important to compare to the more interpretable slab models.

While latent heat release within the updraft of convection is important from an efficiency point of view, within the context of the rotating convection paradigm, enhanced radial inflow due to friction within the TCBL can also act to spin up the vortex if the angular momentum is converged at a rate that is faster than the rate at which angular momentum is destroyed through friction (Montgomery and Smith 2014; Smith and Montgomery 2015).

However, while spinning up the secondary circulation through friction has some positive effects for intensification, there is debate as to whether the positive effects of enhanced radial inflow outweigh the direct spindown from surface drag (Stern et al. 2015). When diagnosed in a linear model, the negative direct effects from friction outweigh the positive effects (Stern et al. 2015). In addition, not only are there direct spindown effects from friction, but unbalanced supergradient tangential flow can produce an outflow jet above the TCBL that can also act to spin down the vortex by advecting absolute angular momentum outward (Torgerson et al. 2022). However, depending on the strength of the outflow jet, it could also simply act to restore the inward "overshoot" of radial inflow back to the radius of the updraft (Montgomery et al. 2014), or be more of a passive adjustment to rapid changes in inflow (Kepert and Nolan 2014).

Despite the many uncertainties that exist regarding internal processes within the TCBL, simplified TCBL models have been shown to be able to generally reproduce full-physics wind structure (Kilroy et al. 2016; Kepert 2013). Therefore, there is a suggestion that the TCBL places a strong constraint on the overlying vortex.

However, an unknown question remains as to how the TCBL responds as a function of TC intensity and size, and whether a TC's size and intensity affect the location of the updraft relative to the RMW. While Williams Jr. (2015) shows a comparison of how slab and height-resolved simulations respond to three stationary, initial vortices, the initial vortices all have a V_{max} = 55 m s^{-1} and an RMW = 40 km, and only a modified Rankine parameter (which is similar to ϕ) is varied. That said, Williams Jr. (2015) shows that as initial TCs become more mature, then the secondary circulation becomes enhanced.

In particular, this study seeks to investigate the sensitivity of the boundary layer response to analytic wind profiles that vary in terms of gradient wind forcing in the free troposphere. The gradient wind forcing drives frictional convergence within the tropical cyclone boundary layer (TCBL) that determines the location of the updraft (Kepert 2017). It is now well established that updrafts that are further radially inward from the RMW are more conducive to intensification (Rogers et al. 2013) through efficient heat conversion to kinetic energy due to increased inertial stability (Schubert and Hack 1982; Pendergrass and Willoughby 2009) and increased advection of angular momentum (Montgomery et al. 2015).

In this study, we seek to investigate the following science questions:

1. How does the TCBL secondary circulation adjust to variations in TC intensity and size?
2. Do the different simplified profiles in Ch. 3 result in highly different TCBL responses, or is the general intensity and size more important?
3. Do certain aspects of TC intensity and size appear to induce a more favorable TCBL response for future intensification?

4.2 Experimental Design

4.2.1 Slab Boundary Layer Response

To test the idealized wind profiles, we use a new tropical cyclone boundary layer (TCBL) model based on the equation set from Williams et al. (2013). In this chapter, the model is set up as an axisymmetric, 1-dimensional model with a single, constant height level, which is commonly referred to as a "slab" TCBL model.

The slab model solves the set of equations used in Williams et al. (2013), which are

$$\frac{\partial u}{\partial t} = -u\frac{\partial u}{\partial r} - w^{-}\left(\frac{u}{h}\right) + \left(f + \frac{v + v_{gr}}{r}\right)\left(v - v_{gr}\right) - c_D U\frac{u}{h} + K\frac{\partial}{\partial r}\left(\frac{\partial (r u)}{r\partial r}\right), \tag{4.1}$$

$$\frac{\partial v}{\partial t} = w^{-}\left(\frac{v_{gr} - v}{h}\right) - \left(f + \frac{\partial (r v)}{r\partial r}\right)u - c_D U\frac{v}{h} + K\frac{\partial}{\partial r}\left(\frac{\partial (r v)}{r\partial r}\right), \tag{4.2}$$

$$w = h\frac{\partial (r u)}{r\partial r}, \tag{4.3}$$

$$\tag{4.4}$$

where u is the radial wind, v is tangential wind in the boundary layer, v_{gr} is the gradient wind above the boundary layer, and w is vertical wind. The 10-m wind speed used to calculate surface fluxes is

$$U = 0.78\left(u^2 + v^2\right)^{1/2} \tag{4.5}$$

and

$$w^{-} = \frac{1}{2}\left(|w| - w\right) \tag{4.6}$$

is the rectified Ekman suction.

For simplicity, we use a constant c_D drag coefficient of 2.4×10^{-3} following Bell et al. (2012). The horizontal diffusion K is set to 1500.0 m^2 s-1 and Coriolis parameter f is set to 5.0 x 10^{-5}. The height of the slab layer is set to a constant 1000.0 meters. Additional details on the equation set can be found in Williams et al. (2013).

The model uses the cubic spline transform method following Ooyama (2002) to integrate the model equations. The cubic spline nodal spacing is 500 m from the origin (0 km) out to 1000 km radius, with 3 Gaussian 'mish' points between each node representing the physical grid. The physical tendencies are calculated on the grid, then transformed to spectral amplitudes for time integration similar to the spectral transform method (Orszag 1970). The integration closely follows Ooyama (2002), including the use of a spline cutoff filter to control numerical noise. The primary difference with Ooyama (2002) is the use of a 3rd order Adams-Bashforth time integrator which provides better numerical stability and numerical accuracy than the second order method (Durran and Blossey 2012). A time step of 1 second is used for the integration.

One advantage of the cubic spine transform over pure spectral methods is the ease of imposing non-periodic boundary conditions. The boundary conditions enforces a Dirichelet zero wind condition at the origin for u, v, and w, and a Neumann zero first derivative at the outer boundary.

Given the minimal computational expense of the 1-D model, we ran every profile calculated in every bin shown in Fig. 3.1: 35 Angular Momentum profiles, 35 Holland profiles, and 35 Willoughby profiles, for a total of 105 slab TCBL simulations.

4.2.2 Height-resolved TCBL model Model Setup

Instead of solving the set of partial differential equations found within Williams et al. (2013), the height-resolved TCBL model adds a vertical dimension and solves the equations from Kepert (2017):

$$\frac{\partial u}{\partial t} + u\frac{\partial u}{\partial r} + w\frac{\partial u}{\partial z} - \tilde{v}\left(f + \frac{\tilde{v}}{r}\right) = -v_{gr}\left(f + \frac{v_{gr}}{r}\right) + \frac{\partial}{\partial z}\left(K_v\frac{\partial u}{\partial z}\right) \tag{4.7}$$

$$\frac{\partial \tilde{v}}{\partial t} + u\frac{\partial \tilde{v}}{\partial r} + w\frac{\partial \tilde{v}}{\partial z} + u\left(f + \frac{\tilde{v}}{r}\right) = \frac{\partial}{\partial z}\left(K_v\frac{\partial \tilde{v}}{\partial z}\right) + K_h\left[\frac{1}{r}\frac{\partial}{\partial z}\left(r\frac{\partial \tilde{v}}{\partial r}\right) - \frac{\tilde{v}}{r^2}\right], \tag{4.8}$$

where u, $\tilde{v}$, and w are the radial, azimuthal, and vertical wind components, respectively; v_{gr} is the gradient wind, and K_h and K_v are the horizontal and vertical turbulent diffusivities, respectively. The height-resolved TCBL model retains the same splines in spectral space in the radial direction. In the vertical, a discretation based on Chebyshev polynomials is used. The Chebyshev polynomials are closely related to Fourier series, and represent a cosine transform of the evenly spaced interval from 0 to π to an uneven interval spanning -1.0 to 1.0 in z. The -1.0 to 1.0 interval in physical space is then transformed from the surface to the top of the boundary layer using a simple linear scaling. Representation of variables through a Chebyshev series provides high numerical accuracy of a field and its vertical derivative through a spectral representation that allows for non-periodic boundary conditions. Additional details on Chebyshev methods can be found in Boyd (2001).

One advantage of the Chebyshev series is rapid convergence of the function with increasing polynomial order compared to finite difference methods. One disadvantage for numerical weather prediction is the non-uniform spatial resolution that can put a severe constraint on the time step required for time integration. The spatial resolution is finest near the boundaries and coarser in the middle of the domain. In the current application we use this feature as an advantage to increase the resolved flow near the surface and near the top of the TCBL. The following simulations use 25 vertical levels on the Lobatto points (extrema plus endpoints) from 0.0 to 2350 meters, such that the second height level is at 10.0 meters altitude for use in the bulk aerodynamic formula for surface drag. No vertical boundary condition is imposed at the surface winds, and a Neumann zero first derivative is enforced at the top of the domain.

The radial boundary conditions are identical to the slab boundary layer model. Due to more computational expense, the radial nodal spacing was reduced to 1 km with an outer boundary of 400 km. Three Gaussian quadrature points were used in between each node for the cubic spline transform similarly to the slab model.

4.3 Results

4.3.1 Slab TCBL Model Results

To test the dynamical implications and boundary layer response for each wind profile derived in Ch. 3, the analytic profiles were used as a gradient wind forcing at the top of the slab TCBL, and the model was run out to 3 hours to calculate the quasi-steady TCBL response to the gradient wind forcing. Longer time integrations were tested and did not change the results.

Examples of the gradient forcing and TCBL response are shown in Fig. 4.1, which shows that stronger and larger TCs have a stronger response to the initial gradient wind forcing. In addition, the Holland method appears to force the strongest supergradient winds within a given part of the EOF phase space. Interestingly, the weak, big example TC shows the greatest variability in terms of quasi-steady RMW and radius of maximum vertical motion (RMWW), despite having the most similar gradient wind profiles outside the initial RMW.

Fig. 4.2 shows that the above example TCBL responses are representative of the responses within the entire EOF phase space of interest. In Fig. 4.2a-c, the adjusted TCBL maximum tangential wind speed (V_{max}) is the largest for the strong, big TCs and smallest for the weak, small TCs for all three methods. Similarly, Fig. 4.2d-f shows that the strongest radial inflow (U_{min}) also occurs for the strong, big TCs, and Fig. 4.2g-i shows that the largest maximum updraft speed (W_{max}) also occurs in the strong, big TCs for all three profile methods.

The locations of the wind maxima are described in Fig. 4.3. While the strongest V_{max} occurred in the strong, big quadrant, Fig. 4.3a-c shows that the most radially outward RMW of those maxima occurred in the weak, big quadrant, and the smallest RMW occurred in the strong, small quadrant.

The radius of maximum inflow (RMWU) is described as distance from the RMW in Fig. 4.3d-f, which shows that the distance of RMWU is furthest radially outward from the RMW for strong, small storms. The distance of RMWU from the RMW is not a smooth gradient, and there is a sharp cutoff between the furthest apart RMW and RMWU in the strong, small quadrant and the closest together RMW and RMWU in the strong, big quadrant for the Angular Momentum method (Fig. 4.3d). In the Holland method, there is a generally smooth gradient where the weak, big storms have a larger distance between RMW and RMWU to most of the strong, small TCs having a narrower distance between RMW and RMWU, with and exception of Bin 34 having the largest distance overall (Fig. 4.3e). Finally, the Willoughby method response is in between the other two methods, where the pattern more closely resembles the Angular Momentum method, but the magnitudes in the Big PC2 quadrants more closely resemble the Holland method (Fig. 4.3f).

The radius of maximum updraft (RMWW) is also shown as distance from the RMW in Fig. 4.3g-i, where red indicates further radially inward from the RMW. All three profile methods are

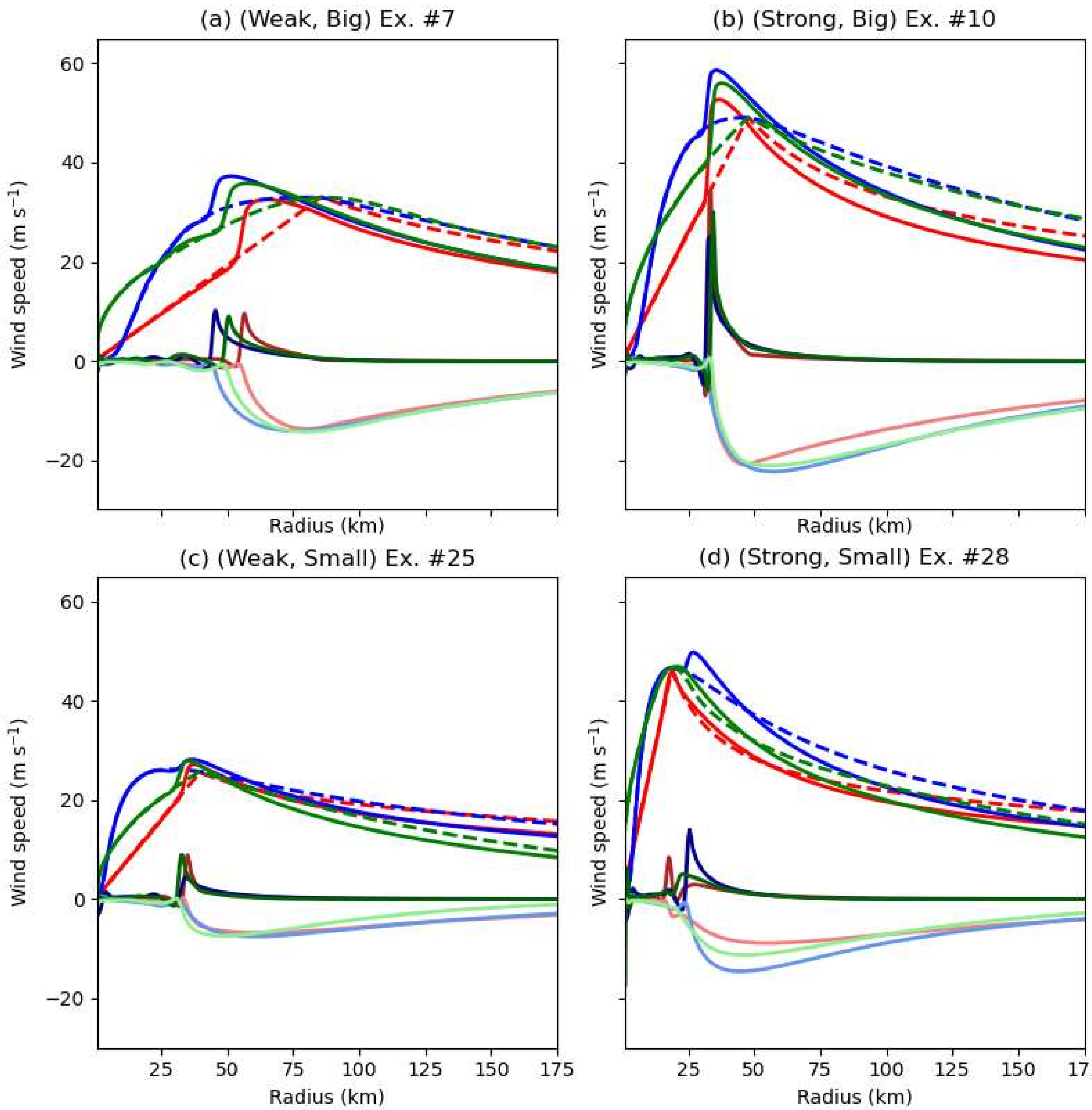

Figure 4.1: Radial profiles of tangential wind speed (m s^{-1}) at 0 hr (dashed, medium shades) and 3 hr (solid, medium shades), radial inflow (m s^{-1}; light shades), and vertical wind speed ($\times 5$ m s^{-1}; dark shades) for each method within each example bin. Red indicates the Angular Momentum method, blue represents the Holland method, and green represents the Willoughby method.

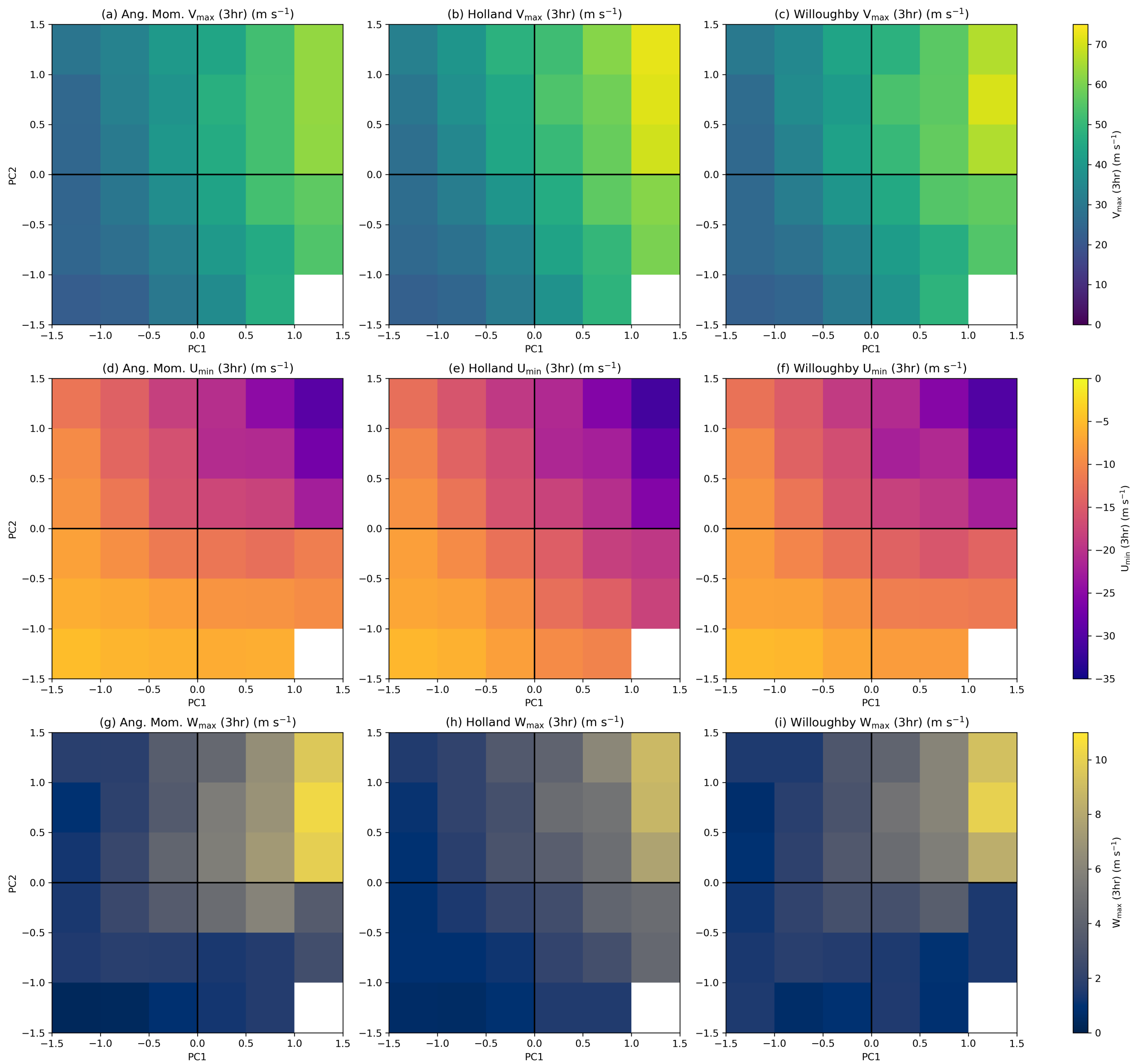

Figure 4.2: Resulting (a-c) maximum tangential wind (V_{max}), (d-f) minimum radial wind (U_{min}), and (g-i) maximum vertical wind (W_{max}) from each slab TCBL model simulation in m s^{-1}. Columns denote the wind profile method, where the first column (a,d,g) represents the Angular Momentum method, the second column (b,e,h) represents the Holland method, and the third column (c,f,i) represents the dual-exponential Willoughby method.

in agreement that the furthest distance between RMWW and RMW occur for weak, big storms, and the two radii become closer together as TCs become either stronger or smaller. However, the strongest, smallest TCs have a secondary updraft maximum outside the RMW, which may suggest that these TCs are favorable for secondary eyewall formations.

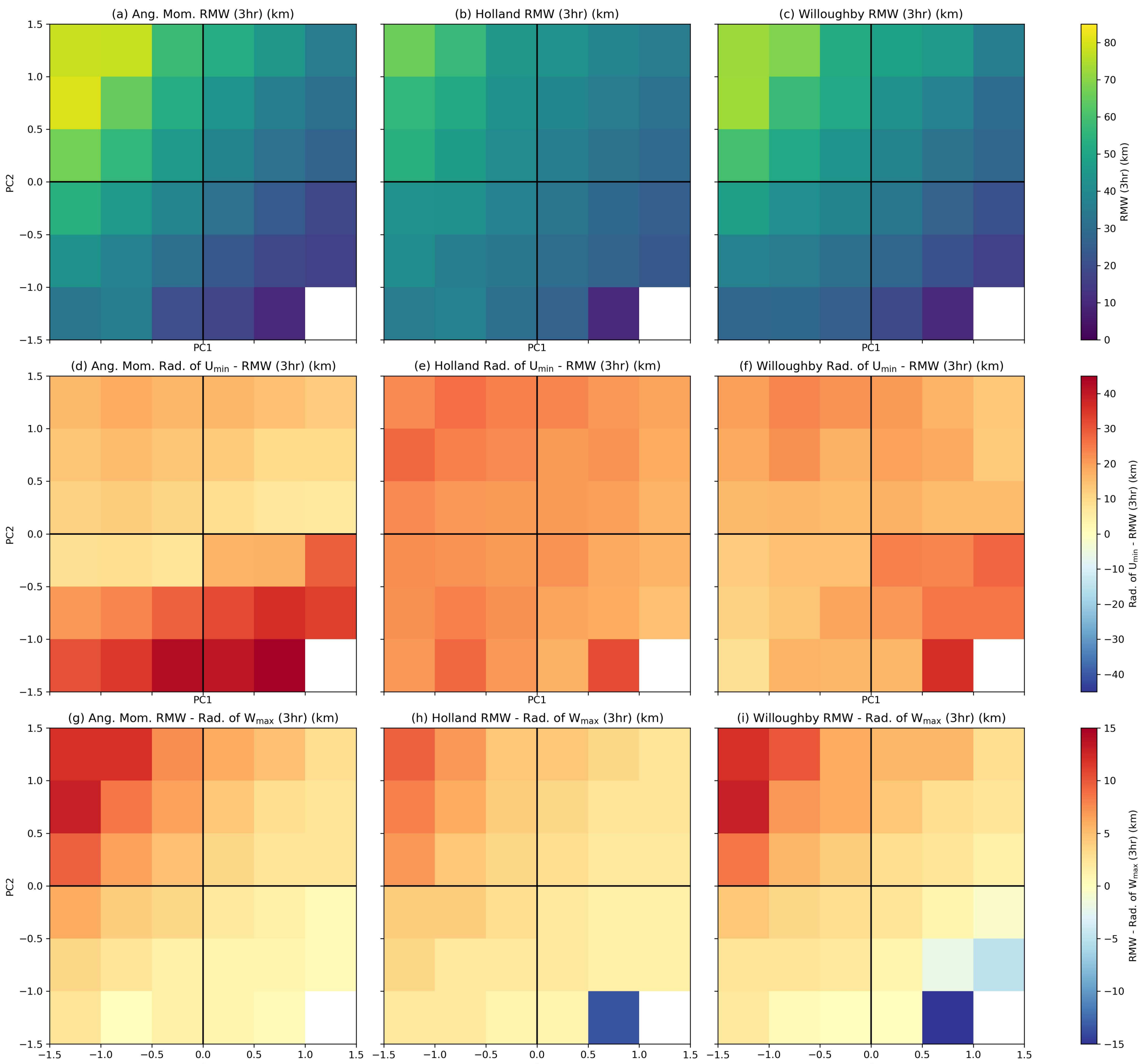

Figure 4.3: As in 4.2, but for (a-c) the radius of maximum tangential wind (RMW), (d-f) the departure of the radius of minimum radial wind from the RMW (RMWU - RMW), and (g-i) the departure of the radius of maximum vertical wind from the RMW (RMW - RMWW) from each slab TCBL simulation in km.

Fig. 4.4 shows how much V_{max} and its RMW changed from the original gradient wind forcing. Fig. 4.4a-c shows that the largest changes of V_{max} occurred for the strong, big TCs, and somewhat for the weak, small TCs. In contrast, the largest contraction of RMW from the original gradient wind forcing occur for the weak, big and some strong, big TCs. Interestingly, the strong, small TCs show either no change or an expansion from the original gradient wind forcing depending on the profile method (Fig. 4.4d-f).

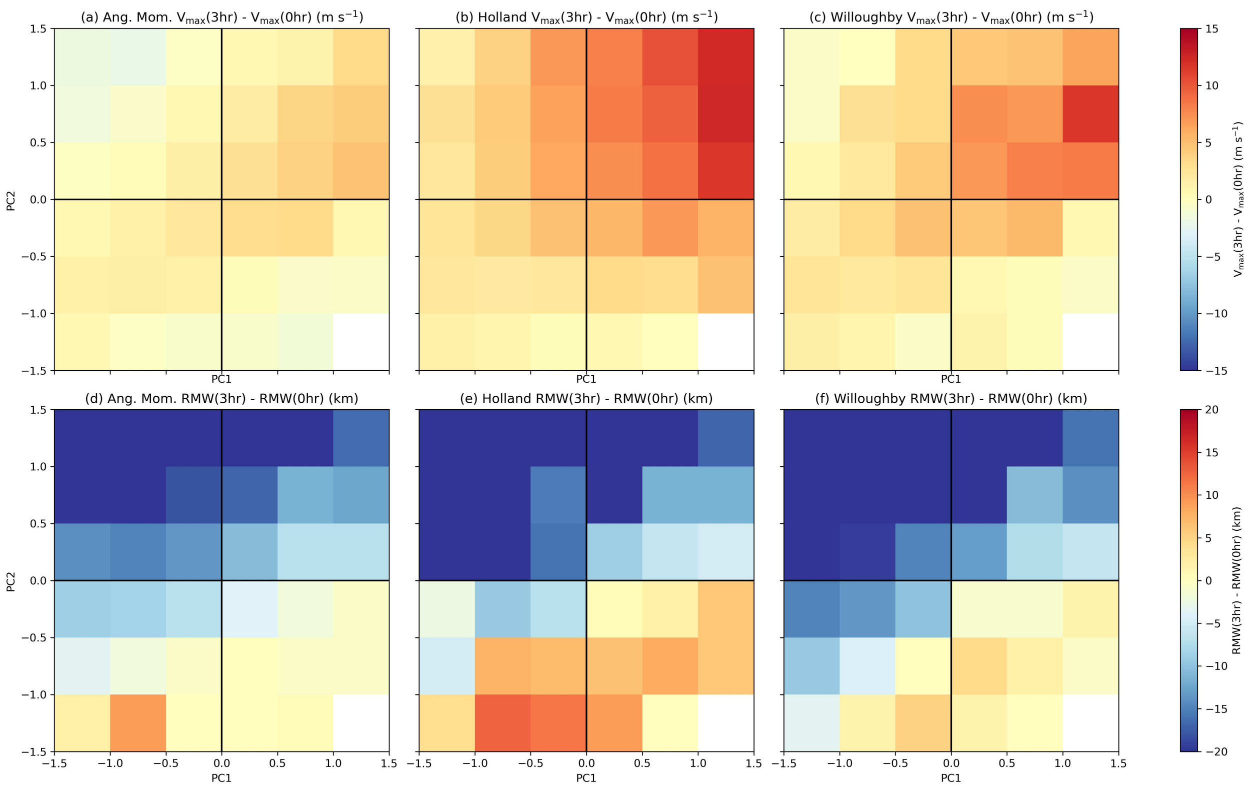

Figure 4.4: As in 4.2, but for the differences between (a-c) the V_{max} (m s^{-1}) and (d-f) the RMW (km) changed from their initial gradient forcing magnitudes in each slab TCBL simulation.

Fig. 4.5 shows the stretching vorticity term of the vorticity budget with respect to u/I at the location of maximum updraft (RMWW). As introduced in Section 4.1, u/I represents a balance between the radial inflow and inertial stability, such that either stronger inflow or weaker inertial stability increases u/I and allows parcels to travel radially closer to the center, where convective heating can become more efficient. Therefore, a TC with a large u/I ratio and large vorticity generation is expected to be most efficient at intensifying. However, while Kepert (2017) chose the radius of maximum negative vorticity gradient, we chose the RMWW as a proxy since the RMWW was very close and the Willoughby method has the steepest vorticity gradient at the eye.

Focusing on the x-axis first, Fig. 4.5 shows that the weakest TCs (purples and blues) have the largest u/I magnitudes for all three methods, which may indicate a greater inward displacement of the RMWW from the RMW, and therefore more efficient heating. In contrast, the most intense TCs (reds and oranges) have the smallest u/I, and may have less efficient heating. There is also a general pattern that for TCs with the same PC1 intensity, smaller TCs have a smaller u/I.

However, when focusing on the y-axis, the strong, big TCs also produce the most stretching. Interestingly, there is a nonlinear relationship between increasing PC2 size for a given PC1 intensity, such that there is little to no relationship between PC2 size and vorticity stretching for the blues and purples, but there is a mostly direct relationship between PC2 size and vorticity for greens to reds. When combined with the u/I patterns, this suggests that there may be a "Goldilocks structure" where there is optimal heating efficiency and vorticity stretching.

However, when also considering radial vorticity advection at the same RMWW location, many of the strong, big TCs also have a more negative advection term, such that the vorticity generation is partially offset locally (Fig. 4.6). In contrast, simulations that did not have large stretching also did not have a large advective term, such that the sum remained relatively unchanged.

4.3.2 Height-Resolved TCBL Model Results

While slab TCBL models are easiest to interpret, they are not capable of fully representing TCBL structure, such as the decrease in TCBL height with decreasing radius. Therefore, the Angular Momentum profiles were re-run in a height-resolved TCBL model to confirm whether the slab TCBL models were representative of a more complete TCBL response to a gradient wind forcing.

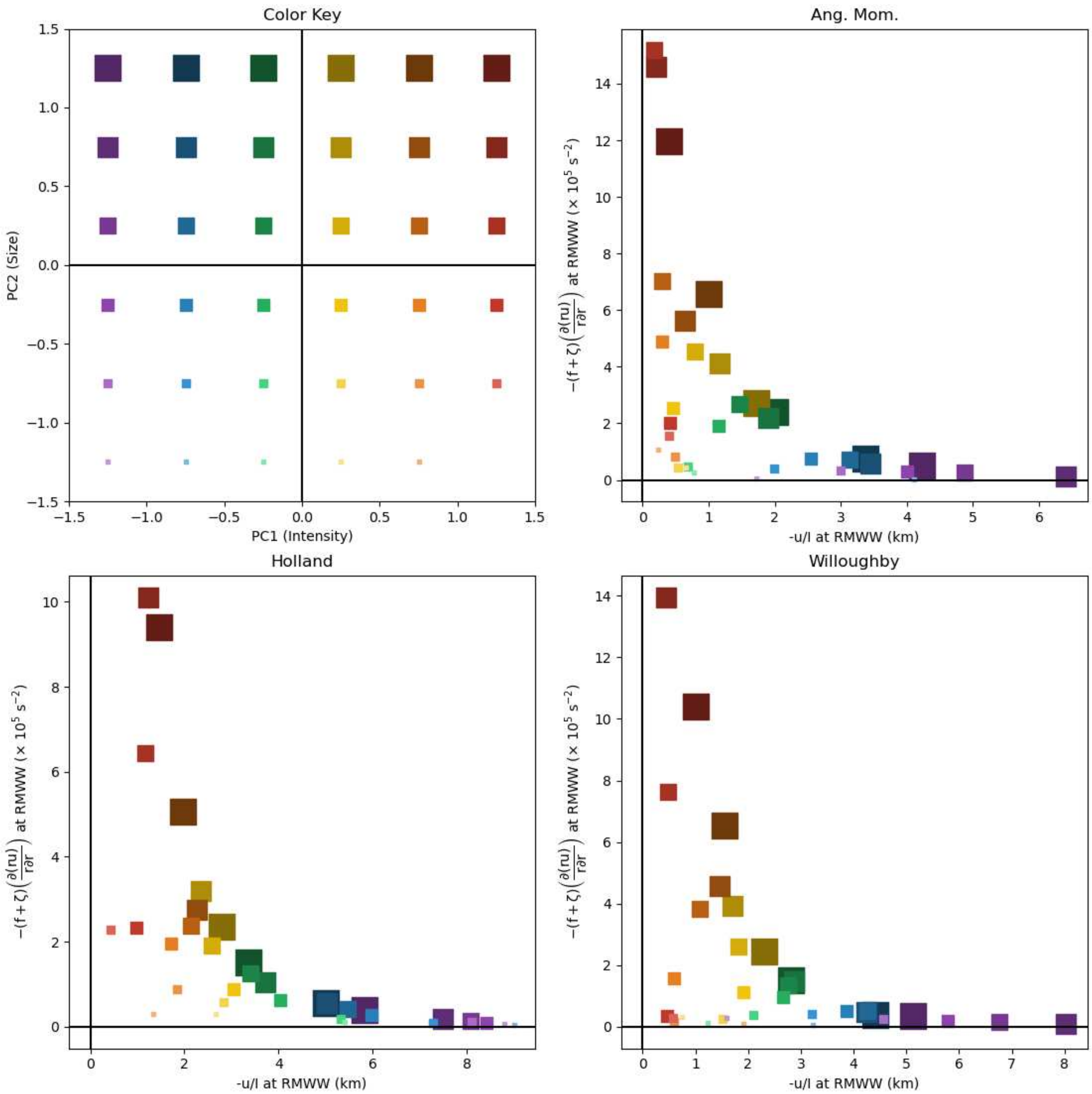

Figure 4.5: Stretching of Vorticity in each slab TCBL model simulation. Scatter point hue goes from cool to warm to indicate weak to strong PC1, and point size indicates PC2 size.

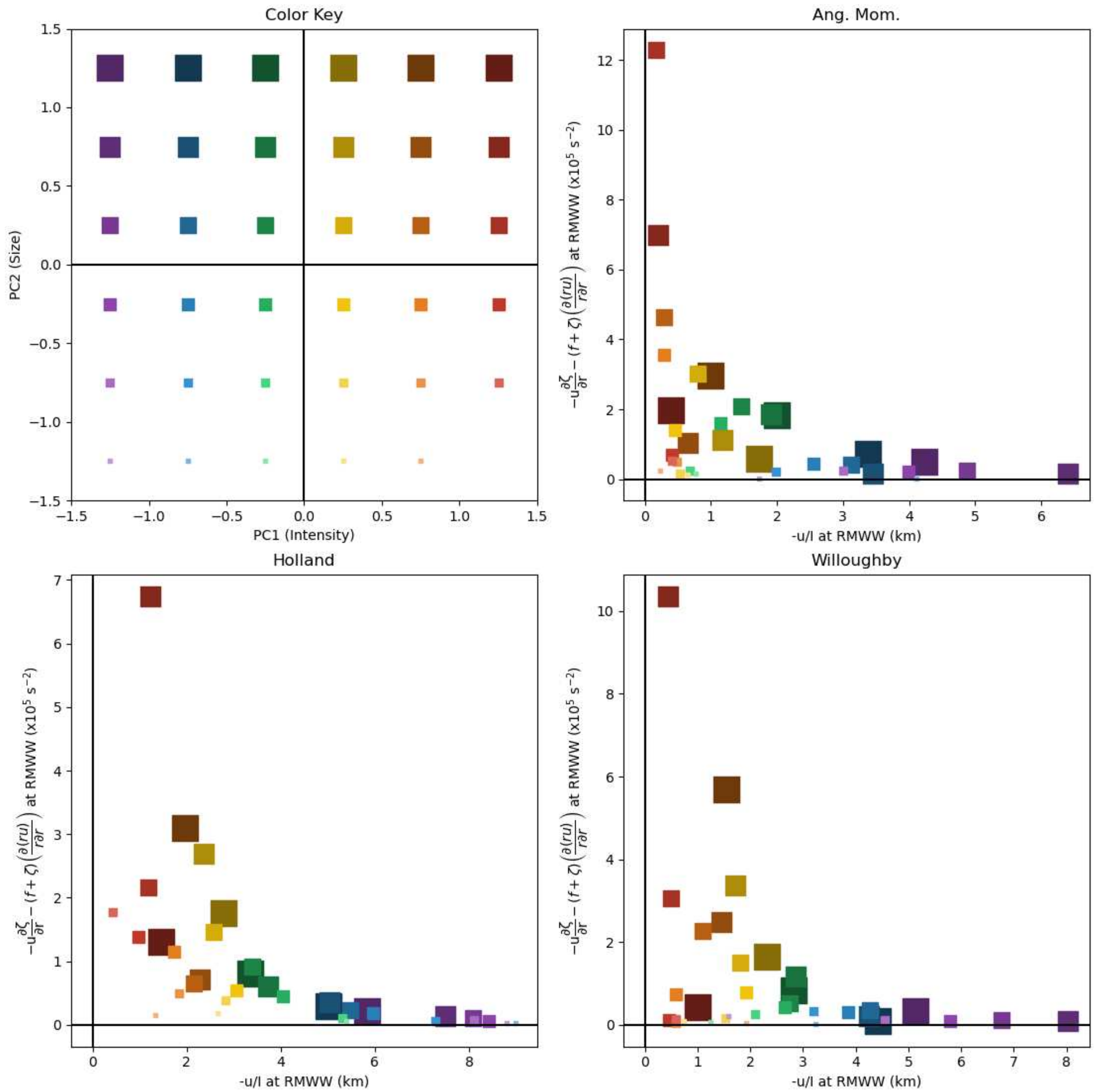

Figure 4.6: Sum of radial advection and stretching of Vorticity in each slab TCBL simulation.

Consistent with the slab TCBL model results, height-resolved TCBL model also shows that the strong, big TCs also have the strongest secondary circulation, while the weak, small TCs have the weakest secondary circulation (Fig. 4.7). Similarly, the weak, big TC has the largest distance between the RMWW and RMWW, and the strong, small TC has the smallest distance between the two. Interestingly, the updrafts are asymmetric in terms of width, such that the portion of the updraft that is radially outward of the RMWW is wider than the portion radially inward from the RMWW.

Interestingly, while Williams Jr. (2015) suggests that the strong, small TCs should have the largest distance between the RMWU and the RMW, our results do not indicate that. Instead, the radius of U_{min} is very close to the RMW, and may be a result of the sharp peak of gradient wind forcing at V_{max}. The height of U_{min} also appears to have a relationship with both intensity and size, such that U_{min} occurs at a higher altitude for weaker and larger TCs. However, the total depth of the inflow layer only appears to vary with TC size, such that larger TCs have a deeper inflow layer.

The height of V_{max} appears to have a relationship such that larger TCs have a higher V_{max}, but stronger TCs have a lower V_{max}, such that the weak, big TCs have the highest V_{max} altitude, and the strong, small TCs have the lowest V_{max} altitude. In addition, the strong, small TCs also have the most peaked tangential wind outside the tangential wind, consistent with the high angles of ϕ in that part of the phase space.

The full suite of height-resolved TCBL model simulations, shows that the patterns observed in Fig. 4.7 are consistent and smoothly vary across the phase space (Fig. 4.8). In addition, Fig. 4.8 shows broadly similar results to the slab TCBL model results in Fig. 4.2-4.3a,d,g, except that the maximum wind speeds are slightly weaker for all wind components due to the vertical advection possible with resolving height.

Additionally, while V_{max} is slightly weaker, its RMW tends to be located slightly more radially outward than in slab TCBL model. However, the RMWW tends to be relatively more radially inward from the RMW, but the difference is on the order of 5 km. In contrast, the RMWU tends

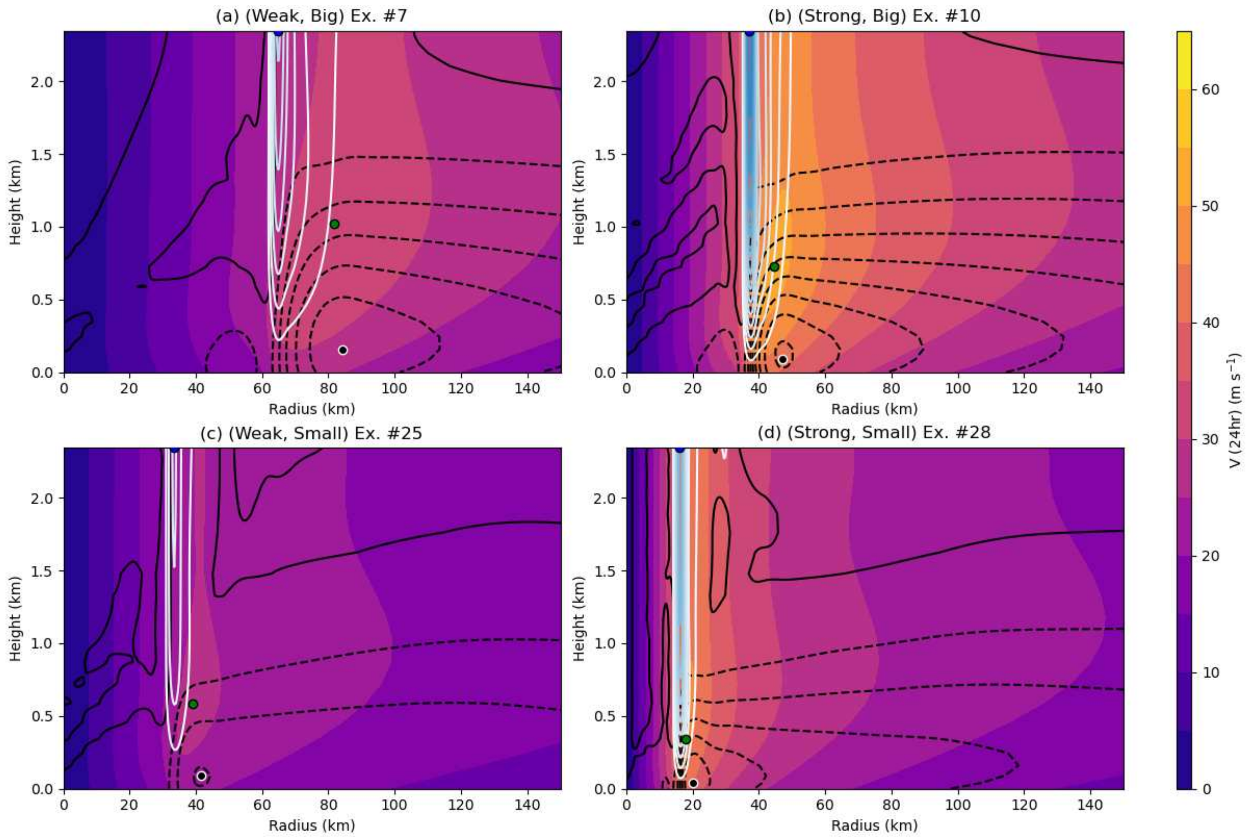

Figure 4.7: Quasi-steady TCBL response after 24 hr for the four example bins, where the contour intervals for each variable are ever:y 5 m s^{-1} for V (shading), every 2 m s^{-1} for U (black contours), and every 0.25 m s^{-1} for W (white to blue contours).

to be much closer to the RMW in height-resolved TCBL model, with the exceptions of the two weakest and smallest bins (No. 30-31). The small difference between RMW and RMWU may be due to the sharp point at V_{max}, and bins 30–31 may be forming a secondary wind maxima.

Fig 4.9 shows the changes from initial gradient wind forcing to the quasi-steady TCBL response after 24 hr, and shows that the changes in magnitude for V_{max} and RMW are much less dramatic than in slab TCBL model (Fig. 4.4a,d). However, the general pattern is still consistent that the strong, big TCs have the largest increase in V_{max} and therefore the largest supergradient winds. Similarly, the weak, big TCs also still have the largest decrease in RMW. Interestingly, the differences between the weak, big and strong, big quadrants are much less pronounced in height-resolved TCBL model where height is resolved than in slab TCBL model. Another interesting result of Fig 4.9 is that the TCBL response appears to be less conducive for intensification, due to the slight broadening of the RMW in the steady-state TCBL response, and the most intense Bin 34 shows a slight weakening from the gradient wind forcing.

Overall, results from height-resolved TCBL model indicate that the TCBL structure may be most favorable for future intensification in strong, big TCs, due to having the strongest secondary circulation. Strong inflow is present to converge angular momentum and increase sensible and latent heat fluxes. Additionally, the frictional updraft is the strongest and located relatively far inward from V_{max}, which is conducive for more efficient conversion from heat to kinetic energy.

Similarly, height-resolved TCBL model results also indicate that the weak, big TCs are most likely to contract in terms of RMW, due to having a moderately strong radial inflow and furthest radially inward updraft location. However, the updraft magnitude is not as strong, which may not be as favorable for intensification.

Interestingly, while the strong, small TCs have a strong updraft, the radial inflow is not as strong as in TCs with the same PC1-Intensity but larger PC2. This may indicate that strong, small TCs are less likely to undergo RMW contraction, and not change in size as much.

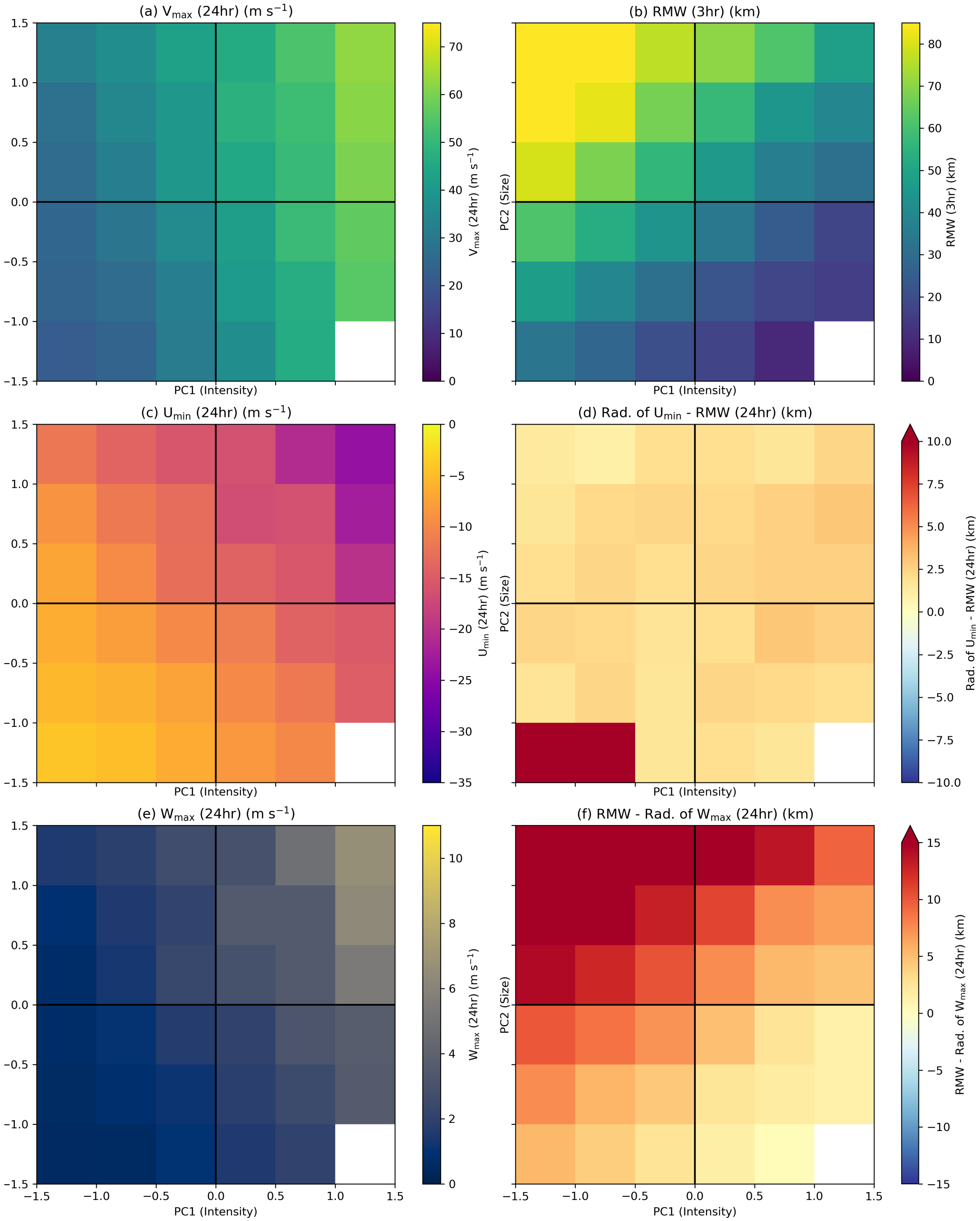

Figure 4.8: As in Figs. 4.2a,d,g–4.3a,d,g, but for the height-resolved TCBL model simulations at 24 hr. Note that the colorbar range was reduced in (d) when compared to Fig. 4.3.

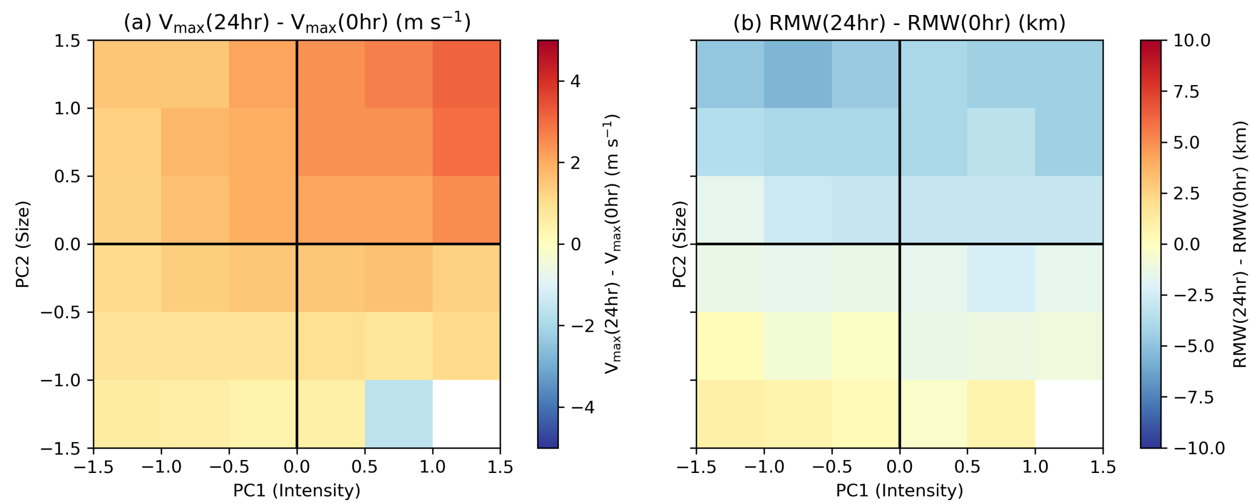

Figure 4.9: Changes in V_{max} (m s^{-1}) and RMW (km) from 0 to 24 hr, as in Fig. 4.4a,d.

4.4 Discussion and Conclusion

In this chapter, we sought to determine what the dynamical implications of the profiles from Ch. 3 were, and whether the analytic method for idealized profile construction or the EOF phase space location had a bigger impact on TCBL responses to gradient wind forcing. For this, a new slab TCBL model was used, and results indicate that while there were systematic differences between the methods on how the TCBL adjusted to gradient wind forcing, the general location in the EOF phase space was more important for TCBL responses than the details of the analytic profile. For example, we systematically saw that the strongest, largest TCs induced the strongest secondary circulation, regardless of which profile was used. We also saw that the weakest, largest TCs systematically also had the largest contraction of the RMW.

We then sought to begin laying a foundation for whether certain regions of the EOF phase space are more conducive for intensification based on the TCBL response to gradient wind forcing. Slab boundary layer model results indicated that weak TCs ($PC1 \leq -0.5$) regardless of size may be more favorable for heating efficiency and contraction given their high u/I values. However, these TCs produced little vorticity stretching within the TCBL. In contrast, the strong, big TCs produced large vorticity stretching, which could be favorable for intensification. However, the addition of the radial advection term decreased the net vorticity generation the most in the strong, big TCs. Combined with the lower u/I values, the strong, big TCs may not be as efficient for intensification. Overall, results suggest that there may be a "Goldilocks zone" where average TCs may have an optimal balance between u/I and vorticity stretching, and the possibility of this zone was then investigated in a height-resolved TCBL model.

In the height-resolved TCBL model, we saw that results were qualitatively consistent with the slab TCBL model. We again saw that the strongest, largest TCs produced the strongest secondary circulation, such that the stronger radial inflow and updraft speeds allow a TC to better converge angular momentum and increase surface thermodynamic fluxes that can further aide in intensification when moist convection is present.

Additionally, we saw that the weakest, largest TCs had the largest inward displacement of the maximum updraft location, which is more conducive for the contraction of the RMW. Addtionally, the weak, large TCs had a stronger secondary circulation than weak, small TCs, which may be favorable for intensification, but the secondary circulation was not as strong as in intense TCs. Small TCs had a relatively weaker secondary circulation, as well as smaller changes in RMW as the boundary layers adjusted to gradient wind forcing.

All together, we saw qualitatively similar results between the slab and height-resolved boundary layer models, but the height resolved TCBLs tended to have slightly larger RMWs and weaker V_{max}. Additionally, the height-resolved TCBLs experienced much smaller changes in response to a constant gradient forcing. In Ch. 5, we will investigate the two-way interaction between axisymmetric TCBLs and the overlying TCs.

Chapter 5

Relationships between Tropical Cyclone Wind Structure and Intensification

5.1 Introduction

Rapid intensification (RI) is associated with the largest forecast errors, due in part to their dependence on internal processes that are not fully understood (Trabing and Bell 2020). In particular, the onset RI is especially difficult to forecast (DeMaria et al. 2021), and better characterising the TC intensity, size, and structure could potentially lead to earlier recognition that RI onset may have recently occurred in a TC.

While relationships between RI and TC intensity and size are not well understood, previous studies have shown that: strong TCs typically undergo RI at least once in their lifetimes (Kaplan and DeMaria 2003); they have longer lifetimes, during which they grow from smaller than to larger than non-RI TCs (Fudeyasu et al. 2018); and that greater axisymmetry is favorable for RI (Miyamoto and Takemi 2015). Together, these studies suggest that strong TCs are more likely to undergo RI. Additionally, TCs with larger Rossby numbers are associated with earlier RI onset (Miyamoto and Takemi 2015), and shallow water models indicate that smaller TCs may be able to intensify faster and to stronger intensities (Hendricks et al. 2014). However, an open question remains as to how RI characteristics vary as a function of both intensity and size simultaneously.

While the maximum intensity and maximum size of a TC have a weak correlation in observations (Merrill 1984), recent research has revealed that there are complex relationships between the two attributes over time, even in identical, favorable environments for intensification. In particular, the initial characterization of intensity and size appears to be important at all future times. For example, in idealized, axisymmetric TCs, Tao et al. (2020) shows that even in environments that yield TCs with the same maximum potential intensity (MPI), initially larger TCs end up having higher steady-state intensities than initially smaller TCs at the same initial intensity. In more realistic 3D simulations, Tao et al. (2022) shows that the forecast error in an ensemble of Hurricane Patricia (2015) simulations is strongly related to the initial structure and intensity, such that a more accurate initial structure yields a more accurate intensity forecast at all times.

Initial conditions of TC intensity and size also matter for future TC size, as well. For example, Tao et al. (2020) also shows in the ensemble of axisymmetric simulations that initially larger TCs remain larger at all times. In fact, not only do initially larger TCs remain larger at all times, Martinez et al. (2020) show that the difference in size between initially large and small TCs actually *increases* over time, even in different environmental humidities in both 2D and 3D idealized simulations. Together, these and additional recent findings suggest that TCs have memory of their initial conditions of intensity and size throughout their lifecycles. Therefore, correctly representing these initial conditions is important for improving future forecasts of intensity, size, and intensification and contraction rates.

Additionally, while initial TC size and intensity are important, there are also many different ways that *current* intensity and size may influence future TC intensity and size. For example, in real environments, vortex size is associated with vortex "resiliency," such that large TCs appear to be more resistant to the negative effects of vertical wind shear than smaller TCs and are therefore better able to maintain their intensities over time (Reasor et al. 2004). In addition, TCs with a broadening outer wind field, which are therefore increasing in size, are associated with secondary eyewall formation (Rozoff et al. 2012), and the subsequent eyewall replacement cycles are associated with intensity and size changes near V_{max}. Finally, small TCs may also be associated with faster intensification rates, and examples of very small TCs that support this hypothesis include Hurricane Charley (2004), which was introduced in Ch. 2, and Hurricane Patricia (2015), which currently holds the record for fastest change in intensity over 24 hours (Rogers et al. 2017).

However, while there are many more ways that intensity and size influence TCs, a central focus of this study regards the effects of intensity and size on the change in RMW throughout the period of TC intensification. Current TC intensity is associated with future contraction rates, such that weaker TCs appear to contract more than stronger TCs in observations (Stern et al. 2015). This relationship may be indirect since Stern et al. (2015) also show that the contraction of the RMW must satisfy the condition

$$\frac{\partial RMW}{\partial t} = -\frac{(\partial/\partial r)(\partial V/\partial t)}{(\partial^2 V/\partial r^2)}\bigg|_{RMW}, \tag{5.1}$$

where the contraction rate of the RMW depends on the radial gradient of the tangential wind tendency over the curvature or "peakedness" of the tangential wind at the RMW at a given point in time. In other words, the RMW depends in part on the angle of ϕ (Eq. 2.1), and lower angles of ϕ appear to be more favorable for RMW contraction at a single point in time. However, this condition does not inform how the RMW contracts over the entire TC lifecycle, and Stern et al. (2015) acknowledge that "[it] is unclear how typical it is for the RMW to reach a steady state prior to peak intensity, as opposed to following the existing paradigm, where peak intensity is coincident with the end of contraction."

However, while Eq. 5.1 does not explain the dynamics of how and why the RMW contracts, other research has shown that effects from the TCBL play a large role in setting the location of the RMW. In particular, the location of the maximum updraft with respect to the vorticity gradient is important. If the updraft is located on a steep vorticity gradient near the RMW, then the significant vorticity stretching that is produced will act to amplify the existing tangential wind and further spin up the storm (Kepert 2017). However, if the vorticity stretching produced in the updraft is located sufficiently far inward from the RMW, then the tangential wind will be spun up radially inward from V_{max}, and the RMW will contract.

Since there are many complexities and interactions that stem from differences in initial and current TC intensity and size, we first seek to clarify the relative contributions from each aspect on future TC intensity and size. Additionally, we also seek to examine how the contraction of the RMW is dependant on intensity and size and how its relationship to intensification rates evolves during TC intensification, with a special emphasis on rapid intensification.

5.2 Experimental Design

In this study, we increase complexity and realism from the slab and height-resolved TCBL models of Ch. 4 by introducing an additional set of numerical simulations in which we allow the TCBL to be coupled with the overlying vortex in the axisymmetric mode of Cloud Model 1 (CM1; Bryan and Fritsch 2002).

As in height-resolved TCBL model, we use all 35 Angular Momentum profiles developed in Ch. 3. CM1 uses the same Angular Momentum profiles as height-resolved TCBL model with the same 1 km radial grid spacing, but the domain extends much further radially outward. In addition, the axisymmetric version of CM1 retains the 1km grid spacing, and has 59 vertical grid levels.

Rather than a linear decay with height from the surface to 15 km as is the default setup, CM1 has been modified to have a constant initial vortex from 0−3.5 km, and then a linear decay to 15 km to improve the wind-pressure relationship such that P_{min} was lower and more consistent with the bin-average profiles. However, while Angular Momentum profiles are optimized for several of the original EOF parameters, there are still some departures from the bin means (Fig. 5.1). In particular, pressure is adjusted by CM1, and profiles may depart from the bin-average P_{min} by as much as 40 hPa for the strong, big TCs. However, while P_{min} skews to be initially too weak for those storms, they also tend to have larger ϕ angles that skew them towards being more intense. This departure in ϕ angles is consistent with the RMSE discussed in Ch. 3, and is because the method fits between the RMW and R_{34}, not between 1–2RMW.

5.3 Results

Fig. 5.2 shows the developing TCBL structure just after model spinup, which is defined as the first 5 hr of each simulation in this study. Fig. 5.2b-d is also at the onset of rapid intensification (hereafter RI Onset), which is defined as the operational definition of an increase in V_{max} of 30

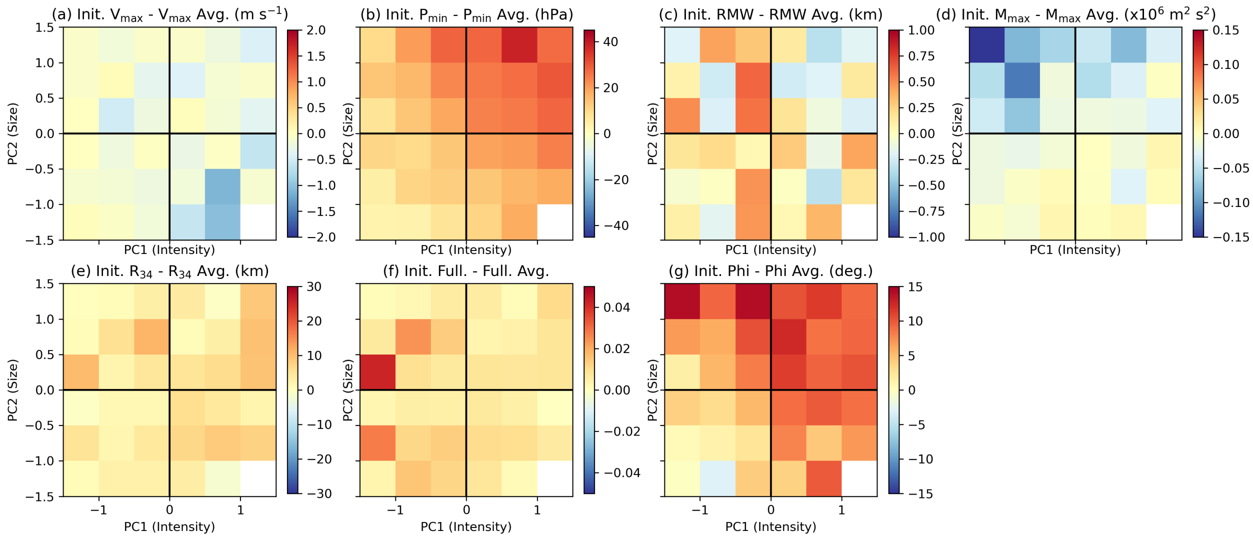

Figure 5.1: Initial CM1 vortex departure from the average within each bin shown in Fig. 3.2 for each of the seven EOF parameters.

kt within 24 hr. Fig. 5.2a is 5 hr prior to RI Onset. The CM1 TCBL structure is much noisier than the steady-state TCBL structure in Fig. 4.7, but the general structure has similarities. First, in the weak examples at this time, the maximum updraft lies just radially inward of V_{max}. Second, in the strong examples at this time, U_{min} and V_{max} are nearly vertically aligned, with an updraft bottom nearly reaching to the location of U_{min}. Finally, the radial inflow within the TCBL and radial outflow above it is strongest in the strong, big example, and weakest in the weak, small example.

However, there are differences between the height-resolved TCBL model structure and the CM1 structure at this time as well. First, the maximum updraft does not necessarily occur within the RMW, since isolated convection may have stronger updrafts at this time (Fig. 5.2d). Second, the radial outflow above the TCBL also appears to be slightly stronger.

Fig. 5.3 shows the evolution of the seven EOF parameters over the first 72 hr, and several patterns emerge. First, the initial model spinup is more pronounced for the strongest initial vortices, but a similar duration for all simulations. Interestingly, V_{max} ends the initial weakening slightly earlier than the initial R_{34} contraction during this model spinup period. After the model spinup period, Fig. 5.3a shows that the most initially intense simulations appear to have

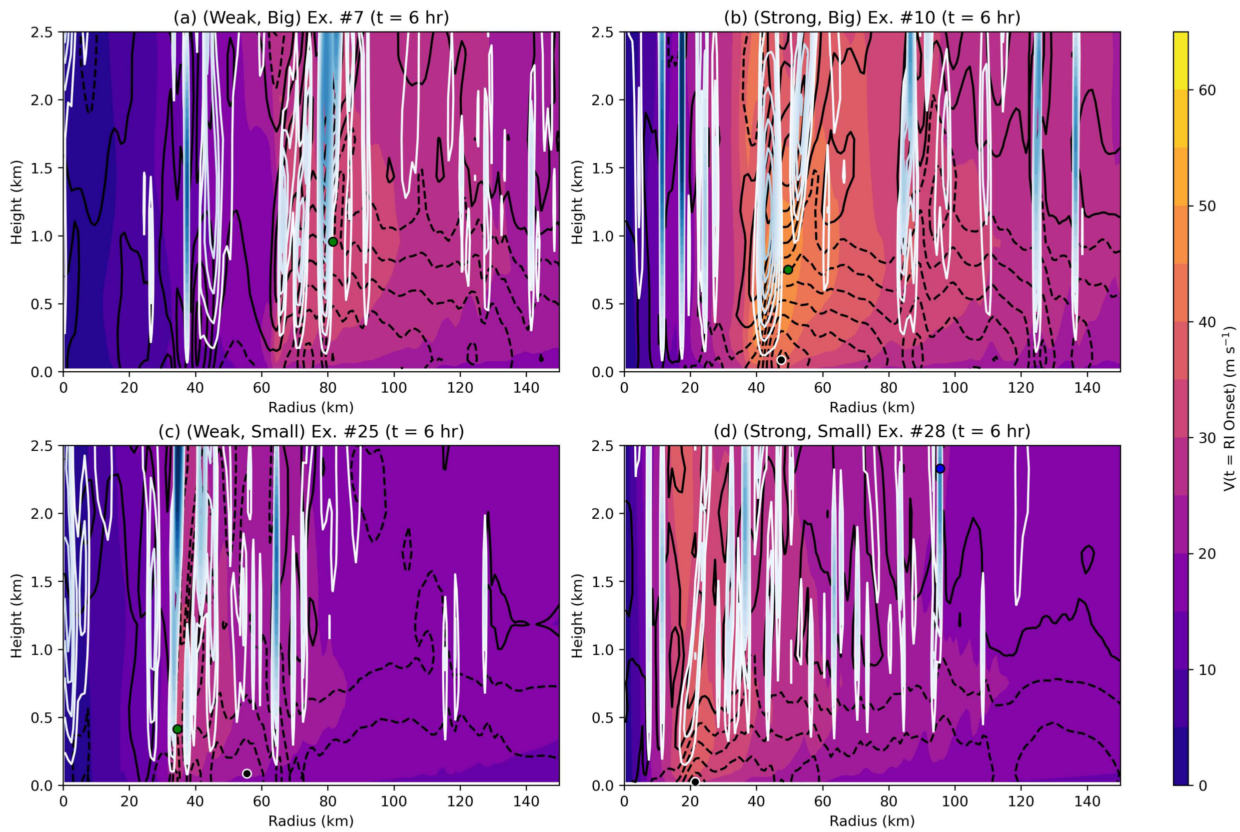

Figure 5.2: As in Fig. 4.7, but for CM1 simulations at $t = 6$ hr.

the fastest intensification rates, but for the shortest period of time. Similarly, the initially weakest simulations in purple take longest to reach rapid intensification rates, and the peak rates do not appear to be as rapid as the initially strongest simulations.

5.3b shows P_{min}, which generally shows the same patterns as V_{max}. However, since the pressure field is computed by CM1, there is not enough initial spread in values, and simulations with the same initial PC1-Intensity have the same initial P_{min} regardless of size.

Interestingly, there are nonlinear relationships between RMW and intensification rates (Fig. 5.3c). For the initially weakest TCs in purples and blues regardless of size, the RMW initially remains a nearly steady size until shortly after V_{max} starts to accelerate, when it starts to sharply contract. However, as TCs are initialized more intense in greens and warmer colors, there is less of a relationship between RMW and V_{max}. Rather, the RMW immediately contracts for the initially larger TCs or immediately starts to slowly expand for the smallest TCs. Overall, the spread of RMW values becomes nearly steady after $t = 40$ hr, and Fig. 5.3c shows that the initially largest RMWs generally remain the largest throughout their lifecycles.

M_{max} shows broadly similar trends to RMW, where the initially largest simulations generally still have the largest M_{max} by 72 hr (Fig. 5.3d). Interestingly R_{34} exhibits very different evolutions from RMW, where there is a sharp decrease in R_{34} during model spinup, but a slow expansion with time after model spinup (Fig. 5.3e). There is also not a large difference in rates of expansion across all simulations either.

Fullness also appears to have a broadly similar pattern to RMW, where the initially weak TCs regardless of size have a nearly steady period of fullness until shortly after model spinup until a rapid increase at approximately 20 hr, and the initially strong TCs remain at high fullness values (Fig. 5.3f).

While phi shows the largest noise, there is a general increase with time throughout the entire 72 hr shown (Fig. 5.3g). Since phi is most closely aligned with PC3 and roughly describes TC maturity, the general increase in phi indicates that while V_{max} may be steady after $t = 40$ hr for the majority of simulations, the simulations are still becoming more mature and Rankine-like.

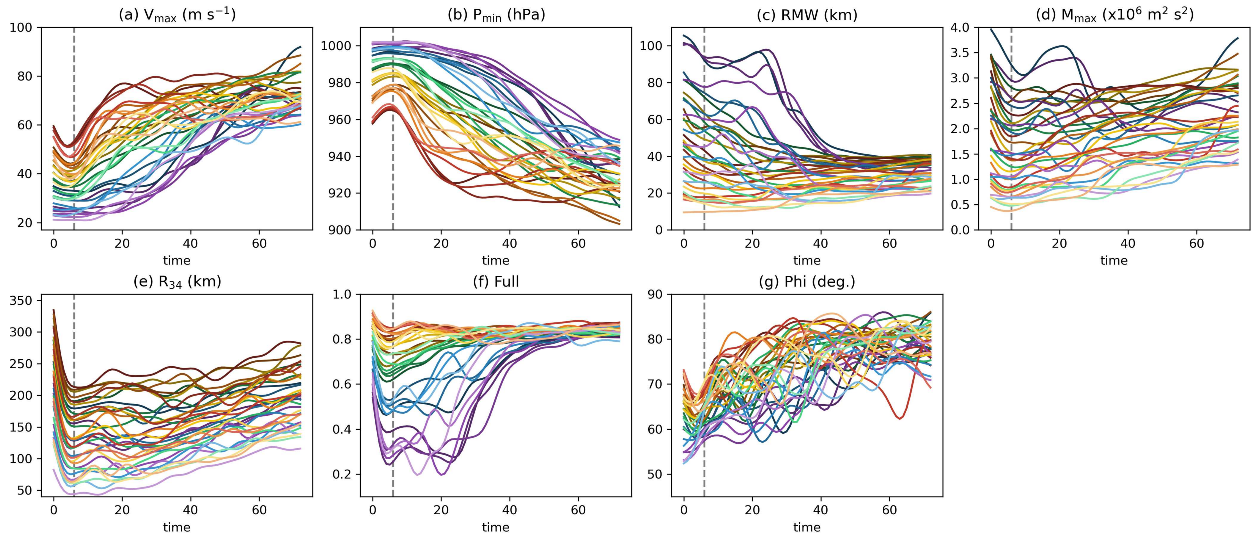

Figure 5.3: All CM1 time series of EOF parameters from 0–72 hr. Colors are consistent with the color key in Fig. 4.5–4.6, where hues from purple to red represent negative to positive PC1-Intensity, and shades from light to dark represent negative to positive PC2-Size. A gray, dashed line at $t = 6$ hr denotes the end of the model spinup period.

Fig. 5.4 shows the time series of V_{max} relative to RI Onset and stratified by PC1-Intensity and PC2-Size quadrants. The slope of each curve represents the instantaneous intensification rate, and results show that the strong TCs regardless of size have quite high intensification rates within the first 12 hours after RI onset. In particular, the strong, small TCs seem to have the fastest RI, both in terms of instantaneous intensification rate and when the TCs reach their maximum potential intensities. Interestingly, the larger TCs also achieve a higher steady-state, consistent with Tao et al. (2020).

However, while the strong TCs have the fastest intensification rates, they have much more modest contraction rates (Fig. 5.5). Instead, the weak, big TCs have the fastest instantaneous contraction rates, followed by the weak, small. There is also a dependence on TC size, with larger TCs contracting more than their smaller TCs at similar intensities.

Fig. 5.6 shows the intensification rates stratified by either the initial quadrant the simulation started in (Fig. 5.6a), or the location of the instantaneous intensification rate (Fig. 5.6b). Results show that while there is a slight dependence of the fastest intensification rates such that the

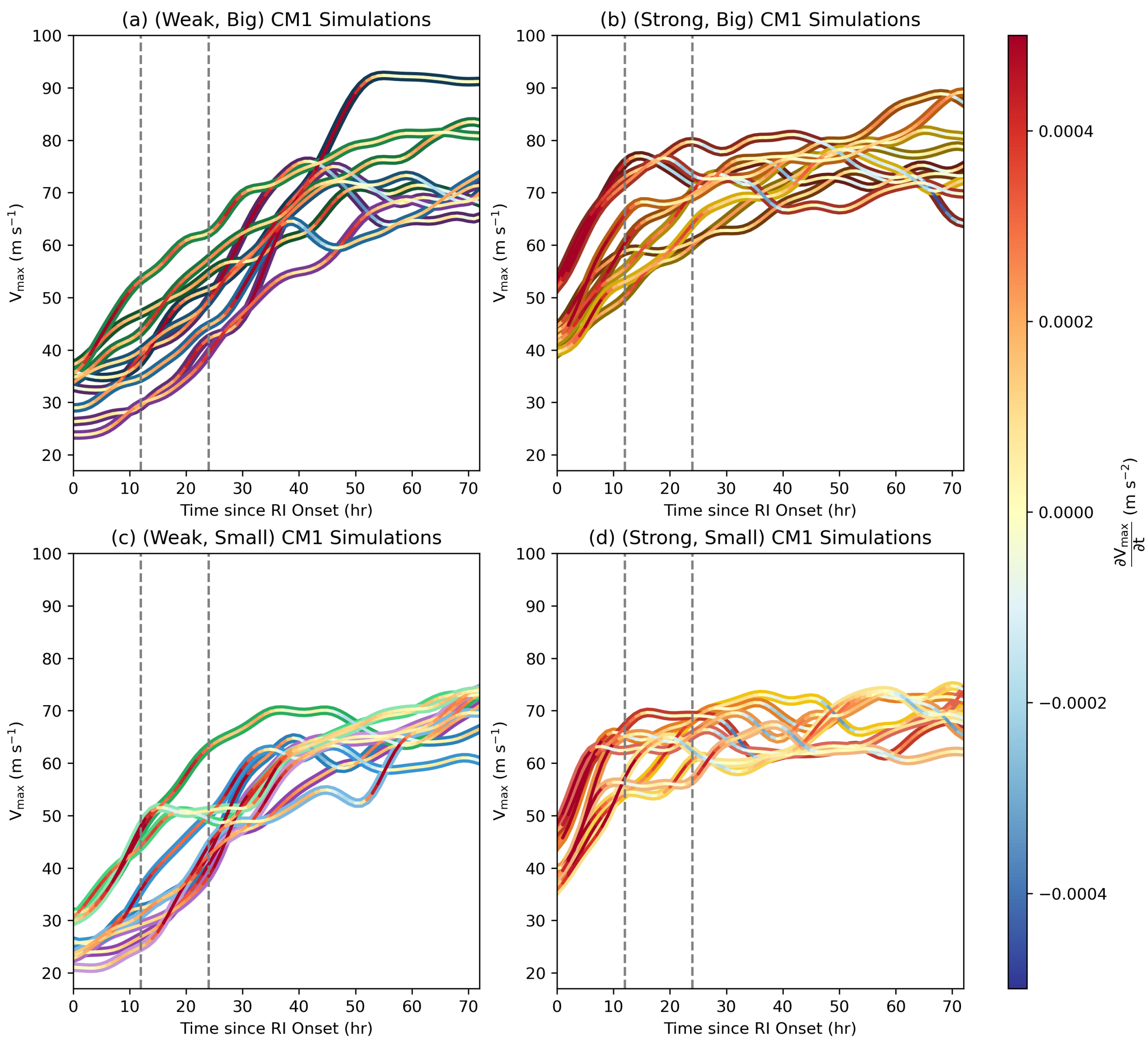

Figure 5.4: All CM1 time series of V_{max} from 0–72 hr after RI Onset in m s^{-1}. Colored outlines are consistent with the color key in Fig. 4.5–4.6, and shading represents the slope or instantaneous intensification rate (m s^{-2}). Gray, dashed vertical lines denote $t = 12, 24$ hr after RI Onset for reference.

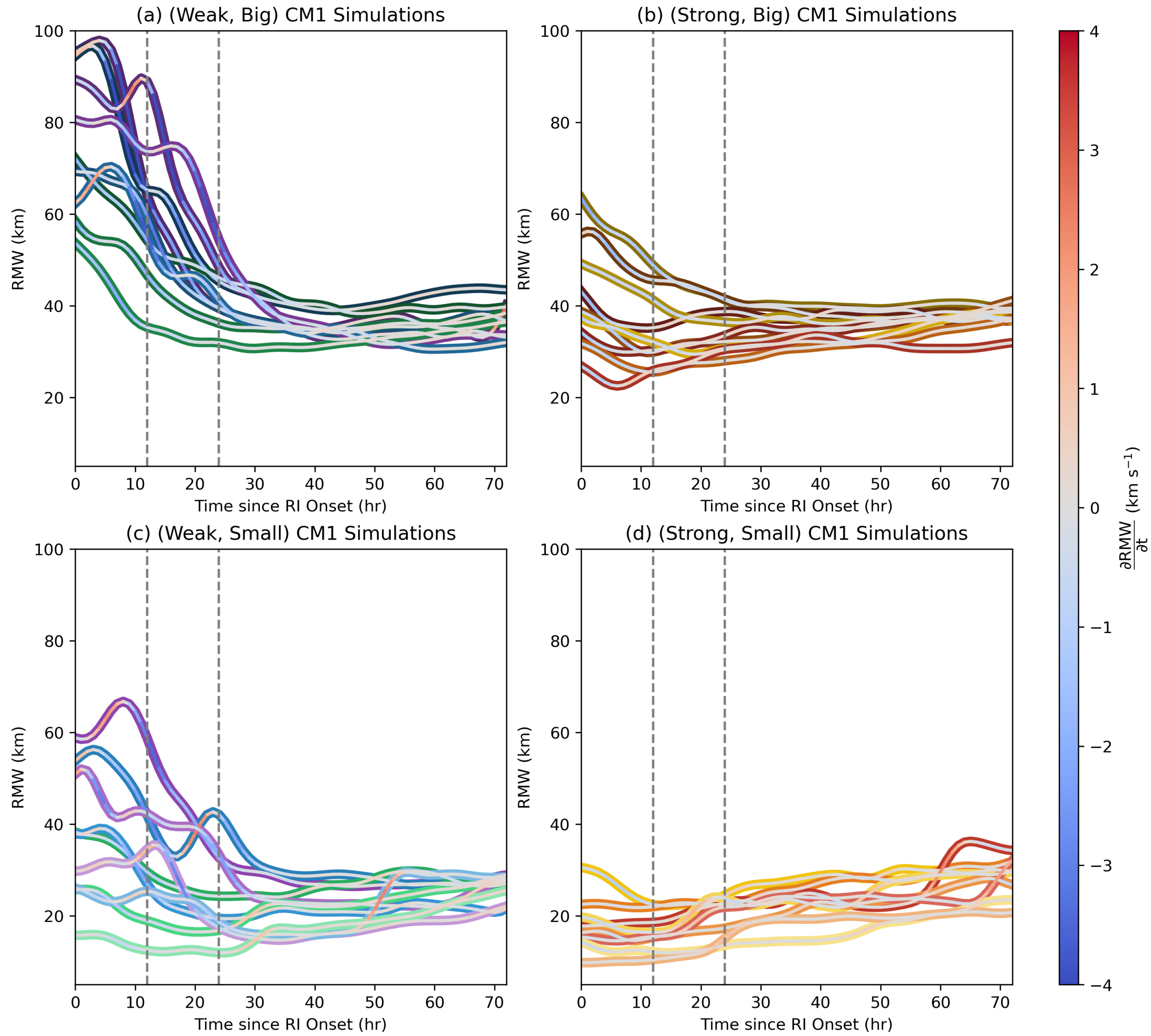

Figure 5.5: As in Fig. 5.4, but for all CM1 time series of RMW from 0–72 hr after RI Onset. Shading also denotes slope, but now represents instantaneous contraction rate in km s^{-1}.

initially strong, small TCs have a larger tail in the fastest intensification rates, there is a much clearer difference in rates between the quadrants based on the current quadrant.

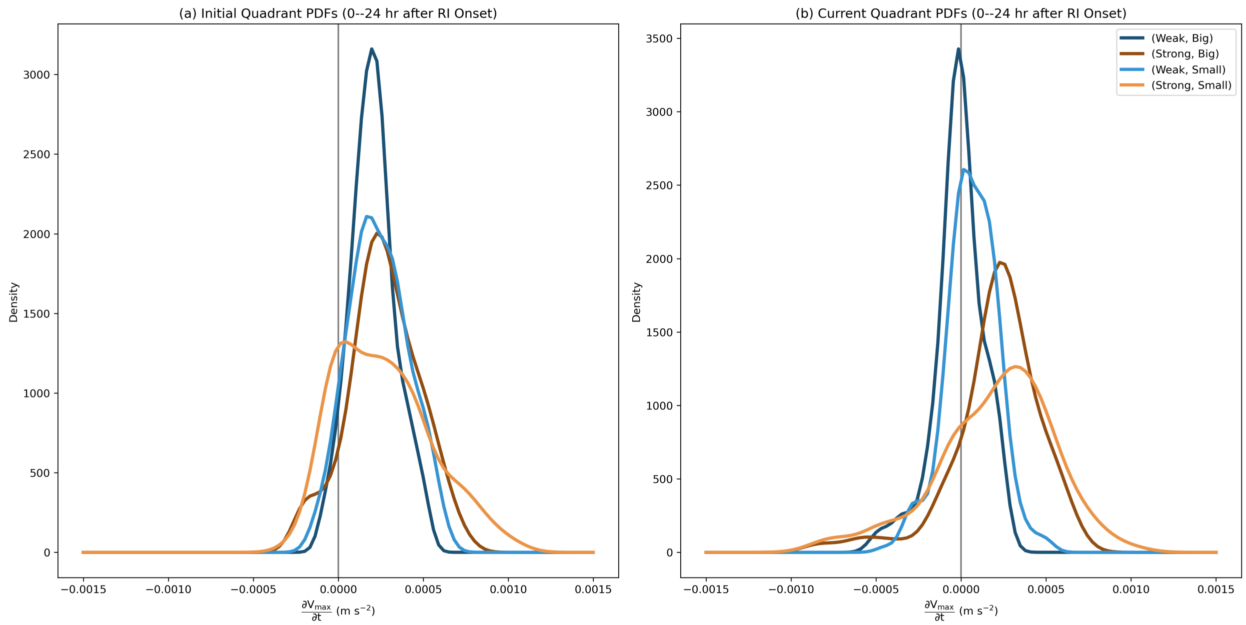

Figure 5.6: Probability density functions of instantaneous intensification rates 0–24hr after RI Onset, but stratified by (a) quadrant location in which each simulation was initialized and (b) current quadrant location at each time.

However, the opposite pattern is true for contraction rates (Fig. 5.7). Instead, instantaneous contraction rates appear to depend more strongly on the initial size rather than the current size, since the PDFs have a pronounced negative skew in Fig. 5.7a and are nearly overlapping in Fig. 5.7b. Additionally, the weak, big TCs have the most negative skew of contraction rates, indicating that they contract the most. In contrast, the small, strong TCs have a quite large peak near zero, indicating that they do not change size much at all.

Fig. 5.6-Fig. 5.7 together suggest that there is a short-lived relationship between intensification rates and contraction rates such that fast contraction decreases intensification rates; however, there is a very weak correlation on instantaneous time scales across all simulations from 0–24 hr after RI Onset.

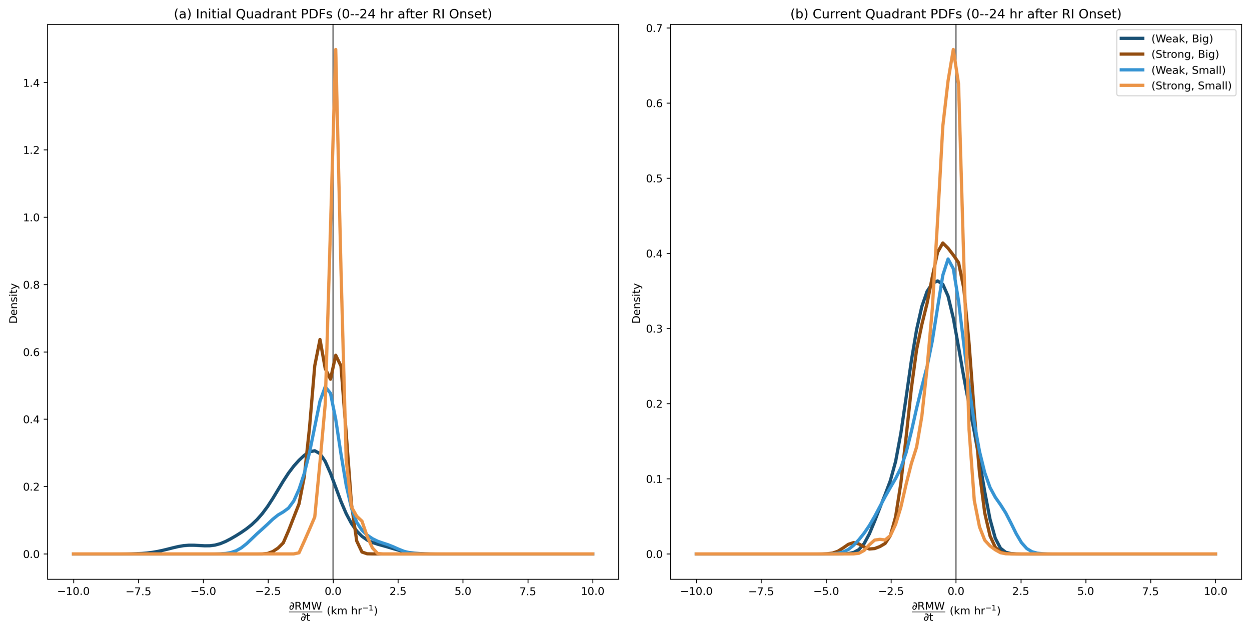

Figure 5.7: As in Fig. 5.6, but for contraction rates 0–24hr after RI Onset in km hr^{-1}.

Fig. 5.8 shows the shading and time period from 0–24 hr after RI Onset as in Fig. 5.4, but regressed onto the PC1-Intensity and PC2-Size phase space. In this framework, it is much easier to see that the initial PC2-Size strongly constrains the future size, such that the initially big TCs in 5.4a-b remain larger throughout the simulation when compared to the initially smaller TCs. There is also a suggestion that TCs are mostly done with contracting in terms of PC2-Size by about the time they reach a PC1-Intensity of roughly -1, but this could be specific to the experimental design.

When comparing simulations in terms of PC1-Intensity, 5.8 shows that the weaker TCs undergo a larger 24-hr intensity change than the stronger TCs in terms of PC1-Intensity, since their trajectories are longer. However, TCs in the strong, small quadrant clearly have the darkest shading, which indicates the highest intensification rates. Finally, for simulations with an RI Onset at a PC1-Intensity less than -1, simulations generally appear to reach their peak instantaneous intensification rates after surpassing a PC1-Intensity of -1.

Fig. 5.9 shows the same trajectories as in 5.2 but shaded by instantaneous contraction rate. Here, we can very clearly see that that weak, big TCs contract simultaneously in terms of PC2-

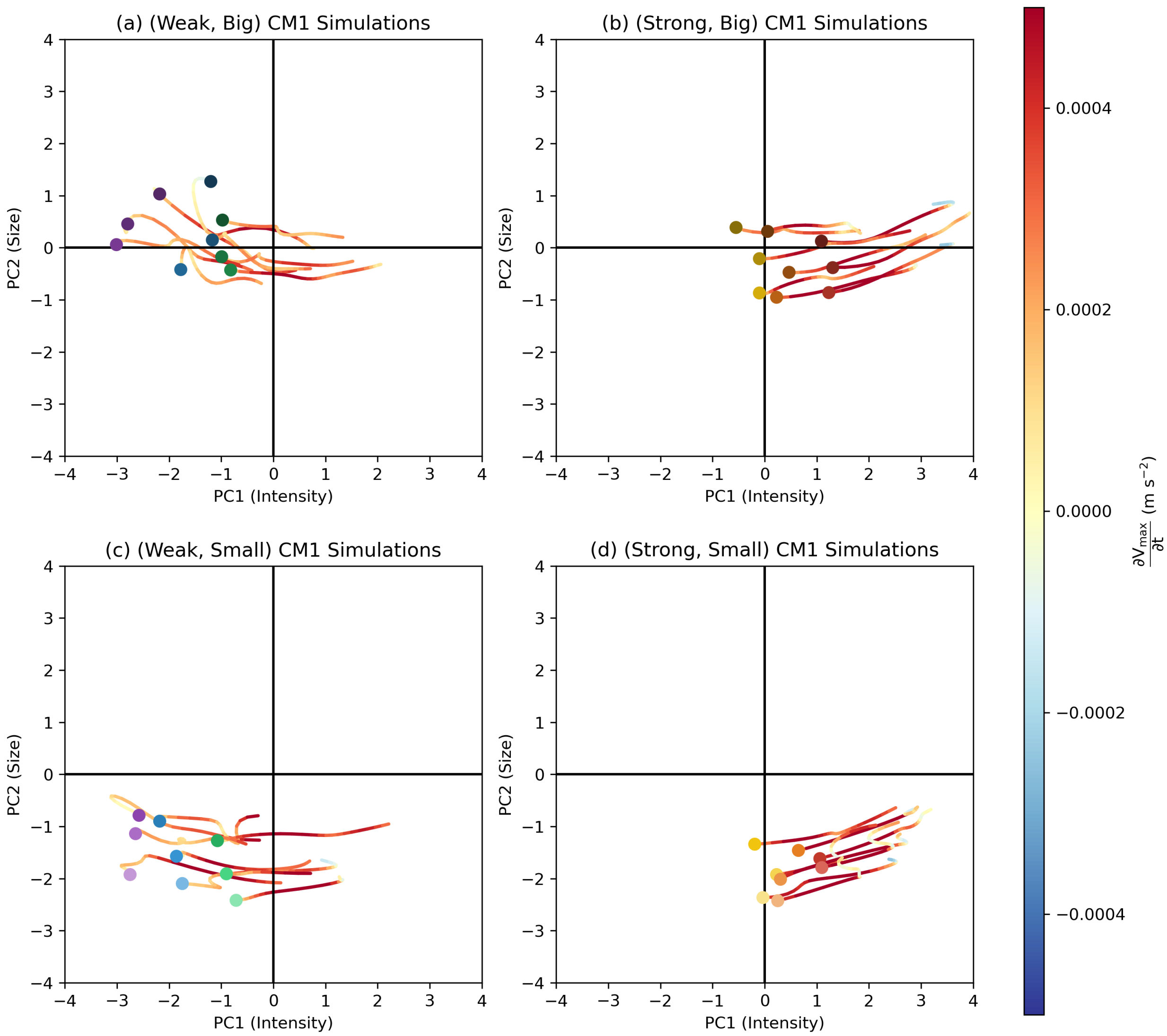

Figure 5.8: All CM1 time series regressed onto PC1-Intensity and PC2-Size for 0–24 hr after RI onset, and shaded by instantaneous intensification rate of V_{max} in m s^{-2}.

Size and RMW. Additionally, we can also see that the RMW contraction accounts for the modest decrease in PC2-Size in the weak, small TCs, but the slight RMW contraction in the strong, big TCs does not result in an appreciable change in PC2-Size. Finally, we can see that there is no appreciable change in RMW for the strong, small TCs, but there is a suggestion of eyewall replacement cycles after PC1-Intensity increases.

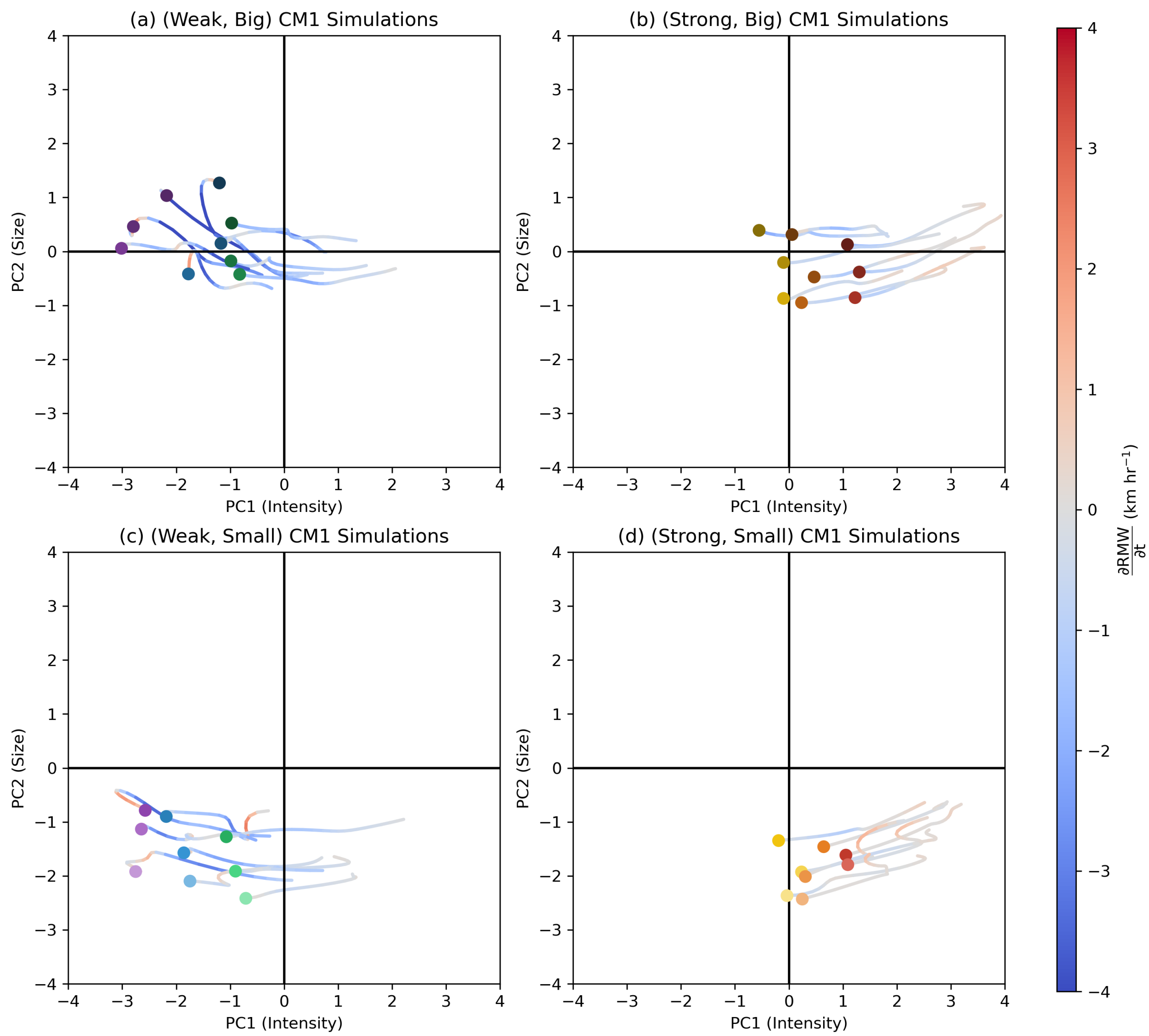

Figure 5.9: As in Fig. 5.8, but instead shaded by instantaneous contraction rate of RMW (km hr^{-1}).

Fig 5.10 shows an alternative way of viewing intensification and contraction rates as a function of PC1-Intensity and PC2-Size from 0–24 hr after RI Onset. Here, we can very clearly see that intensification rates clearly depend more on PC1-Intensity than PC2-Size, and that the relationship is nonlinear (Fig. 5.10a-b). Very weak TCs from $-3 \leq$ PC1-Intensity ≤ -1 start out intensifying at a very slow rate, but accelerate as TCs become average intensity. The initially very strong, small TCs can keep accelerating beyond average intensity, but after a PC1-Intensity of 1 and above, TCs start to reach their steady-state intensities and start to decelerate.

In terms of PC2-Size, instantaneous intensification rate only weakly depend on size, where the largest TCs do not reach as high intensification rates, but small TCs have very variable intensification rates. This suggests that if predicting future intensification rates, then current intensity should be given much more weight than size.

However, RMW contraction rates depend on both PC1-Intensity and PC2-Size (Fig. 5.7c-d). Stratifying by PC1-Intensity shows that the very weak TCs have the largest spread in contraction rates, and can reach the fastest rates as well. In contrast, as TCs intensify to PC1-Intensity > 1, then TCs start to expand.

With respect to PC2-Size, contraction rates are fastest for the biggest TCs, and smallest for the smallest TCs. However, the largest TCs also appear to have the largest spread in contraction rates, as well.

Extending the time out to 0–72 hr after RI Onset and binning by increments of 1, Fig. 5.11 shows that the relationships remain consistent. Here, it is easier to see distributions at each PC bin, and that there is the most variability in intensification rates for a PC1-Intensity of 1–2. In terms of PC2-Size, the relationship between intensification rates and PC2-Size appears to be a bit more robust, such that smaller TCs have a larger fraction of higher intensification rates.

In terms of contraction rates, there are more brief positive contraction rates for above-average TCs, which imply eyewall replacement cycles. Interestingly, the relationship between contraction rates and PC2 is nearly flat with wide tails. However, more of the simulations reached steady-state by 72 hr after RI Onset, which is washing out the signal.

Fig. 5.12 summarizes the 12-hr and 24-hr intensity change from the location of RI Onset in PC1-Intensity/PC2-Size. Results suggest a linear relationship of the increase in V_{max} based on

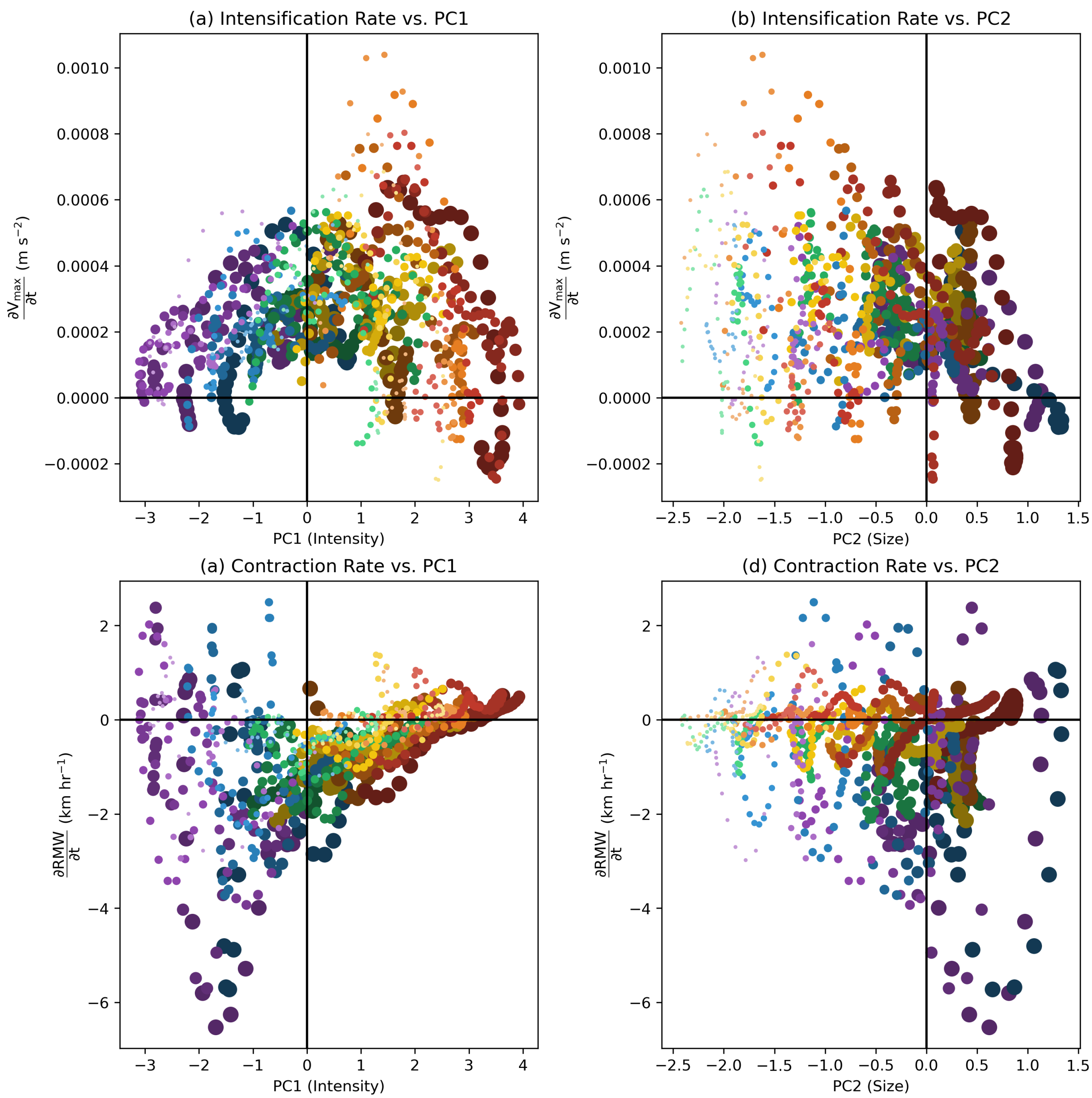

Figure 5.10: Instantaneous intensification rates (m s^{-2}) from 0–24 hr after RI Onset as a function of (a) current PC1-Intensity and (b) current PC2-Size, and instantaneous contraction rates (km hr^{-1} from 0–24 hr after RI Onset as a function of (c) current PC1-Intensity and (d) current PC2-Size. Colors are consistent and sizes are proportional to the color key in Figs. 4.5–4.6

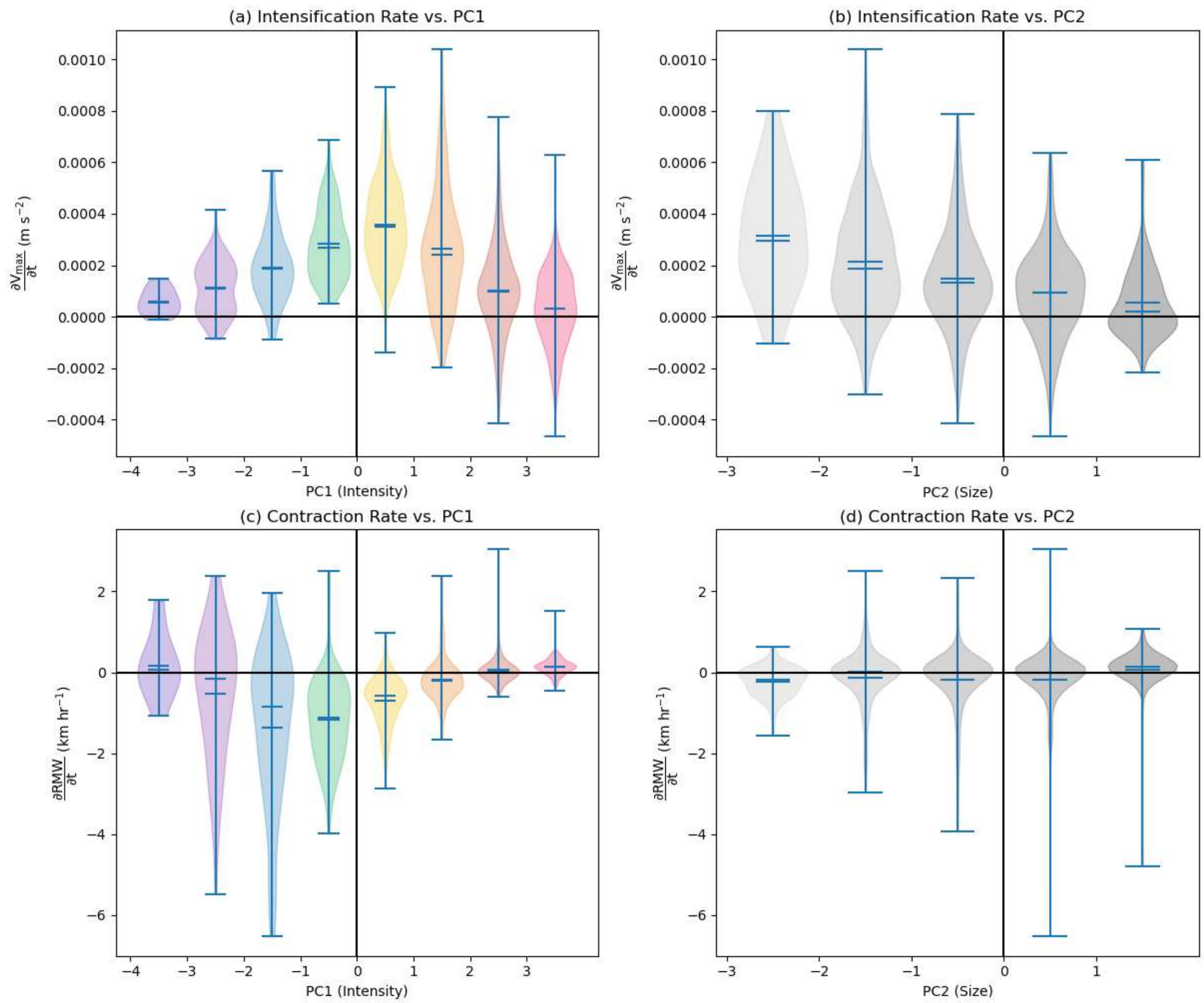

Figure 5.11: As in Fig. 5.10, but extending the time from 0–72 hr after RI Onset, and converted to violin plots that are binned every 1 PC. Blue tickmarks indicate the means, medians, and extrema within each bin.

the the initial PC1-Intensity within the first 12-hr of RI. Strikingly, TCs that begin RI at an above-average intensity are capable of exceeding a 24-hr RI threshold within 12 hours (Fig. 5.12a). However, TCs that begin RI at average or slightly below average intensities are capable of having the largest increase in V_{max} by 24 hr, since they have a longer duration of RI rates (Fig. 5.12b). Finally, TCs that begin RI at a PC1-Intensity below -1 barely reach RI thresholds by 24 hours. However, these TCs are still undergoing RI after 24 hr, and have the largest overall change in V_{max} by the time they are done.

There is much less of a relationship between change in V_{max} and PC2-Size at RI Onset. In fact, the R^2 value decreases from 0.18 to 0.119 as time increases. Additionally, Fig. 5.13 shows how much the RMW contracts both 12- and 24-hr after RI Onset, and results show that RMW contracts at a nonlinear rate. Weak, big TCs beginning RI contract quickly and for a long duration, but weak, small TCs mostly contract after 12-hr. RMW also has a stronger relationship with PC2-Size.

5.4 Discussion and Conclusion

In Chapter 4, we hypothesized that based on the slab and height-resolved TCBL model results, there could be a “goldilocks zone” in which large TCs with near-average intensities may have an optimal balance of u/I setting the updraft sufficiently far inward from the RMW and enhanced vorticity stretching in the TCBL. However, with the addition of resolving height in height-resolved TCBL model, we saw that strong, large TCs had the strongest secondary circulation, which is conducive for future intensification.

To test these findings, we then tested the same initial profiles with a full-physics, axisymmetric model and allowed the TCBL effects to interact with the full vortex and moist convection. Results showed that the strong, big TCs had the largest steady-state intensities, and the weak, big TCs did indeed contract the most. Within the context of RI, we also find that the relationship between intensity at RI Onset and intensity 12 hours later is surprisingly linear, with only a weak dependence on TC size at RI Onset.

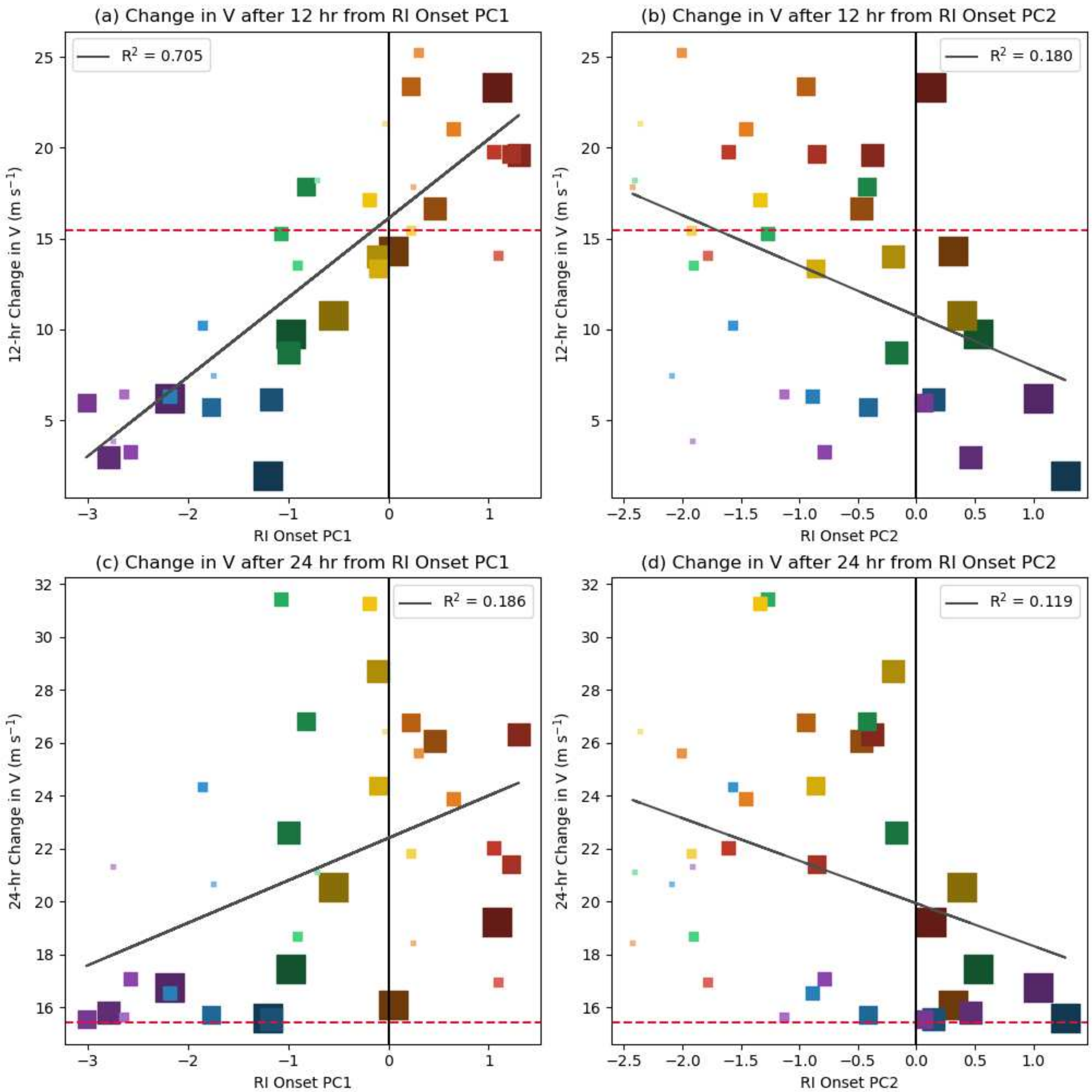

Figure 5.12: Scatter plot of the change in V_{max} at 12 hr after RI Onset as a function of (a) PC1-Intensity and (b) PC2-Size. (c-d) As in (a-b), but for 24 hr after RI Onset. Color key is identical to the one shown in Figs. 4.5–4.6.

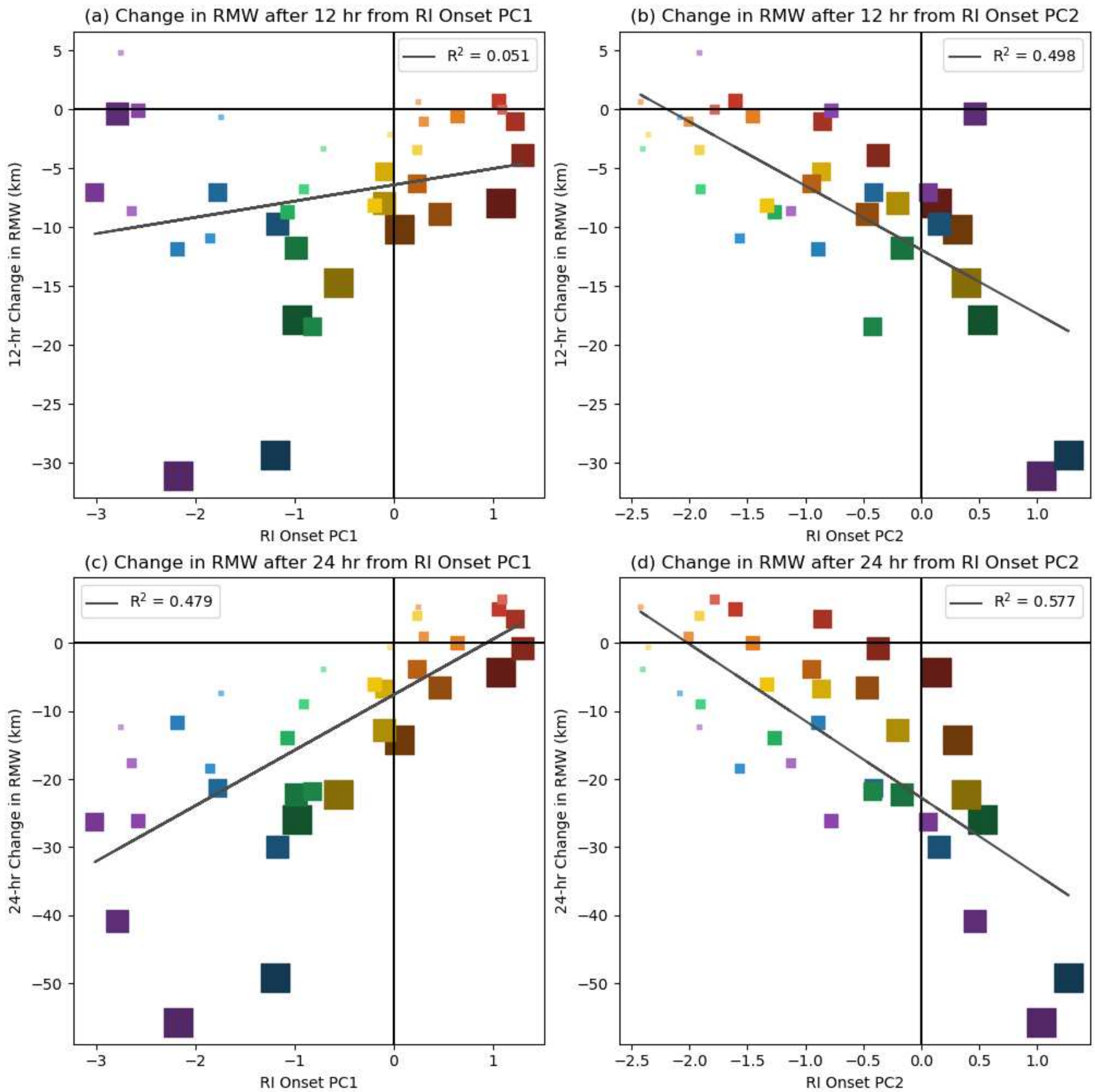

Figure 5.13: As in Fig. 5.12, but for the change in RMW at (a-b) 12 hr after RI Onset and (c-d) 24 hr after RI Onset.

Focusing on instantaneous intensification rates, we find that contrary to expectations from the height-resolved TCBL model results, the initially strong, small TCs intensified the fastest during RI. However, these TCs did not intensify much faster than large TCs with similar intensities, which again suggests that intensification rates are much more strongly dependent on current intensity than size. Interestingly, this also suggests that TC intensification is not entirely logistic, because the TCs that were closest to their "carrying capacities" or steady-state intensities at RI onset had the fastest intensification rates. If intensification was purely logistic, the fastest rates would have occurred at exactly $0.5 \times V_{steady-state}$ regardless of initial intensity.

Looking at contraction rates, we find that RMW contraction has more memory of initial conditions than intensification, and while contraction rates depend on both initial intensity and structure, the initial intensity is more important. In particular, the initially weak, big TCs continued to contract faster than those that were initialized in other quadrants when comparing only the segments of TC evolution within the strong, small quadrant. Contraction rates also evolve nonlinearly, and even though there is a consistent, nearly linear trend by 24 hours after RI Onset, the weakest TCs mostly contracted 12 hours after RI Onset.

Combined, we start to see a picture that significant RMW contraction is associated with slower intensification rates during RI. However, the relationship is nonlinear, and has a very weak correlation on an instantaneous time scale because contraction rates depend on initial conditions more strongly than intensification rates. Therefore, individual TCs have different relative rates at which they transfer from a "contraction-dominant mode" to an "amplification-dominant mode." Overall, this study indicates that there is a smooth transition between two general patterns of RI: (1) a smooth transition from primarily contracting to primarily amplifying in initially large TCs, and (2) minimal size change and primarily amplifying in initially small TCs (Fig. 5.14). These general patterns of RI are generally determined by the initial size of the TC, and as the initial TC size increases, the maximum RMW contraction rates generally increase, as well. However, as TCs begin to approach near-average intensities, RMW contraction rates slow down and intensification rates ramp up. In this study, we find that a PC1-Intensity of roughly -1 could be transition point, but acknowledge that this rough threshold could be specific to the axisymmetric simulations used in this study. As RI continues, Fig. 5.14 also shows that the initially large TCs can reach the highest quasi-steady intensities, but the initially small TCs can reach the fastest intensification rates. However, a key finding of this study is that intensification rates depend more on current intensity than size, so the difference in intensification rates for strong TCs is small across sizes.

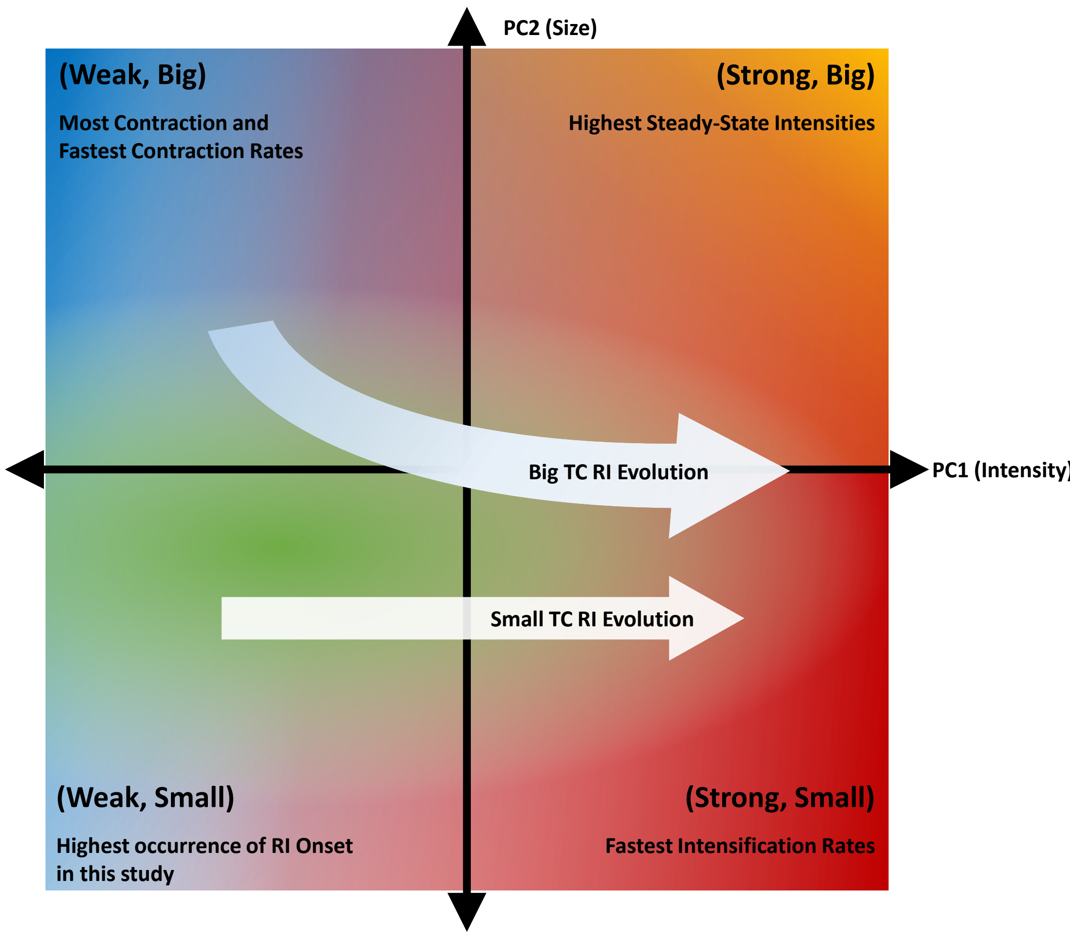

Figure 5.14: Summary schematic of the new PC1-Intensity and PC2-Size space, where blues represent contraction rates, reds represent intensification rates, yellows represent steady-state intensities, and greens represent RI Onset. The two "modes" of RI are represented by white arrows, where initially large TCs smoothly transition from primarily contracting to primarily intensifying, and initially small TCs do not experience an appreciable size change as they undergo RI.

Future work will continue to explore to what extent 3-Dimensional full-physics and observations confirm or modify the axisymmetric results from this study in both constant and variable environments.

Chapter 6

Conclusions

In this doctoral study, I sought to systematically investigate the interconnected relationships between how the observed variability in TC intensity and structure can be most simplified while retaining realism, how the TCBL responds to this observed variability within the context of rapid intensification, and how rapid intensification varies as a function of intensity and size.

In Ch. 2, TC structure and intensity were characterized in a way that reduced the dimensionality into a 2D phase space that retained as much variance as possible. To accomplish this goal, a new parameter ϕ was introduced that describes the tangential wind decay outside of the radius of maximum wind (RMW). By using this new parameter ϕ and six additional, commonly-observed quantities, an Empirical Orthogonal Function (EOF) analysis was computed to identify the primary modes of variability between TC intensity and structure. The dominant mode of variability is associated with TC intensity, and TC size explains the second most variance. Together, these two principal components explain nearly 80% of observed variance, and the third principal component, which is associated with the parameter ϕ and describes TC maturity, explains approximately an additional 10% of observed variance, and by virtue of being orthogonal, provides additional information on characterizing TC structure.

The first two principal components represent a new, simplified intensity-size phase space. In addition to showcasing example useful applications with both observations of Hurricanes Rita (2005) and Charley (2004) and numerical simulations of Hurricane Rita, this new intensity-size phase space lays the foundation for the rest of this doctoral study and yields significant new scientific insight.

In Ch. 3, the new intensity-size phase space was used to investigate characteristics of how TC intensity and size vary within the phase space, how to appropriately represent this variability with simplified tangential wind profiles, and what some of the implications of these new simplified profiles are. By binning the EOF parameters into bins of PC1-2 with size 0.5 × 0.5, "anchor points" were defined and used to construct three different profile methods within each bin: the Holland method, the Willoughby method, and a new method referred to as the Angular Momentum method. These profiles were then found to better represent bin averages in different parts of the intensity-size phase space, but all generally were representative of observed variability when compared to the original aircraft observations. The profiles developed in this chapter continued to lay the foundation for the rest of this doctoral study, and were used to yield additional new scientific insight, as well.

In Ch. 4, the TCBL response to the realistic, simplified tangential wind forcings developed in Ch. 3 was investigated. In particular, how the TCBL dynamical response to a constant gradient wind forcing varies across TC intensity and size was examined, as well as whether the specific profile method used had a larger or smaller impact on the TCBL response than the general intensity and size. Results showed that while there were differences across profile methods that may matter for specific applications, the general patterns across the intensity-size phase space revealed a consistent TCBL response across the methods within the slab model. In particular, the general TCBL response to variations of TC intensity and size are that while strong, big TCs produced large vorticity stretching, they had a smaller u/I term, which indicates that the frictionally forced updraft is closer to the RMW, and therefore likely to further radially outward and less efficient from a balanced vortex model perspective. In contrast, weak TCs regardless of size had the largest u/I term and therefore possibly more efficient heating, but they also produced the least vorticity stretching, which is not as favorable for intensification. Strong, small TCBLs experienced RMW expansion as they adjusted, which is also not as favorable for intensification.

The Angular Momentum profiles were then compared to the height-resolved TCBL model results, and results suggest that while there are differences in the details between the height-averaged and height-resolved simulations, the general patterns remain qualitatively similar, where the weak, big simulations experienced the most RMW contraction, the strong, big TCs experienced the largest supergradient adjustment, and the very small TCs experienced RMW expansion. However, in the height-resolved simulations, TCBL adjustments were much weaker for the Angular Momentum method.

Finally, in Ch. 5, the relationships between TC intensity and size to rapid intensification within full-physics, axisymmetric models was investigated. In particular, the relationship between RMW contraction rates and rapid intensification rates with respect to both initial and current states of TC intensity and size was investigated. Findings suggest that intensification rates depend more on the current intensity of a TC, rather than either initial intensity or size at any time. In contrast, RMW contraction rates depend most on initial conditions of size and initial intensity to a lesser extent. Together, the relationships between intensity, size, and intensification rates indicate a smooth transition between two general patterns of RI: (1) a smooth transition from primarily contracting to primarily amplifying in initially large TCs, and (2) minimal size change and primarily amplifying in initially small TCs (Fig. 5.14).

In conclusion, this doctoral study indicates that there are systematic relationships between the TC *initial* conditions of TC intensity and size, the *current* conditions of TC intensify and size, the dynamic TCBL response to these conditions, and rapid intensification rates. These patterns are revealed in the context of a new intensity-size phase space, and through analysis of simplified profiles in both TCBL models and full-physics, axisymmetric models, I show that the TCBL is able to reproduce many of the features seen in the full-physics simulations, such as that strong, big TCs produce the largest intensities; weak, big TCs exhibit the strongest contraction rates; and small TCs regardless of intensity have the smallest RMW changes. However, the strong, small TCs are able to produce the highest peak intensification rates. I also find that intensification rates depend much more on intensity than size. Finally, while intensification rates and RMW contraction rates are weakly correlated overall, I find that there are relationships between them during RI, but that these relationships depend on initial size. Hurricane Rita (2005) is a prime example of the "large mode of RI" because it was a TC that was initially weak and big, and Rita experienced large contraction in the beginning portion of RI until it contracted to near average-size in the dataset and maintained that size for the duration of RI. In contrast, Hurricane Charley (2004) is a prime example of the "small mode" of RI, in which significant RI occurred without appreciable size changes.

The findings of the doctoral study suggest that RI prediction could potentially be improved if the relationships between TC size and intensity investigated in this study are further explored and exploited. Future work will continue to explore to what extent 3-Dimensional, full-physics simulations and observations confirm or modify the axisymmetric results presented herein, in both quiescent and sheared environments.

References

Bell, M. M., M. T. Montgomery, and K. A. Emanuel, 2012: Air–Sea Enthalpy and Momentum Exchange at Major Hurricane Wind Speeds Observed during CBLAST. *Journal of the Atmospheric Sciences*, doi: 10.1175/JAS-D-11-0276.1.

Boose, E. R., 2004: A method for reconstructing historical hurricanes. *Hurricanes and Typhoons: Past, Present, and Future*, **99**, 120.

Boyd, J. P., 2001: *Chebyshev and Fourier spectral methods*. Courier Corporation.

Bryan, G. H., and J. M. Fritsch, 2002: A benchmark simulation for moist nonhydrostatic numerical models. *Mon. Wea. Rev.*, **130**, 2917–2928, doi: 10.1175/1520-0493(2002)130<2917:ABSFMN>2.0.CO;2.

Cangialosi, J. P., E. Blake, M. DeMaria, A. Penny, A. Latto, E. Rappaport, and V. Tallapragada, 2020: Recent progress in tropical cyclone intensity forecasting at the national hurricane center. *Wea. and Forecast.*, **35 (5)**, 1913–1922, doi: 10.1175/WAF-D-20-0059.1.

Chan, K. T. F., and J. C. L. Chan, 2012: Size and strength of tropical cyclones as inferred from quikscat data. *Mon. Wea. Rev.*, **140 (3)**, 811–824, doi: 10.1175/MWR-D-10-05062.1.

Chavas, D. R., and K. A. Emanuel, 2010: A quikscat climatology of tropical cyclone size. *Geophys. Research Letters*, **37 (18)**, L18 816, doi: https://doi.org/10.1029/2010GL044558.

Davis, C., and Coauthors, 2008: Prediction of landfalling hurricanes with the advanced hurricane wrf model. *Mon. Wea. Rev.*, **136**, 1990–2005, doi: 10.1175/2007MWR2085.1.

DeMaria, M., J. L. Franklin, M. J. Onderlinde, and J. Kaplan, 2021: Operational forecasting of tropical cyclone rapid intensification at the national hurricane center. *Atmosphere*, **12 (6)**, doi: 10.3390/atmos12060683.

Dudhia, J., 1989: Numerical study of convection observed during winter monsoon experiment using a mesoscale two-dimensional model. *J. Atmos. Sci.*, **46**, 3077–3107, doi: 10.1175/1520-0469(1989)046<3077:NSOCOD>2.0.CO;2.

Durran, D. R., and P. N. Blossey, 2012: Implicit–explicit multistep methods for fast-wave–slow-wave problems. *Mon. Wea. Rev.*, **140 (4)**, 1307–1325, doi: 10.1175/MWR-D-11-00088.1.

Ek, M. B., K. E. Mitchell, Y. Lin, E. Rogers, P. Grunmann, V. Koren, G. Gayno, and J. D. Tarpley, 2003: Implementation of noah land surface model advances in the national centers for environmental prediction operational mesoscale eta model. *J. Geophys. Res.*, **108**, 2156–2202, doi: 10.1029/2002JD003296.

Eliassen, E., 1951: Slow thermally or frictionally controlled meridional circulation in a circular vortex. *Astrophys. Nor.*, **5**, 19–60.

Foerster, A. M., and M. M. Bell, 2017: Thermodynamic retrieval in rapidly rotating vortices from multiple-doppler radar data. *Journal of Atmospheric and Oceanic Technology*, **34 (11)**, 2353 – 2374, doi: 10.1175/JTECH-D-17-0073.1.

Fudeyasu, H., K. Ito, and Y. Miyamoto, 2018: Characteristics of tropical cyclone rapid intensification over the western north pacific. *J. Clim.*, **31 (21)**, 8917–8930, doi: 10.1175/JCLI-D-17-0653.1.

Gray, W. M., 1968: Global view of the origin of tropical disturbances and storms. *Mon. Wea. Rev.*, doi: 10.1175/1520-0493(1968)096<0669:GVOTOO>2.0.CO;2.

Guo, X., and Z.-M. Tan, 2017: Tropical cyclone fullness: A new concept for interpreting storm intensity. *Geophysical Research Letters*, **44 (9)**, 4324–4331, doi: 10.1002/2017GL073680.

Hendricks, E. A., W. H. Schubert, Y.-H. Chen, H.-C. Kuo, and M. S. Peng, 2014: Hurricane eyewall evolution in a forced shallow-water model. *J. Atmos. Sci.*, **71 (5)**, 1623–1643, doi: 10.1175/JAS-D-13-0303.1.

Holland, G., 2008: A revised hurricane pressure–wind model. *Mon. Wea. Rev.*, **136 (9)**, 3432–3445, doi: 10.1175/2008MWR2395.1.

Holland, G. H., 1980: An analytic model of the wind and pressure profiles in hurricanes. *Mon. Wea. Rev.*, **108 (8)**, 1212–1218, doi: 10.1175/1520-0493(1980)108<1212:AAMOTW>2.0.CO;2.

Holland, G. J., J. I. Belanger, and A. Fritz, 2010: A revised model for radial profiles of hurricane winds. *Monthly Weather Review*, **138 (12)**, 4393–4401, doi: 10.1175/2010MWR3317.1.

Hong, S.-Y., Y. Noh, and J. Dudhia, 2006: A new vertical diffusion package with an explicit treatment of entrainment processes. *Mon. Wea. Rev.*, **134**, 2318–2341.

Kain, J. S., and J. M. Fritsch, 1990: A one-dimensional entraining detraining plume model and its application in convective parameterization. *J. Atmos. Sci.*, **47**, 2784–2802, doi: 10.1175/1520-0469(1990)047<2784:AODEPM>2.0.CO;2.

Kaplan, J., and M. DeMaria, 2003: Large-scale characteristics of rapidly intensifying tropical cyclones in the north atlantic basin. *Weather and Forecasting*, **18 (6)**, 1093 – 1108, doi: 10.1175/1520-0434(2003)018<1093:LCORIT>2.0.CO;2.

Kepert, J., 2001: The dynamics of boundary layer jets within the tropical cyclone core. part i: Linear theory. *J. Atmos. Sci.*, **58 (17)**, 2469–2484, doi: 10.1175/1520-0469(2001)058<2469:TDOBLJ>2.0.CO;2.

Kepert, J. D., 2010: Slab- and height-resolving models of the tropical cyclone boundary layer. part i: Comparing the simulations. *Quarterly Journal of the Royal Meteorological Society*, **136 (652)**, 1686–1699, doi: https://doi.org/10.1002/qj.667.

Kepert, J. D., 2013: How does the boundary layer contribute to eyewall replacement cycles in axisymmetric tropical cyclones? *J. Atmos. Sci.*, **70**, 2808–2830.

Kepert, J. D., 2017: Time and space scales in the tropical cyclone boundary layer, and the location of the eyewall updraft. *J. Atmos. Sci.*, **74 (10)**, 3305–3323, doi: 10.1175/JAS-D-17-0077.1.

Kepert, J. D., and D. S. Nolan, 2014: Reply to “comments on ‘how does the boundary layer contribute to eyewall replacement cycles in axisymmetric tropical cyclones?’". *J. Atmos. Sci.*, **71**, 4692–4704.

Kilroy, G., R. K. Smith, and M. T. Montgomery, 2016: Why do model tropical cyclones grow progressively in size and decay in intensity after reaching maturity? *J. Atmos. Sci.*, **73 (2)**, 487–503, doi: 10.1175/JAS-D-15-0157.1.

Klotzbach, P. J., M. M. Bell, S. G. Bowen, E. J. Gibney, K. R. Knapp, and C. J. Schreck, 2020: Surface pressure a more skillful predictor of normalized hurricane damage than maximum sustained wind. *Bull. Amer. Meteor. Soc.*, **101 (6)**, E830–E846.

Knaff, J. A., C. J. Slocum, K. D. Musgrave, C. R. Sampson, and B. R. Strahl, 2016: Using routinely available information to estimate tropical cyclone wind structure. *Mon. Wea. Rev.*, **144 (4)**, 1233–1247, doi: 10.1175/MWR-D-15-0267.1.

Knapp, K. R., M. C. Kruk, D. H. Levinson, H. J. Diamond, and C. J. Neumann, 2010: The international best track archive for climate stewardship (ibtracs): Unifying tropical cyclone best track data. 363–376 pp., doi: 10.1175/2009BAMS2755.1.

Mallen, K. J., M. T. Montgomery, and B. Wang, 2005: Reexamining the near-core radial structure of the tropical cyclone primary circulation: Implications for vortex resiliency. *J. Atmos. Sci.*, **62 (2)**, 408–425, doi: 10.1175/JAS-3377.1.

Martinez, J., M. M. Bell, R. F. Rogers, and J. D. Doyle, 2019: Axisymmetric potential vorticity evolution of hurricane patricia (2015). *J. Atmos. Sci.*, **76 (7)**, 2043–2063, doi: 10.1175/JAS-D-18-0373.1.

Martinez, J., M. M. Bell, J. L. Vigh, and R. F. Rogers, 2017: Examining tropical cyclone structure and intensification with the flight+ dataset from 1999 to 2012. *Mon. Wea. Rev.*, **145 (11)**, 4401 – 4421, doi: 10.1175/MWR-D-17-0011.1.

Martinez, J., C. C. Nam, and M. M. Bell, 2020: On the contributions of incipient vortex circulation and environmental moisture to tropical cyclone expansion. *J. Geophys. Research: Atmospheres*, **125 (21)**, e2020JD033 324, doi: 10.1029/2020JD033324.

Merrill, R. T., 1984: A comparison of large and small tropical cyclones. *Mon. Wea. Rev.*, **112 (7)**, 1408–1418, doi: 10.1175/1520-0493(1984)112<1408:ACOLAS>2.0.CO;2.

Miyamoto, Y., and T. Takemi, 2015: A triggering mechanism for rapid intensification of tropical cyclones. *J. Atmos. Sci.*, **72 (7)**, 2666–2681, doi: 10.1175/JAS-D-14-0193.1.

Mlawer, E. J., S. J. Taubman, P. D. Brown, M. J. Iacono, and S. A. Clough, 1997: Radiative transfer for inhomogeneous atmospheres: Rrtm, a validated correlated-k model for the longwave. *J. Geophys. Res.*, **102**, 16 663–16 682, doi: doi:10.1029/97JD00237.

Montgomery, M. T., S. F. Abarca, R. K. Smith, C.-C. Wu, and Y.-H. Huang, 2014: Comments on "how does the boundary layer contribute to eyewall replacement cycles in axisymmetric tropical cyclones. *J. Atmos. Sci.*, **71**, 4682–4691.

Montgomery, M. T., J. Persing, and R. K. Smith, 2015: Putting to rest wishe-ful misconceptions for tropical cyclone intensification. *Journal of Advances in Modeling Earth Systems*, **7**, 92–109, doi: https://doi.org/10.1002/2014MS000362.

Montgomery, M. T., and R. K. Smith, 2014: Paradigms for tropical cyclone intensification. *Aust. Meteor. Oceanogr. J.*, **64**, 37–66.

Montgomery, M. T., R. K. Smith, and S. V. Nguyen, 2010: Sensitivity of tropical-cyclone models to the surface drag coefficient. *Quarterly Journal of the Royal Meteorological Society*, **136**, 1945–1953, doi: 10.1002/qj.702.

Musgrave, K. D., R. K. Taft, J. L. Vigh, B. D. McNoldy, and W. H. Schubert, 2012: Time evolution of the intensity and size of tropical cyclones. *J. Adv. Model. Earth Sys.*, **4 (3)**, M08 001, doi: https://doi.org/10.1029/2011MS000104.

Ooyama, K. V., 2002: The cubic-spline transform method: Basic definitions and tests in a 1d single domain. *Mon. Wea. Rev.*, **130 (10)**, 2392–2415, doi: 10.1175/1520-0493(2002)130<2392:TCSTMB>2.0.CO;2.

Orszag, S. A., 1970: Transform method for the calculation of vector-coupled sums: Application to the spectral form of the vorticity equation. *J. Atmos. Sci.*, **27 (6)**, 890–895, doi: 10.1175/1520-0469(1970)027<0890:TMFTCO>2.0.CO;2.

Pendergrass, A. G., and H. E. Willoughby, 2009: Diabatically induced secondary flows in tropical cyclones. part i: Quasi-steady forcing. *Monthly Weather Review*, **137 (3)**, 805–821, doi: 10.1175/2008MWR2657.1.

Peng, M., L. Xie, and L. J. Pietrafesa, 2006: Tropical cyclone induced asymmetry of sea level surge and fall and its presentation in a storm surge model with parametric wind fields. *Ocean Model.*, **14 (1-2)**, 81–101, doi: https://doi.org/10.1016/j.ocemod.2006.03.004.

Powell, M. D., G. Soukup, S. Cocke, S. Gulati, N. Morisseau-Leroy, S. Hamid, N. Dorst, and L. Axe, 2005: State of florida hurricane loss prediction model: Atmospheric science component. *J. Wind Eng. Ind. Aerodyn.*, **93 (8)**, 651–674, doi: https://doi.org/10.1016/j.jweia.2005.05.008.

Reasor, P. D., M. T. Montgomery, and L. D. Grasso, 2004: A new look at the problem of tropical cyclones in vertical shear flow: Vortex resiliency. *J. Atmos. Sci.*, **61 (1)**, 3–22, doi: 10.1175/1520-0469(2004)061<0003:ANLATP>2.0.CO;2.

Rogers, R., P. Reasor, and S. Lorsolo, 2013: Airborne doppler observations of the inner-core structural differences between intensifying and steady-state tropical cyclones. *Mon. Wea. Rev.*, **141 (9)**, 2970–2991, doi: 10.1175/MWR-D-12-00357.1.

Rogers, R. F., and Coauthors, 2017: Rewriting the tropical record books: The extraordinary intensification of hurricane patricia (2015). *Bull. Amer. Meteo. Soc.*, **98 (10)**, 2091–2112, doi: 10.1175/BAMS-D-16-0039.1.

Rozoff, C. M., D. S. Nolan, J. P. Kossin, F. Zhang, and J. Fang, 2012: The roles of an expanding wind field and inertial stability in tropical cyclone secondary eyewall formation. *J. Atmos. Sci.*, **69 (9)**, 2621 – 2643, doi: 10.1175/JAS-D-11-0326.1.

Schubert, W. H., and J. J. Hack, 1982: Inertial stability and tropical cyclone development. *J. Atmos. Sci.*, **39 (8)**, 1687–1697, doi: 10.1175/1520-0469(1982)039<1687:ISATCD>2.0.CO;2.

Schubert, W. H., and J. J. Hack, 1983: Transformed eliassen balanced vortex model. *Journal of Atmospheric Sciences*, **40 (6)**, 1571–1583, doi: 10.1175/1520-0469(1983)040<1571:TEBVM>2.0.CO;2.

Shapiro, L. J., and M. T. Montgomery, 1993: A three-dimensional balance theory for rapidly rotating vortices. *J. Atmos. Sci.*, **50 (19)**, 3322–3335, doi: 10.1175/1520-0469(1993)050<3322:ATDBTF>2.0.CO;2.

Shapiro, L. J., and H. E. Willoughby, 1982: The response of balanced hurricanes to local sources of heat and momentum. *J. Atmos. Sci.*, **39 (2)**, 378–394, doi: 10.1175/1520-0469(1982)039<0378:TROBHT>2.0.CO;2.

Smith, R. K., and M. T. Montgomery, 2015: Toward clarity on understanding tropical cyclone intensification. *J. Atmos. Sci.*, **72 (8)**, 3020–3031, doi: 10.1175/JAS-D-15-0017.1.

Smith, R. K., M. T. Montgomery, and G. L. Thomsen, 2014: Sensitivity of tropical-cyclone models to the surface drag coefficient in different boundary-layer schemes. *Quarterly Journal of the Royal Meteorological Society*, **140**, 792–804, doi: 10.1002/qj.2057.

Stern, D. P., J. L. Vigh, D. S. Nolan, and F. Zhang, 2015: Revisiting the relationship between eyewall contraction and intensification. *J.Atmos. Sci.*, **72 (4)**, 1283–1306, doi: 10.1175/JAS-D-14-0261.1.

Tao, D., M. Bell, R. Rotunno, and P. J. van Leeuwen, 2020: Why do the maximum intensities in modeled tropical cyclones vary under the same environmental conditions? *Geo-*

phys. Research Letters, **47 (3)**, e2019GL085 980, doi: 10.1029/2019GL085980, e2019GL085980 2019GL085980.

Tao, D., P. J. van Leeuwen, M. Bell, and Y. Ying, 2022: Dynamics and predictability of tropical cyclone rapid intensification in ensemble simulations of hurricane patricia (2015). *J. Geophys. Res.: Atmos.*, **127 (8)**, e2021JD036 079, doi: https://doi.org/10.1029/2021JD036079, e2021JD036079 2021JD036079.

Thompson, G., and T. Eidhammer, 2014: A study of aerosol impacts on clouds and precipitation development in a large winter cyclone. *J. Atmos. Sci.*, **71**, 3636–3658, doi: 10.1175/JAS-D-13-0305.1.

Torgerson, W. S., J. Schwendike, A. Ross, and C. Short, 2022: Intensity fluctuations in hurricane irma (2017) during a period of rapid intensification. *Weather and Climate Dynamics Discussions*, **2022**, 1–44, doi: 10.5194/wcd-2021-81.

Trabing, B. C., and M. M. Bell, 2020: Understanding error distributions of hurricane intensity forecasts during rapid intensity changes. *Weather and Forecasting*, **35 (6)**, 2219–2234, doi: 10.1175/WAF-D-19-0253.1.

Velden, C., and Coauthors, 2006: The dvorak tropical cyclone intensity estimation technique: A satellite-based method that has endured for over 30 years. *Bull. Amer. Met. Soc.*, **87 (9)**, 1195 – 1210, doi: 10.1175/BAMS-87-9-1195.

Vigh, J. L., and Coauthors, 2020: Flight+: The extended flight level dataset for tropical cyclones (version 1.3). Accessed dd mm yyyy, doi: 10.5065/D6WS8R93.

Wheeler, M. C., and H. H. Hendon, 2004: An all-season real-time multivariate mjo index: Development of an index for monitoring and prediction. *Mon. Wea. Rev.*, **132 (8)**, 1917–1932, doi: 10.1175/1520-0493(2004)132<1917:AARMMI>2.0.CO;2.

Williams, G. J., R. K. Taft, B. D. McNoldy, and W. H. Schubert, 2013: Shock-like structures in the tropical cyclone boundary layer. *J. Advances in Modeling Earth Systems*, **5 (2)**, 338–353, doi: https://doi.org/10.1002/jame.20028.

Williams Jr., G. J., 2015: The effects of vortex structure and vortex translation on the tropical cyclone boundary layer wind field. *Journal of Advances in Modeling Earth Systems*, **7 (1)**, 188–214, doi: https://doi.org/10.1002/2013MS000299.

Willoughby, H. E., R. W. R. Darling, and M. E. Rahn, 2006: Parametric representation of the primary hurricane vortex. part ii: A new family of sectionally continuous profiles. *Mon. Wea. Rev.*, **134 (4)**, 1102–1120, doi: 10.1175/MWR3106.1.

Willoughby, H. E., and M. E. Rahn, 2004: Parametric representation of the primary hurricane vortex. part i: Observations and evaluation of the holland (1980) model. *Mon. Wea. Rev.*, **132 (12)**, 3033–3048, doi: 10.1175/MWR2831.1.

Xu, J., and Y. Wang, 2015: A statistical analysis on the dependence of tropical cyclone intensification rate on the storm intensity and size in the north atlantic. *Weather and Forecasting*, **30 (3)**, 692 – 701, doi: 10.1175/WAF-D-14-00141.1.

Xu, J., and Y. Wang, 2018: Effect of the initial vortex structure on intensification of a numerically simulated tropical cyclone. *Journal of the Meteorological Society of Japan. Ser. II*, **96 (2)**, 111–126, doi: 10.2151/jmsj.2018-014.